Methods for Control of Granular Material Attributes

Thesis by
Robert Andrew Buarque de Macedo

In Partial Fulfillment of the Requirements for the
Degree of
Doctorate of Philosophy in Applied Mechanics

CALIFORNIA INSTITUTE OF TECHNOLOGY
Pasadena, California

2023
Defended August 11, 2022

Robert Andrew Buarque de Macedo
ORCID: 0000-0002-2218-4117

ACKNOWLEDGEMENTS

First, I must express tremendous gratitude towards my advisor, Jose Andrade. Jose has supported my scientific career through thick and thin. His profound scientific curiosity has resonated with my own, and under his tutelage I have learned the essence of the scientific process. It is rare to find an advisor as brilliant and empathetic as Jose, and I will also be grateful that he took a chance on me.

I am also grateful to those on my committee: Xiaojing Ruby Fu, Joseph Parker, and Kaushik Bhattacharya. Each has provided me with valuable insight throughout my PhD, both in the classroom and in vibrant discussion.

Next, I am deeply thankful for the wonderful members of the COSYMO lab — both current and alumni: Liuchi Li, Konstantinos Karapiperis, John Harmon, Rigoberto Moncada, Ziran Zhou, Raj Kumar Pal, Siavash Khosh Sokhan Monfared, Estefan Fernando Garcia, Jacinto Ulloa, and Anna Gorgogianni. All of you have provided friendship and wisdom throughout my PhD, and this thesis would not have been possible without you.

I'd also like to thank the MCE staff, in particular Jennifer Campbell and Stacie Takase. They have been of tremendous support during my doctorate, helping me navigate the world of scientific administration.

Further, I would also like to acknowledge my wonderful undergraduate academic and research advisors, Kunal Ghosh and Kaushik Dayal. Drs. Ghosh and Dayal pushed me to achieve greatness in science, communication, and philosophical thinking from an early point in my career. Without their advising, I do not think I would be graduating from Caltech today.

I'd also like to thank my cousins and brother-in-law: Evan, Miles, Helena, and Andy. They have provided me with love and support throughout this challenging phase of my life.

I am also deeply appreciative of my friends from all stages of life: from those in high school who support me to this day, to my wonderful classmates at Carnegie Mellon, and to my newest friends at Caltech alongside whom I endured the perils of classes and of the qualifying exams.

To my parents and sister, I owe everything. It is to them I dedicate this thesis.

ABSTRACT

A granular material is a collection of discrete, solid particles. This substance is ubiquitous in nature and industry, with examples ranging from soils, jointed rocks, foodstuffs, ball bearings, powders, and even asteroids. As such, understanding granular materials is necessary for making sense of the physical world. Tremendous progress has been made in directly simulating granular materials in the previous decades, in particular via the discrete element method (DEM). Nevertheless, there remains ample opportunity for manipulating granular materials to achieve specific outcomes by leveraging the DEM. The research presented in this thesis utilizes DEM simulations to develop tools and strategies for manipulating granular material to achieve desired attributes. These attributes include the shape of individual grains, the structure of granular tunnels, and mesoscopic packing characteristics such as packing fraction and coordination number. Optimization of granular materials is considered at 3 different scales: at the single grain scale (10^0 grains), at the scale of granular structures such as arches (10^1 grains), and at the mesoscopic scale (10^3 grains). The first component of this thesis considers automated design of individual grain shapes that embody user-specified morphological properties via genetic algorithms. Next, excavation in granular materials is considered. It is studied how ants can so successfully manipulate granular materials to achieve stable systems by mapping the forces around real ant tunnels. Ant tunnels are simulated using a DEM which can handle arbitrary shaped grains: the Level-Set Discrete Element Method (LS-DEM). Finally, tools are developed for controlling mesoscopic attributes of granular materials as a function of grain shape. To do so, genetic algorithms and a deep generative model are combined with LS-DEM. The methodologies introduced in this thesis serve as a foundation for controlling granular material attributes. Such techniques can be leveraged to engineer granular materials, with applications ranging from swarm robotics, robotic grippers, mechanically tunable fabrics for armor, and robotic excavation.

PUBLISHED CONTENT AND CONTRIBUTIONS

Buarque de Macedo, Robert, Bing Wen Brunton, et al. (2022). "Learning to excavate like ants." In: *In preparation*.
R.B. helped with the conceptualization of the project, wrote the relevant code, analyzed the data, and wrote the manuscript.

Buarque de Macedo, Robert, Konstantinos Karapiperis, et al. (2022). "What is shape? Characterizing particle morphology with genetic algorithms and deep generative models." In: *Granular Matter, in review*.
R.B. helped with the conceptualization of the project, writing the relevant code, analyzing the data, and writing the manuscript.

Karapiperis, Konstantinos et al. (2022). "Stress transmission in entangled granular structures." In: *Granular Matter* 24.3, pp. 1–15.
R.B. helped with the conceptualization of the project, writing relevant code, supervising summer students, and preparing the manuscript.

Buarque de Macedo, Robert, Edward Andò, et al. (2021). "Unearthing real-time 3D ant tunneling mechanics." In: *Proceedings of the National Academy of Sciences* 118, pp. 1–15.
R.B. wrote the relevant code, analyzed the data and wrote the manuscript.

Pal, Raj Kumar, Robert Buraque de Macedo, and José Andrade (2021). "Tunnel excavation in granular media: the role of force chains." In: *Granular Matter* 23.4, pp. 1–14.
R.B. helped with the conceptualizing of the project, writing the relevant code, analyzing the data, and contributed to writing the manuscript.

Buarque de Macedo, Robert, Jason Marshall, and Jose Andrade (2018). "Granular object morphological generation with genetic algorithms for discrete element simulations." In: *Granular Matter* 20.4, pp. 1–12.
R.B. helped with the conceptualization of the project, wrote the relevant code, analyzed the data, and wrote the manuscript.

TABLE OF CONTENTS

LIST OF ILLUSTRATIONS

LIST OF TABLES

Chapter 1

INTRODUCTION

1.1 Objective

Granular materials are any object composed of discrete, solid particles (Buarque de Macedo, Marshall, and Andrade, 2018). These objects are ubiquitous in both nature and industry, with examples ranging from sands, soils, foodstuffs, ball bearings to even asteroid belts (Geng et al., 2001; Ji-Cheng et al., 2011; Coetzee and Els, 2009; Guessasma and Machado, 2018; Hestroffer et al., 2019). In the last few decades, tremendous effort has been exerted in understanding and modeling granular materials. In particular, simulations such as the discrete element method (DEM) for simulating granular materials have gained popularity (Cundall and Strack, 1979a). Recently, attempts have been made to leverage our understanding of granular materials to control and design granular systems. Examples include aleatory architectures, robotic grippers, fabrics with tunable stiffness, and automated excavations (Keller and Jaeger, 2016; Brown et al., 2010; Wang, Li, et al., 2021; Cloud et al., 2021).

This dissertation concerns the control and optimization of granular material attributes using a variety of computational techniques. By attributes, we mean the structure and behavior of granular materials such as the shape of grains, the architecture of granular tunnels and the porosity of a granular material. The tools developed in this thesis serve as a foundation for granular control, as such principles may be built upon by researchers attempting to manipulate granular materials.

In particular, the objectives of this work are:

- Development of methods to control the shape of individual particles to fit specified morphological properties.
- Elucidation of biological strategies to control the structure of granular tunnels.
- Development of methods to control mesoscopic attributes of granular materials, such as packing fraction ϕ, by controlling the shape of particles.

Taken as a whole, this thesis constitutes the development of methods and principles to control granular material attributes at multiple scales: at the scale of individual

particles (10^0 particles), we develop an algorithm to control the shape of grains, at the scale of granular arches (10^1 particles), we explore biologic strategies for controlling tunnel architecture, and at the mesoscopic scale (10^3 grains), we develop foundational tools for controlling the packing characteristics of granular materials see Figure 1.1.

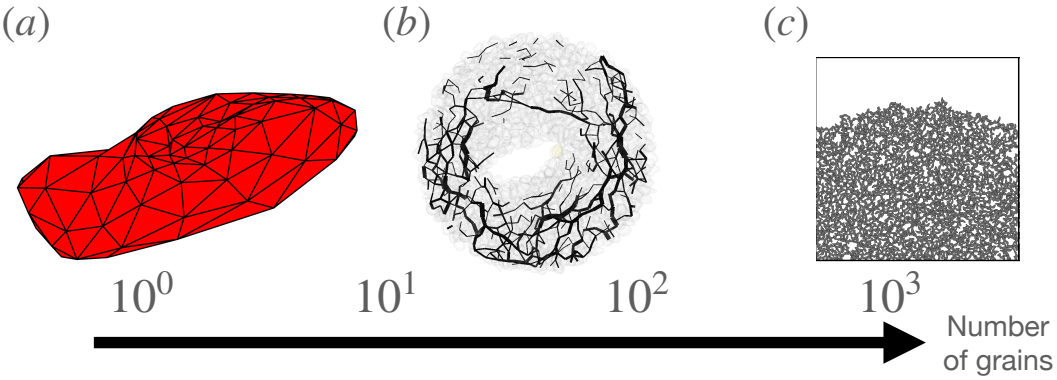

Figure 1.1: Examples of different scales for granular control. (a) Individual particle scale (Buarque de Macedo, Marshall, and Andrade, 2018). (b) Ant tunnel arch scale (Buarque de Macedo, Andò, et al., 2021). (c) Mesoscopic scale (Buarque de Macedo, Karapiperis, et al., 2022).

These techniques are helpful to researchers entering the next stage of granular understanding by attempting to engineer such materials.

1.2 Approach

This thesis spans the micro- to mesoscale of granular materials, beginning with the former and increasing length scale with each chapter. At each scale, a particular variable or variables (controlled variables) are modified to achieve a desired granular material attribute (optimized variables). The list of controlled variables and corresponding optimized variables is given in Table 1.1.

Length Scale	Controlled Variable	Optimized Variable
Single particle (10^0 grains)	Grain shape	Morphological property
Arch scale (10^1 grains)	Grains removed	Arch stability/size
Mesoscale (10^3 grains)	Morphological property	Packing fraction/aspect ratio

Table 1.1: Table depicting controlled variables and optimized variables for each scale.

The first component of this thesis considers optimizing grain shape to fit user-specified morphological properties. Morphological properties are numerical de-

scriptors of a particle's shape. For instance, the roundness of a particle is a number that describes the smoothness of a grain. This is an inherently challenging problem because morphological properties are not necessarily independent, i.e. modifying the roundness of a particle may effect it's elongation, or aspect ratio. Thus, a genetic algorithm is developed which can modify the shape of a particle until the shape matches user-specified morphological properties to a given accuracy.

The second component of the thesis considers excavation in granular materials. Excavation can be thought of as a granular optimization problem, where the optimization variables are which grains to remove with the goal of controlling the size and stability of the tunnel. It is investigated how nature has attempted to solve this optimization problem by studying ant tunnels. Using x-ray computer tomography (XRCT), every soil particle in a soil sample is imaged. During this imaging process, ants tunnel through the soil sample. Then, a DEM simulation which simulates arbitrary shaped grains (Level set discrete element method, or LS-DEM) calculates the forces in an in silico re-creation of every grain in the soil sample. It is discovered that ants take advantage of granular arching to successfully tunnel in latently unstable granular environments.

In the final piece of the thesis, a framework is developed for controlling mesoscopic attributes of granular materials such as packing fraction ϕ (solid area/total area) and coordination number Z (average number of particle contacts per grain). The framework developed in this chapter lays the foundation for topology optimization of granular material attributes. It is first investigated how morphological properties such as roundness, aspect ratio and convexity affect these mesoscopic variables. With this mapping, granular materials can be engineered for specific mesoscopic properties by choosing the appropriate morphological property values. Then, a new set of grain morphological properties are discovered through the use of a deep neural network architecture: variational autoencoders (VAEs). It is demonstrated how these new morphological properties offer advantages over traditional descriptors. Further, it is demonstrated how these descriptors can be mapped to mesoscopic variables. Finally, a methodology for topology optimization of granular materials is proposed which leverages specific properties of the new, machine-discovered morphological properties. Such a topology optimization framework can be used to control mesoscopic attributes of granular materials by modifying grain shape.

1.3 Organization

The thesis is organized as follows:

- Chapter 2 reviews the background information relevant to this thesis. It begins with a general overview of granular materials and discrete element methods (DEM), including the level set discrete element method (LS-DEM). Then the effects of granular shape on material properties are reviewed. Finally, an overview of excavation in granular materials with reinforced and unreinforced tunnels is presented.

- Chapter 3 introduces the granular cloning methodology. This technique uses genetic algorithms to create grains with user-specified morphological properties in 2 or 3 dimensions. The chapter overviews the technical details, application and success rate of the technique.

- Chapter 4 introduces a study which uses XRCT and LS-DEM to learn how ants can successfully manipulate granular materials to achieve stable tunnels. The experimental methodology for imaging all granular materials in a soil during ant tunnel construction is reviewed. Then, the results of an LS-DEM re-creation of the experiment, with grain scale accuracy, is introduced. The findings and implications for automated excavation are reviewed.

- Chapter 5 returns to granular cloning. Grains are created with specific morphological traits using the methodology developed in Chapter 2. Then, mappings between morphological traits and mesoscale granular characteristics, such as packing fraction ϕ and coordination number Z are explored via LS-DEM simulations. These 'forward' mappings are developed such that they can be easily inverted into 'inverse' mappings. Such 'inverse' mappings are invaluable for topology optimization. Then, a deep learning algorithm is leveraged to create a new set of morphological traits that can uniquely describe a particle's shape. The application of this new technique towards topology optimization is explored.

- Chapter 6 concludes the thesis and provides future outlooks.

Chapter 2

BACKGROUND

2.1 Granular materials

A granular material is a collection of discrete, solid objects (Duran, 2012). Granular materials have been studied since antiquity, though primarily through the lens of soil mechanics in recent centuries. Early attempts at understanding granular materials include the works of Charles-Augustin de Coulomb in the 18^{th} century, who conducted both pioneering studies into soil mechanics and developed Coulomb friction (Oliveira, 2004) which later evolved into the 'Coulomb friction law' that is essential to the study of granular materials (Metcalfe et al., 2002). Nevertheless, it is in fact Leonard Euler who originally stated that 'the resistance force exerted on a body by a plane surface along which the body is sliding is proportional to the force pressing the body to the surface' (Zhuravlev, 2013).

Soil mechanics advanced significantly in the early 20^{th} century due to the works of Karl Terzaghi. Terzaghi, known as the 'father of soil mechanics' (Goodman, 1999), was an engineer from Prague. In 1925, Terzaghi published a theory of soil consolidation, as well as the theory of effective stress (Terzaghi, 1925). This equation states that the stress in a saturated granular material could be additively decomposed into the stress in the granular skeleton and the pressure in the pores. This equation is foundational to the fields of soil mechanics and civil engineering. Terzaghi's groundbreaking work also encompassed the stability of slopes and investigations of arching in soil (Terzaghi, 1962; Terzaghi, 1943a). Further, Terzaghi defined the 'angle of repose' of granular materials as the internal angle of friction in the material (Terzaghi, 1943a). More visually, this angle can be defined as the slope a granular material can rest at without becoming unstable (Day, 2010). For instance, the slope of a sand pile is approximately the tangent of the material's angle of repose.

As the 20^{th} century progressed, research into granular materials began to focus more on the micromechanics, i.e. the behavior of the individual grains in a granular material rather than Terzaghi's continuum approaches. Such studies investigated granular materials made of photoelastic discs: discs which refracted light as a function of stress on said grain (Ramesh, 2000). These pioneering studies discovered 'force chains'; the phenomenon of stresses propagating through granular materials

unevenly, with some particles bearing significantly more of the material stress than that which other particles endure (Bardenhagen, Brackbill, and Sulsky, 2000). Further, the advent of computing provided significant insights into the mechanics of granular materials at the grain scale.

2.2 Computational granular mechanics

In 1979, Peter Cundall and Otto Stract proposed the Discrete Element Method, or DEM (Cundall and Strack, 1979a). The DEM is a computational method for simulating individual grains in a granular material. In the original 2D DEM, grains are modeled as circles. These grains interact through normal contact forces, with force magnitude a function of particle overlap. This overlap is a proxy for small particle deformations during contact. Further, grains can interact through a Coulomb friction law and viscous damping forces. Within a decade, the DEM was extended to three dimensional spheres (Cundall, 1988). DEM has been used to model a wide variety of granular materials, including foodstuffs, ball bearings and even asteroids (Coetzee and Els, 2009; Guessasma and Machado, 2018; Hestroffer et al., 2019). These micromechanical studies predicted the continuum scale behavior quantified by Terzaghi while also predicting real physical effects that do not manifest in traditional continuum models, such as granular arching in cohesionless soils (Guo and Zhou, 2013).

One disadvantage of traditional DEM is that particles are spheres. However, real granular materials are not necessarily composed of spherical particles. Further, it has been shown experimentally that the shape of grains can have a significant impact on behavior (Cho, Dodds, and Santamarina, 2006a). Methods to capture non-circular shapes in DEM include sphere clustering and polyhedron approaches (Li, Xu, and Meng, 2015; Nassauer, Liedke, and Kuna, 2013). Nevertheless, such methods are not computationally efficient when representing arbitrary shapes as they require contact checking between every pair of spheres or polyhedra on contacting grains. With this in mind, the level set discrete element method (LS-DEM) was developed to model particles of arbitrary shapes in a computationally efficient manner (Kawamoto et al., 2016). In LS-DEM, each particle in the simulation is represented in two ways: as a collection of points on the surface of the grain, and as a level set Φ. Φ is a space-filling function, where at every point the absolute value of Φ is the distance to the particle surface. Φ is by convention negative inside the particle surface and positive outside. When one particle (A) intersects another (B), the penetration extent can be quickly calculated by looking up the value of each point on A's surface in

B's level set. If the level set value of a point is negative, an equal and opposite force is applied on the particles at the corresponding point with direction normal to the particles' surface.

LS-DEM has been used to exactly simulate the shape, orientation and position of every particle in a soil sample (Kawamoto et al., 2018). This information was gleaned from the soil sample through x-ray computed tomography, or XRCT (Kalender, 2006). With XRCT, x-rays are taken of the soil sample contained in a cylinder from multiple angles. The x-rays can then be used to reconstruct a 3 dimensional image of the sample. From this image, a watershed algorithm can be used to extract the morphology, location and orientation of every grain (Stamati et al., 2020). The grains are converted into points and level sets which are used in simulations. These simulations have a high degree of almost grain scale accuracy in mechanical properties, such as deviatoric strain, when compared to experiments (Kawamoto et al., 2018).

2.3 Particle shape

Grain shape plays a significant role in the emergent properties of granular materials. This has been well studied experimentally. An increase in particle angularity (sharpness of corners) can lead to an increase in material porosity, a decrease in stiffness and an increase in the critical state friction angle (Cho, Dodds, and Santamarina, 2006b). With the introduction of DEM for non-circular particles within the last 2 decades, a wide range of granular materials with non-spherical particles has been investigated.

One of the earlier attempts to move beyond spheres and circles in granular materials was ellipsoidal and elliptical grains. These grains can be seen as a generalization of circular/spherical particles. In 2D, ellipses can be characterized by their 'aspect ratio' i.e. the ratio of the major axis to the minor axis of the ellipse. As a frictionless ellipse is elongated from a circle, and aspect ratio moves away from 1, the packing fraction ϕ for grains prepared by random deposition of frictionless ellipses oscillates about 0.88 before monotonically decreasing as aspect ratio increases above 2 (Guises et al., 2009). On the other hand, coordination number Z (average number of contacting grain neighbors per particle) increases with increasing aspect ratio, beginning at about $Z = 4.2$ before approaching an asymptote at $Z = 5.5$. Frictional ellipses follow similar trends, yet with lower values for both Z and ϕ. Nevertheless, one key difference is a clear maximum ϕ for frictional ellipses occurs at aspect

ratio 1.6. Visually, ellipses begin to experience 'nematic ordering' as they are elongated, which is amplified when when there is no friction (Guises et al., 2009). With nematic ordering grains stack side-by-side, like nematic liquid crystals. This particular ordering begets a higher porosity than the hexagonal packing of circles. Additionally, ellipses require more contacts to reach static equilibrium than circles and so Z increases with aspect ratio (Guises et al., 2009).

In 3D, spheres are conjectured to be the loosest packing convex object when packed optimally (Graaf, Roij, and Dijkstra, 2011). However, for random deposition in a container certain ellipsoids can pack more loosely than spheres (Zhou, Zou, et al., 2011). For frictional ellipsoids, Zhou defines aspect ratio as to the ratio of the largest over the smallest principle axis, and sets the two smaller principle axes as equal. As aspect ratio is increased, trends are similar to that observed in ellipses. ϕ increases until an aspect ratio of 2, followed by a decrease in ϕ. Likewise, Z increases with aspect ratio, approaching an asymptote at about an aspect ratio of 3. Z and ϕ are both larger than in 2D ellipse systems, representing the larger degrees of freedom available in 3 dimensions compared to 2.

The closest non-circular shape to an ellipse may be the capsule. Capsules have pill-like shapes, and consist of two circles connected by a rectangle. These shapes are also referred to as rounded cap rectangles (RCR) by some authors (Azéma and Radjai, 2012). It is interesting to investigate whether the trends observed for ellipses extend to capsules, as this may indicate general properties of grains as their shape is elongated. Once again, such objects can be seen as a generalization of a circle. In this case, the elongation of the particle can be defined by a constant η, which takes a similar role as aspect ratio in ellipses (Azéma and Radjai, 2012). As elongation increases, packing fraction initially increases, then decreases with the peak occurring at $\eta = 0.4$. Z behaves similarly to ellipses and ellipsoids, increasing until reaching an asymtote at around $\eta = 0.2$. The similarity in behavior between ellipses and capsules implies there may be general packing characteristics that persists across many elongated particle shapes. Chapter 5 investigates whether such behavior is indeed universal among a large class of morphologies.

Another class of shapes commonly considered are polygons. Novel DEM variations were created in the last 10 years which could handle larger variety of shapes, though were not able to handle arbitrary shapes as in LS-DEM (Kawamoto et al., 2016). One such method which could simulate polygons was used to investigate shapes with 2 to 11 sides (Wang, Dong, and Yu, 2015). Polygons were separated into two classes:

those which could fill a plane perfectly (squares, triangles and hexagons) and the rest which can not. It was observed that the random close packing of plane filling particles was generally higher than all others. Nevertheless, the triangle had the lowest packing fraction of plane filling shapes, with a packing fraction comparable with circles. These behaviors persisted across a range of friction coefficients. Coordination number Z generally increased with number of edges. Triangles have a relatively low coordination number due to the 3-particle neighbor tessellation, compared to shapes such as circles which have more neighbors in hexagonal packing. On the other hand, hexagons have the largest Z and break the trend of Z increasing with sides. This is due to the 6-neighbor tessellation which naturally forms under random deposition. Such results also raise questions regarding generalizability. Do shapes which are approximately polygonal, but contain some imperfections, follow similar trends? How far can one deviate from a polygon and still maintain a similar packing fraction? Such questions are relevant towards grain design, as their answers may explain which morphological characteristics are most critical for achieving a given mesoscopic state. These are the questions which are further explored in this thesis, in particular Chapter 5.

Real granular materials found in nature are not ellipses or regular polygons, and are better described by such measures as roundness, aspect ratio, sphericity and convexity. Roundness measures the 'bumpiness' of a particle, aspect ratio and sphericity measure elongation while convexity measures the amount a grain is indented. For stricter definitions, see Equations 3.1, 5.1, 5.3, and 5.2. As pre-LS-DEM methods struggle to capture the level of morphological complexity in real grains, there exists a paucity of computational studies exploring the effects of these real morphological parameters with most quoted values originating from experimental studies (Cho, Dodds, and Santamarina, 2006a). That being said, there has been increased interest in highly non-convex particles in the last decade. Non-convex 3d staple-shaped particle can pack extremely loosely (Gravish, Franklin, et al., 2012). These particles can be described by the ratio of their length to width. As this ratio increases, ϕ decreases from about 0.25 to 0.1. These packing fractions are substantially lower than those observed in ellipses, ellipsoids or regular polyhdrons. 2d non-convex particles have also been investigated by attaching 3 circles together (Saint-Cyr et al., 2011). The non-convexity can be increased by controlling the distance between circle centers. Interestingly, it is discovered that increasing non-convexity initially leads to an *increase* in packing fraction followed by a decrease as non-convexity increases. This implies the relationship between non-convexity

and packing fraction may not be simple, as small non-convexities could lead to interlocking which increases ϕ. It is important to note that this study considers polydisperse grains, i.e. mixtures of grains with different sizes. Thus, the results can not be directly compared to results which consider monodisperse (same size) particles.

For attempting to control granular materials by changing grain shape, obtaining a general mapping between particle morphology and ϕ or Z that can be quickly evaluated would be invaluable. Such patterns described above can be understood as subspaces of the function mapping morphology-to-mesoscale. While the limitations of traditional DEM have prevented numerical investigations into general mappings, there have been significant theoretical attempts. In (Baule and Makse, 2014), a methodology for calculating the approximate packing fraction and coordination number for arbitrary shaped particles is proposed. In this methodology, a grain is decomposed into an addition of Voronoi volumes of spheres to calculate the voronoi volume of the particular shape. The authors derive a formula for ϕ and Z using the particle's voronoi volume representation. This groundbreaking study created one of the first instances of a 'shape space': a general mapping between many particle shapes and mesoscopic properties. The authors propose that such an algorithm can be used for optimization, as one can search for the shape that extremizes Z and ϕ using their formula. However, this theoretical calculation does not match numerical and experimental results exactly and is therefore not equivalent to performing a numerical or physical experiment. As such, it is unclear if the results of topology optimization using this methodology will bear results which match simulations and experiments.

In the thesis, we develop a tool for controlling particle shape given a morphological property, such as roundness and aspect ratio (Chapter 3). We also develop a generalized mapping from morphological properties to mesoscopic properties. This mapping can be inverted to perform topology optimization of granular materials. For instance, attempting to find the particle morphology that when packed in bulk gives a particular packing fraction ϕ.

2.4 Modeling excavation

We now shift attention to modeling excavations. Excavation in granular materials can be seen as an optimization, where the controlled variables are which grains to remove and the optimized variables are the desired size and stability of the tunnel

(Table 1.1). A focus of this thesis is on understanding and controlling ant tunnel-like unreinforced excavations in soils, i.e. tunnels without additional support such as linings and rock bolts in irregular-shaped grains. Yet most tunneling studies focus on reinforced tunneling as this is most relevant to human excavation, particularly when tunneling in soils rather than hard rock. Still, studying reinforced tunneling can provide great insight into phenomenon such as soil arching which also is highly relevant for unreinforced excavations.

Reinforced tunneling in granular materials is intimately linked with arching in granular materials. Such a phenomenon was studied by Terzaghi who stated that a loosened zone was created around the tunnel during construction with the loosened zone's weight supported by rock surrounding the tunnel (Chen, Huang, and Tseng, 2011). Terzaghi explored soil arching in greater detail in his treatise 'Theoretical Soil Mechanics' (Terzaghi, 1943a). Here, Terzaghi states 'arching is one of the most universal phenomenon encountered in soils' and occurs when one part of a soil yields, for instance during tunneling. In this case, 'the relative movement within the soil is opposed by a shearing resistance within the zone of contact between the yielding and stationary mass' which 'reduces pressure on the yielding part of the support and increases pressure on the adjoining stationary parts.'

Reinforced tunnels in granular media have been extensively studied throughout computational mechanics literature. Most studies take a continuum approach to tunneling, using models such as the finite element method (FEM) to study excavations. When grains are very small, such as in large scale excavation in clay, it is reasonable to use continuum models as simulating each of the billions of particles involved in DEM would be prohibitively computationally expensive. This is common in human-scale excavation to avoid tunnel collapse. For instance, Lin et al studied the change in material stress around an earth pressure balance shield (EPBS) during the process of tunnel excavation in sandy soil, incorporating a tunnel lining (Lin et al., 2019). The authors leveraged a 3D FEM simulation with a Mohr-Coulomb failure criterion. A Mohr-Coulomb failure criterion is a generalization of Coulomb friction to a continuum, and dictates when and how an isotropic, frictional brittle material (such as soil) will failure in tension (Labuz and Zang, 2012). A zone of low stress due to soil arching develops around the tunnel during excavation. This loosened zone expands primarily upwards and in front of the tunnel gradually during tunneling. The authors also quantify the depth at which soil arching occurs by identifying an inflection point in vertical stress $\sigma_z(z)$, where z is vertical depth.

This methodology is similar to that used in earlier studies (Chen, Huang, and Tseng, 2011).

Constitutive modeling in FEM is efficient compared to discrete-scale studies. Nevertheless, FEM has numerous disadvantages compared to DEM: constitutive models like Mohr-Coulomb can not capture all relevant physical effects (Guo and Zhou, 2013) and depend on many ad-hoc variables to capture the effects of microscopic properties such as particle shape (Yin, Wang, and Zhang, 2020). With increased computation, recent studies have attempted to model tunneling using the DEM. Most computational studies use spherical particles due to limitations of traditional DEM. Earlier 3D DEM studies of reinforced excavation observed similar arching effects around the tunnel as in FEM studies (Chen, Tang, et al., 2011). Further, it was identified that as the horizontal displacement of the tunnel excavation grows, the support pressure (pressure on the tunnel surface) decreases to a value known as the 'limit support pressure' as arching occurs. Next, as the tunnel horizontal displacement continues this stress will in fact grow to a value known as the 'residual support pressure.' More recent studies have considered the effects of particle shape in excavations using sphere clustering in DEM. In (Yin, Wang, and Zhang, 2020), a coupled FDM-DEM (finite difference method — discrete element method) is used to probe the effects of particle shape on 3D lining-reinforced tunneling. Near the tunnel, a DEM is used to capture the large deformation behavior and arching. The FDM is employed far from the tunnel surface due to the relatively smaller strains in these areas, thereby minimizing unnecessary computational expense. 3 types of particle shapes are investigated: spheres, elongated particles (2 clustered spheres), and 4 clustered spheres in a tetrahedral configuration. A model of a tunnel boring machine is used to construct the tunnel by first excavating forward to create the tunnel, then backwards. Similar to previous studies, it is seen that a large arching zone occurs both infront and around the boring machine, greatly reducing stress near the surface of the tunnel. Further, the authors discover that the deformed area around the excavation is highly dependent on particle shape. During backwards movement of the boring machine, spherical grains have much larger deformation than other shapes. The authors suggest this could be due to material dilation. More angular particles also lead to a lower supporting force around the tunnel, potentially due to increased arching effects as grains interlock. These studies imply arching plays a significant role in granular excavation, and its general behavior can be captured with spherical particles. However, if one wishes to capture the behavior of a specific soil, using the correct particle shape may be essential (at the cost of computational

expense).

As stated above, unreinforced tunnels in soils are not as extensively studied in literature due to lack of application. On the other hand, clogging of silos has been heavily scrutinized in granular mechanics research. A silo can be viewed as a container with a hole in the bottom. If a granular material flows through the hole it may form an arch at the hole, 'clogging' the silo. Such a clog is similar to an unreinforced tunnel, with the stability of the arch dependent upon grain-scale forces and not external support. Thus, we review relevant studies on silo clogging. Silo clogging is usually considered from a probablistic perspective. A recent experimental study investigated the clogging probability of grains with a range of morphologies flowing through orifices of different sizes (Hafez et al., 2021). The shapes considered were 3D crosses, '2D' crosses (cross prisms), cubes and spheres. It was found that for all shapes as the size of the orifice increased the probability of a clogging arch forming decreased with the hole size following a logistic curve as a function of orifice size. As such, clogging probability was approximately 1 for low orifice sizes, until a critical orifice size value where the probability rapidly decreases to zero. Cubes had the largest critical orifice size, followed by 3D crosses, then 2D cross and finally spheres. The authors claim this is due to cubes forming stable beam-like structures at the orifice and entanglement of cross-like particles. This study demonstrates both the probabilistic nature of granular arching, and how the stability of unreinforced tunneling is strongly dependent on particle morphology. Analytical studies have also derived formulas for predicting the critical arch width and height for cohesive and non-cohesive granular materials, discovering that while arch width depends on cohesion arch height is a function of the material's internal friction angle (Guo and Zhou, 2013). DEM has also been used to study the effects of cohesion on arch formation. In (Morrissey, Ooi, and Chen, 2013), spherical particles flow through an orifice. Different amounts of cohesion are studied, with cohesion modeled as an attractive force between non-contacting grains. As cohesion is increased, the distance between grains at which the cohesive force acts increases. With increasing cohesion, the critical orifice size for the material increases. Arches which form at the orifice also become taller at intermediate cohesive strengths. Finally, similar to reinforced tunnels significant arching effects around the orifice are observed. These results imply cohesion and particle shape all play a substantial role in arch stability.

Most studies of tunneling in unreinforced soils are either theoretical or based on

continuum FEM simulations (Di Prisco et al., 2018; Yuliza et al., 2018). Such studies usually rely on limit analysis theory, predicting upper bounds on stable tunnel geometries given particular soil characteristics (Huang, 2014) or assume highly ordered grain packings. However by not modeling the material at the grain scale, as in DEM, certain important characteristics of tunneling are missed. As demonstrated above, DEM simulations can capture the probablistic nature of arching and can directly model the impact of grain shape on soil stability. Studies which do model unreinforced tunnels at the grain scale usually pertain to jointed rocks. Rocky materials can form arches due to the large size of the individual rock joints and blocky shapes of the joints. Such behavior is explored in (Do and Wu, 2020), where discontinuous deformation analysis (DDA) (Goodman et al., 1984) is used to evaluate the stability of tunnels in jointed rocks. Similar to the previous studies, a low-stress region forms around the opening, with forces forming 'arches' around the low stress zone. Further, the authors discover the stability of these arches depends heavily on the angular orientation of the rock joints.

There are few works that investigate unreinforced tunneling in soils at the grain scale. The work in thesis aims to fill this gap by performing DEM simulations of unreinforced tunnels in soils.

2.5 Predicting stability of unreinforced tunnels

In order to control the stability of unreinforced tunnels, it is necessary to first predict the stability of the tunnel when particular grains are removed. While theoretical methods such as limit analysis theory can supply upper bounds on tunnel size in a particular soil, there is no robust method for predicting the stability of specific unreinforced tunnels in granular materials (Di Prisco et al., 2018). Similar work has focused on predicting whether an arch will form when grains are flowing through an orifice. This study discovered that arch stability could be estimated by measuring the angle between contacting grains in the arch. If the contact angle exceeded 180 degrees, the probability of arch stability decreased dramatically. Such high-angle contacts were termed 'defects' (Lozano et al., 2012). Though, it is unclear if such results generalize to tunnels rather than clogging arches and to non-circular particles.

With these results in mind, the author of this thesis collaborated on a project to predict the stability of unreinforced non-cohesive granular tunnels in soil with realistically shaped grains (Pal, Buraque de Macedo, and Andrade, 2021). In this study, a 2D

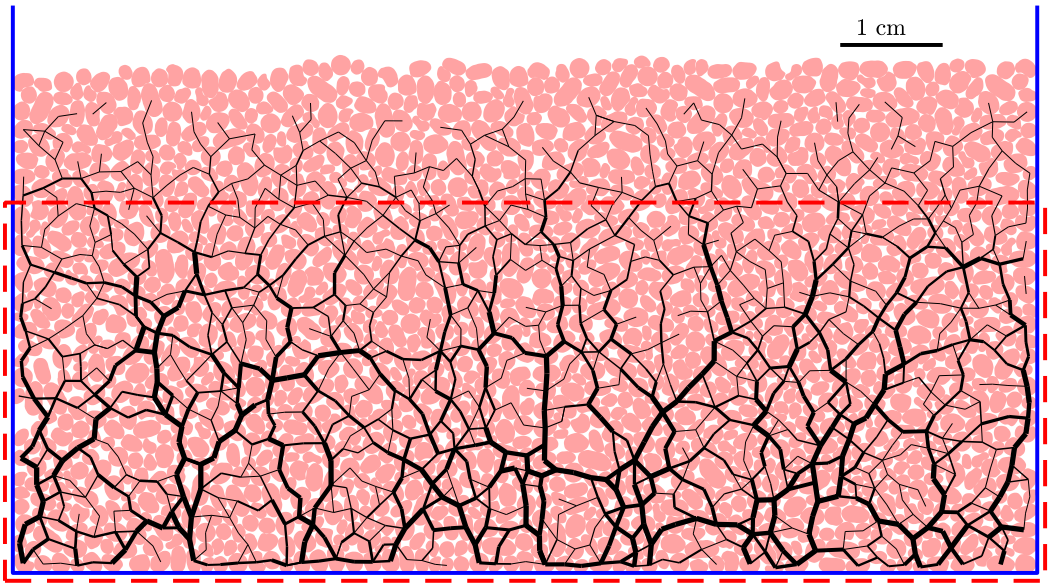

Figure 2.1: 2D cross section of soil, with grain shapes cross sections of particles imaged from XRCT. Black lines indicate contacts forces obtained from LS-DEM, with contact force strength proportional to line thickness (Pal, Buraque de Macedo, and Andrade, 2021).

cross section of a granular soil was considered, see figure 2.1. Grain shapes were obtained from cross sections of particles imaged via XRCT. The goal of this study was to discover whether there existed a formula for predicting the stability of a tunnel formed from grain removal. In this case, a 'tunnel' is in fact a tunnel cross section, i.e. a set of contiguous grains removed in the 2D cross section. An ant does not have access to all information in the material when digging, but rather just on the surface of the tunnel. As we were interested in the studies' relevance to ant tunnels, we attempted to see if a 'local' criterion could be discovered, i.e. a criterion for stability which only used information on the surface of the tunnel. Further, as ant tunnels tend to have a constant radius (Buarque de Macedo, Andò, et al., 2021) we dug tunnels of predefined diameters.

The first stage of the study consisted of equilibrating the soil particles in LS-DEM to obtain the interparticle forces, see Figure. 2.1. The next stage consisted of creating constant radii tunnels at random points in the soil, and investigating what properties controlled granular stability. Examples of tunnels before and after excavation are given in Figure 2.2. It was quickly discovered that removing grains under high interparticle forces (thick black lines in Figure 2.2) was more likely to induce a collapse than removing grains under low interparticle forces. To quantify the

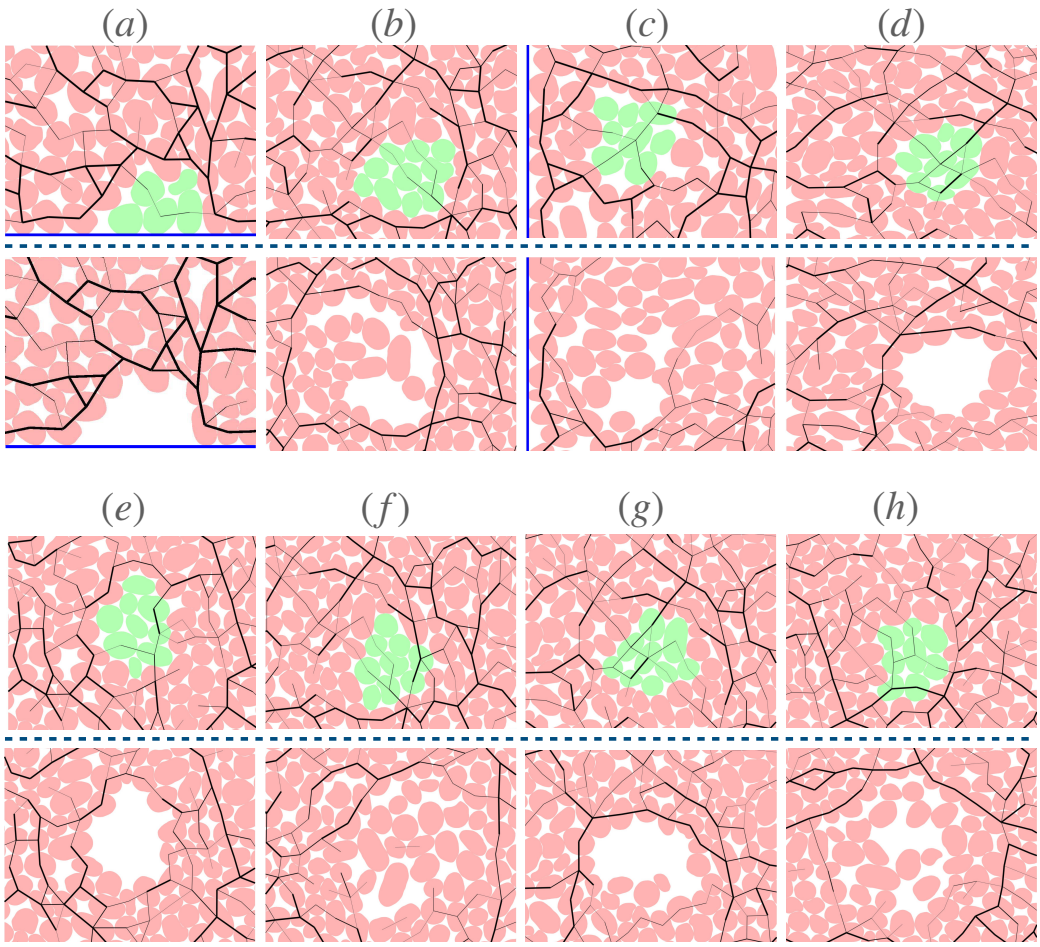

Figure 2.2: Examples of tunnels before (above dotted line) and after (below dotted line) excavation (Pal, Buraque de Macedo, and Andrade, 2021).

amount of force on a candidate set of grains for removal, we calculated a quantity f_p, with f_p given by Equation 2.1, where F_{ij} is the contact force between particles i and j, x_i is the position of particle i and R_t is the radius of the tunnel.

$$f_p = \sum_{i,j;i<j}^{N} \alpha_p(i,j)|F_{ij}|, \quad \alpha_p(i,j) = \begin{cases} 1 & \text{if } \min(|x_i - x_p|, |x_j - x_p|) < R_t \\ 0 & \text{otherwise.} \end{cases} \tag{2.1}$$

Tunnels with the 40 lowest and highest f_p for a given R_t were dug. It was discovered that grains with the 40 lowest f_p were occasionally stable, while none of the tunnels with the 40 highest f_p were stable. This can be considered the 'Jenga' principle: removing grains under low interparticle forces is more likely to be stable than removing grains under high interparticle forces in dry granular materials. This is

similar to how one may play Jenga, feeling the force on a block to determine whether its removal will cause a collapse. We restricted our attention to tunnels with the 40 lowest f_p.

Then, we investigated whether tunnel stability could be predicted *a priori* using local variables. First, we investigated the 'angle criterion': if tunnels were universally unstable when angles between contacting grains on the tunnel surface exceeded 180 degrees and vice-versa. Indeed, many tunnels with low contact angles formed arches when grains were removed (Figure 2.2 d,g). On the other hand, some tunnels with low contact angles between grains were still unstable. We hypothesized this was due to unbalanced forces on the removed grains, i.e. the 'Jenga' principle. In fact, it has been conjectured that ants use the amount of force on grains to determine whether it is suitable for removal (Frost et al., 2017; Espinoza and Santamarina, 2010). A new criterion was developed which judged tunnel stability by the imbalanced force on grains on the tunnel surface if the grains that will be removed (green particles in Figure 2.2). Again, while such a criterion was successful in many cases (Figure 2.2 a,d,f) certain tunnels with high unbalanced forces were in fact successful in forming a stable arch under grain removal (Figure 2.2 e).

Finally, we questioned whether it was even possible to develop a general stability criterion for granular tunnels using local information alone. In other words, is it feasible to always correctly predict the stability of a granular tunnel using grain shape, positions and forces on the tunnel surface *a priori*? To check this, we first removed grains to create a tunnel. Then, instead of simulating all the grains in the material, we only simulated grains within four particles of the tunnel surface. On the outside of the outermost layer of the local domain, grains at the top are replaced by directly applied forces matching the forces on the top layer prior to excavation. Meanwhile, grains below the domain are fixed to their original position, see Figure 2.3 a. We discovered that certain tunnels were stable in the local situation, but not when all grains in the domain are considered (and vice-versa). This implied that the tunnel excavation problem in dry granular materials is inherently non-local, i.e. predicting whether a given tunnel will be stable with 100% accuracy is infeasible using only information on the tunnel surface.

Finally, we attempted to explore *why* the problem was inherently non-local. The change in contact forces around a tunnel due to excavation was visualized (Figure 2.3 b). Clearly, the influence of the tunnel extends far beyond the tunnel surface. This lead us to believe that the behavior of the tunnel is linked to the mechanics

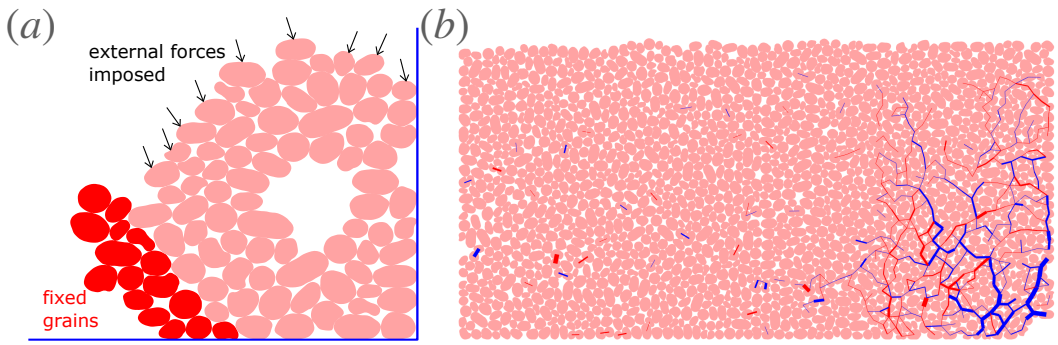

Figure 2.3: The local granular tunnel problem. (a) Diagram of grains simulated in the 'local' problem. Grains at the bottom of the domain are fixed while grains above the domain are removed and replaced by forces matching the initial contact forces. (b) Change in grain-grain contact forces due to an excavation about a stable tunnel. Grain contacts with increased force are blue, while decreased are red (Pal, Buraque de Macedo, and Andrade, 2021)

of grains far from the surface via force chains, making exact prediction of tunnel stability from local considerations alone generally infeasible in dry environments. To extend these results to real ant tunnels, one must consider the effect of cohesion and 3 dimensions. These parameters are explored in Chapter 4 of this thesis.

Chapter 3

GRANULAR OBJECT MORPHOLOGICAL GENERATION WITH GENETIC ALGORITHMS FOR DISCRETE ELEMENT SIMULATIONS

PUBLISHED CONTENT AND CONTRIBUTIONS

Buarque de Macedo, Robert, Jason Marshall, and Jose Andrade (2018). "Granular object morphological generation with genetic algorithms for discrete element simulations." In: *Granular Matter* 20.4, pp. 1–12.
R.B. helped with the conceptualization of the project, wrote the relevant code, analyzed the data, and wrote the manuscript.

A granular material is a collection of discrete, solid particles with examples including sand, ice floes, soil, and in general any assembly of discrete objects. These materials are ubiquitous and are found in many industries from food production (stacking of foodstuffs) to civil engineering (soil mechanics) (Sperl, 2006; Hyslip and Vallejo, 1997). The Discrete Element Method (DEM) is one common technique for simulating granular particle dynamics (Cil and Alshibli, 2012; Cundall and Strack, 1979a; Vu-Quoc, Zhang, and Walton, 2000; Kawamoto et al., 2016). However, many challenges arise when simulating these materials including the large number of grains in an assembly, efficiently calculating contact between grains, and how to accurately reproduce particle shape. In this work, we discuss new methods that accurately reproduce particle shape and develop algorithms for generating new unique shape morphologies for simulation from a smaller subset of input data.

When simulating a granular material via the DEM, one must decide the shape of the computational grains. A natural first choice is to represent particles as spheres. Spherical particles are common because calculating particle intersections and hence forces are fast and easy (Kruggel-Emden et al., 2007). However, real grains are in general not spheres (Kawamoto et al., 2016). Multiple studies have demonstrated that particle morphology affects macroscopic granular material properties (Cho, Dodds, and Santamarina, 2006b; Kawamoto et al., 2016; Lim, Krabbenhoft, and Andrade, 2014; Guo and Su, 2007), highlighting the importance of granular shape. A concrete example is that non-spherical particles can exhibit interlocking between grains, which effects the shear resistance of the material (Guo and Su, 2007).

Numerous methods have been proposed for simulating non-spherical particles. The cluster approach consists of building each non-spherical particle out of multiple spherical particles, allowing contacts between particles to be calculated sphere-by-sphere (Vu-Quoc, Zhang, and Walton, 2000). However, this method leads to bumpy grains that may not be physical (Kawamoto et al., 2016). It has also been shown

that increasing the number of spheres used to build a particle, while improving morphological accuracy, can have a negative effect on simulation results (Höhner et al., 2011).

Polyhedra have also been used to model non-spherical particles in the DEM (Cundall, 1988). Using polyhedra, any set of geometries can theoretically be modeled. However, achieving a high resolution particle morphology requires many polygons per particle, and thus can be computationally expensive (Lim, Krabbenhoft, and Andrade, 2014). Furthermore, it has been shown that these models suffer the same morphological/mechanical accuracy tradeoffs exhibited by clustered sphere models (Höhner et al., 2011).

Recently, the Level-Set Discrete Element Method (LS-DEM) (Kawamoto et al., 2016) was developed, which can simulate morphologically accurate and arbitrarily shaped grains. This method captures granular behavior to an extent unmatched by traditional DEM approaches and reproduces experiments with high accuracy (Kawamoto et al., 2016; Kawamoto et al., 2018). However, this method requires shape data for each grain in the simulation. One option for obtaining this data is to take high-definition three dimensional images of each grain with techniques such as x-ray computed tomography or laser scanning. This data collection approach, while highly accurate can be time-consuming and cumbersome for simulations with 10,000s of particles. Consequently, a method for generating large quantities of realistic computational grains without having to obtain images of every particle is highly valuable.

Granular cloning is one approach to reduce the challenge of collecting exact particle shape morphologies (Cobo, 2016). The cloning procedure starts by gathering data of particle shape morphologies and creating particle avatars, these are the parent particles. For an example of these parent particles, see Figure 3.1. New clone particles are then generated from features of the parent particles. This generation process could take many forms including perturbing existing particles geometries or by randomly sampling from the distributions of morphological properties of the parent particles. Examples of these properties include sphericity, roundness, and roughness (Cho, Dodds, and Santamarina, 2006b). In this process, each clone is unique from other clones and parent particles, yet the collection of cloned particles would match the overall shape distributions of the granular material. Thus, from images of a small number of grains, an indefinite number of computational grains can be generated with realistic variation in morphological properties. These grains

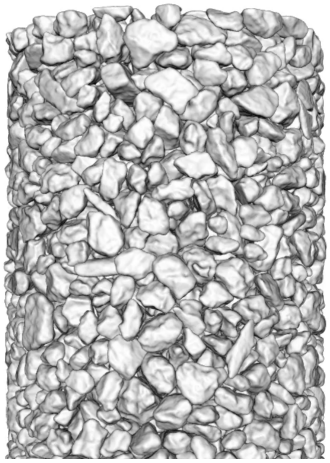

Figure 3.1: Exact grain morphology captured from 3D XRCT. These objects are morphologically accurate computational representations of the particles which will be cloned. In other words, each computational avatar has the same shape as an imaged physical particle, from (Kawamoto et al., 2016).

can then be used in simulations.

An initial example of this type of method was recently developed (Cobo, 2016). In that work, each avatar obtained from XRCT imaging is represented as a function of polar and azimuthal angle $r(\Phi, \Theta)$. The value of r, or the radius, at a given Φ and Θ is the distance from the particle centroid to the surface of the particle. Distributions of r for each of the two angles are gathered by performing measurements across each grain avatar. In addition, particle roundness and the lengths of each particle's principal axes are recorded.

Clones are then generated from the collected data. First, an equivalent ellipsoid is built by randomly sampling principal axes values from the parent principal axes distribution. Following this, for each Θ and Φ on the clone, a new radius value is sampled by using data from the parent particle distribution of $r(\Phi, \Theta)$. The ellipsoid surface is perturbed to fit this new radius. The cloned particles are then smoothed until the roundness matches a chosen value from the parent particle roundness distribution. The result is a clone particle that is distinct from all parent particles, but fits certain morphological properties of the original grains (Cobo, 2016).

Another cloning method uses spherical harmonics (Neil and Russ, 2012) and principal component analysis (PCA) (Wold, Esbensen, and Geladi, 1987) to generate new particles. This method first decomposes the voxelated images of each particle into spherical harmonics, i.e. finding the vector representation of each particle in

a basis formed by spherical harmonic functions, given that each particle is a function mapping polar and azimuthal angle to radius of surface at said angles. As each particle is represented by an infinite series of spherical harmonic functions, a maximum number of basis functions are chosen such that the accuracy of the series representation is sufficient. Then, each particle is represented as a point in a high dimensional space, where the i^{th} dimension is the particle's i^{th} spherical harmonic coefficient. Once a large number of points have been obtained by sampling many particles from the granular material, PCA is performed to reduce the space to a lower-dimension with an orthogonal set of coordinates to the original coordinates, such that the points in this space maintains most of the variance of the original distribution. This space is said to have the principal components (PCs) as a basis. Finally, new clones are generated by picking a value for each principal component of the clone from a normal distribution with a mean of zero and a standard deviation derived from particle diameter distributions. These values are then projected from PC space into the spherical harmonic space and a clone is constructed (Zhou and Wang, 2016).

In this work, a new granular cloning method is developed that uses genetic algorithms to build cloned particles that accurately capture distributions of any shape properties, including roundness and sphericity. These properties can be sampled from parent particles or directly provided. An advantage of this method is the ability to build particles from specified, suitably defined, properties, thereby allowing the investigation of granular materials with any desired morphological characteristic. We demonstrate this method by generating clones which match the roundness and sphericity distributions of the parent particles. Distributions of these clones are compared against the original parent distributions to validate the cloning process. The potential applications of this method are widespread, including building libraries of computational grains for granular material simulation without the need for extensive imaging. Furthermore, by being able to generate particles from different morphological properties, our method can be used to finely control shape parameters and understand their importance in the physics of granular media.

3.1 Methods

Measurement of Morphological Properties

We focus on generating particle clones using morphological properties, specifically sphericity and a length scale dependent measure of normalized principal curvature. As roundness is related to this second property in particular circumstances, our

clones match the sphericity and roundness of the parent particles. Sphericity is an approximate measure of how much a particle deviates from a sphere (Wadell, 1935), see 3.1,

$$\Psi = \frac{\pi^{\frac{1}{3}}(6V_p)^{\frac{2}{3}}}{A_p}, \tag{3.1}$$

where V_p and A_p are the volume and area of the particle and are calculated in this work from meshes of a particle surface. Sphericity was chosen as a property for inclusion in the cloning method due to the ease of numerical measurement and its effectiveness at capturing particle morphology at a large length scale (Cobo, 2016).

Normalized principal curvatures were also chosen as a target property because commonly used geomechanical properties like roundness and roughness (Neil and Russ, 2012; Cho, Dodds, and Santamarina, 2006b) are related to the variations in curvature on the particle surface. According to Cho, Dodds, and Santamarina (2006b) roundness describes the scale of major surface features which are typically one order of magnitude smaller than the particle size and is quantified as the average radius of curvature of surface features relative to the radius of the maximum sphere that can be inscribed in the particle. Additionally, according to Hyslip and Vallejo (1997), roughness is the general shape and surface irregularity, of particulate soil. Hence, curvature captures the essence of these classical geotechnical properties. In general, curvature κ is the rate at which the unit tangent $\hat{t}$ changes with respect to s (arc length) (Riley, Hobson, and Bence, 2006), see Equation 3.2. Thus, a low curvature at a given point indicates that the surface is flat near the point. On the other hand, a high curvature signifies bending of the surface near this point.

$$\kappa = \left|\frac{d\hat{t}}{ds}\right| \tag{3.2}$$

In this work, particles are represented as two dimensional surfaces in three dimensional space. At a point on a two dimensional surface in three dimensional space, there will be a different curvature in every direction. The principal curvatures are the direction and magnitude of the largest and smallest curvatures at said point. Thus, we record the magnitude of principal curvatures at a given point i.e. the maximum and minimum curvatures, see Figure 3.2. The curvature measured at points of interest, using reference points spaced close to the point of interest, will be a quantitative measure of particle irregularity. The rougher the particle, the higher the curvature.

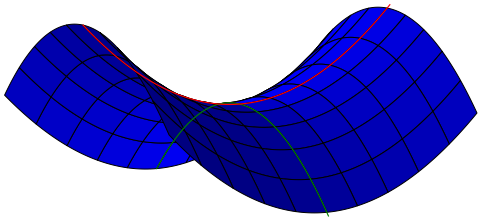

Figure 3.2: Principal curvatures at a point will be the minimum and maximum curvature at said point. For example, at the saddle point of the hyperbolic paraboloid pictured above, the principal curvatures will be the curvatures of the red and green curves at the point.

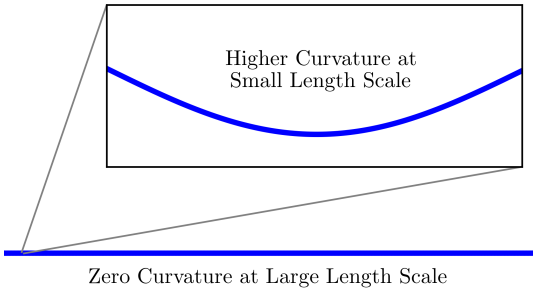

Figure 3.3: Measuring curvature at a point is dependent on the length scale of interest. For example, a rapidly oscillating function appears flat on a large length scale, yet has a high amount of curvature on a small length scale.

There is an additional subtlety for curvature, however. Given a set of discrete points representing a continuous surface, the curvature at a given point will vary depending upon which points surrounding the given point are used to calculate curvature. For example, consider a seemingly flat line which, upon closer inspection, is in fact very rough, see Figure 3.3. Furthermore, this line is represented by discrete points. Measuring the curvature at a given point on the curve requires choosing a set of surrounding points as references; one point alone is not sufficient information for a curvature calculation. If reference points are chosen such that the distance between the reference points and the point of interest is far greater than the perturbations in the curve, they will record a small curvature indicating a flat line. However, if reference points are picked such that the distance between the reference points and the point of interest is on the order of the oscillations in the curve, they will record a high curvature. We may record properties of a discrete function at multiple resolutions by picking different reference points for calculations of curvature at a given point.

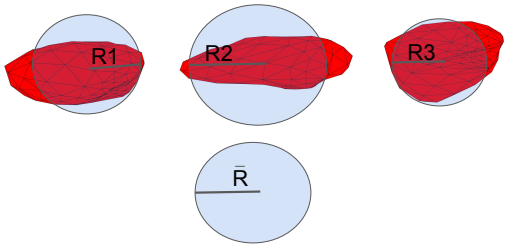

Figure 3.4: A particle, viewed along each of its principal axes. For each alignment, a sphere is generated with radius equal to the particle's extent along the principal axis. These radii are averaged to obtain $\bar{R}$.

We utilize this multiple resolution capability to measure the mean and standard deviation of principal curvatures on a particle surface at different length scales. The length scale denotes the distance between points of interest and reference points for calculating curvature. The smaller the length scale, the smaller the distance between reference points and points of interest. By finding curvatures at different length scales, a holistic quantitative understanding of granular shape morphology can be captured. For example, roundness is related to the curvature of bumps roughly the size of the diameter, D, of the particle divided by 10. Consequently, by measuring curvatures of the particle using reference points separated from points of interest by distances of about $\frac{D}{10}$ on the particle surface, we will achieve an approximate measurement of particle roundness.

Nonetheless, this discussion is incomplete: principal curvature alone is a size dependent property. For example, two spheres with different radii will have different principal curvatures. Yet, we are trying to characterize particle shape, not size. Curvature, thus needs to be normalized so there is a size-independent measure of particle shape. Normalizing the curvature of a particle occurs by first aligning the particle to its principal axis. Then, the distance of the particle's surface to the centroid along each of its three principal axes is calculated — denoted by R_1, R_2 and R_3. These three values are averaged to obtain the radius $\bar{R}$ of a sphere that is approximately the size of the particle, see Equations 3.3 and 3.4.

$$\bar{R} = \frac{R_1 + R_2 + R_3}{3} \tag{3.3}$$

Given previous definitions of roundness (Cobo, 2016; Cho, Dodds, and Santamarina, 2006b), the averaged radius ($\bar{R}$), and the average maximum principal curvature

measured on the $D/10$ length scale (C_{max}) we define the roundness of a particle in 3.4. The maximum principal curvature is chosen because we believe this direction captures the greatest irregularities in a surface feature at a given point.

$$\text{Roundness} = \frac{1}{\bar{R}C_{max}} \tag{3.4}$$

Granular Cloning Method Overview

The granular cloning method developed takes as input either morphological property distributions of parent particles directly, or extracts these distributions from parent particle data. In this paper, morphological distributions are extracted from particle data, though this is not to imply that direct input of morphological data is not worth consideration, and may in fact be preferable depending on the situation. Specifically, sphericity, normalized principal curvature distributions, and volume are captured for approximately 1000 particles. After these characteristics are measured from images of the parent particles, the process detailed below is repeated for the generation of each clone.

1. An ellipsoid is generated with a randomly chosen sphericity and volume from the parent particle sphericity and volume distribution.

2. A surface mesh is created for the particle.

3. The particle surface mesh is deformed until the normalized principal curvature distribution (see Section 3.1) matches a randomly selected mean and standard deviation of per particle curvature sampled from the curvature distributions of the parent particles. Particle deformation follows an optimization process, where the difference between the cloned particle's normalized curvature distribution properties and the randomly selected curvature distribution properties are minimized by changing the position of vertices on the particle surface.

4. The process is then repeated on any number of smaller length scales for the cloned particle by perturbing vertices at the smaller length scale on a finer mesh. Larger length scale perturbations modify the general shape of the particle, while smaller length scale deformations maintain the large scale structure of the particle, but add small local deviations from the overall particle shape - which affect the roundness of the particles.

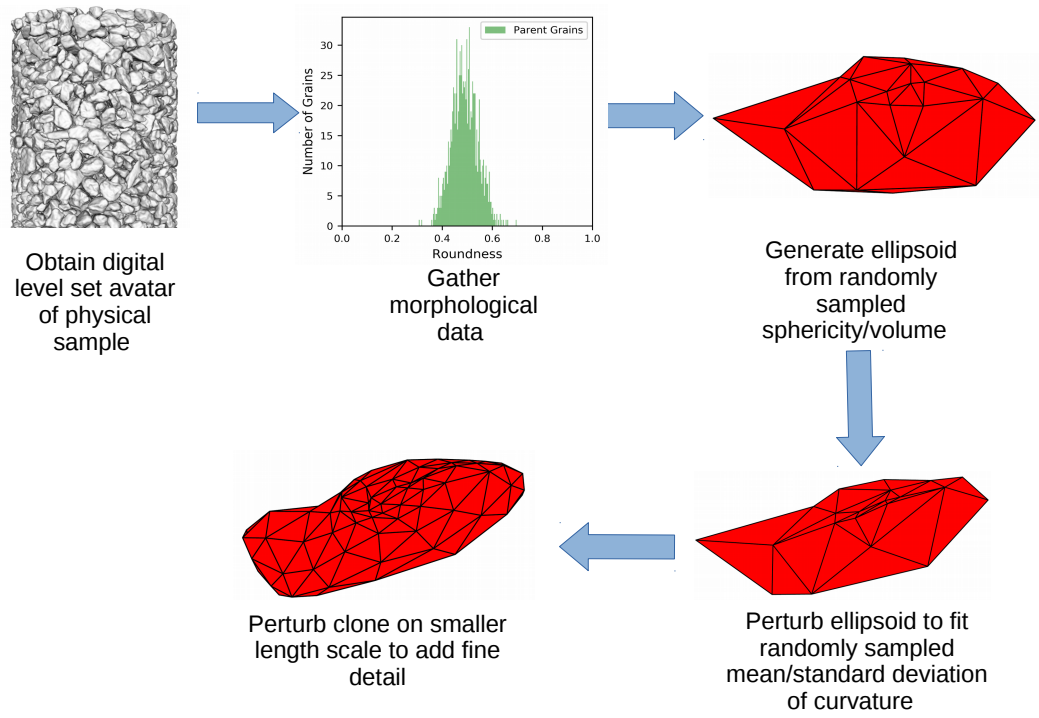

Figure 3.5: Overview of granular cloning method.

Figure 3.5 shows an overview of the general method.

Curvatures at a given vertex are independent on different length scales. A particle may have a generally flat shape, leading to a small curvature on large length scales. Nonetheless, this same particle could be rough, leading to large curvatures on smaller length scales. We differentiate between these lengths scales for sampling data and particle construction so that we can capture this variability in structure across distinct resolutions.

Currently, the optimization process is run on two length scales in order to capture particle sphericity and roundness, though the method can be used to generate grains on any number. Once the optimization process is completed on both length scales, the cloned particle has been formed. This process is then repeated until the required number of grains has been generated. These particles are all unique, and can be converted directly into suitable formats for simulation methods like LS-DEM. It is worth re-iterating that the method may also take as input apriori generated morphological distributions, in which case there is no need to mesh a collection of parent particles.

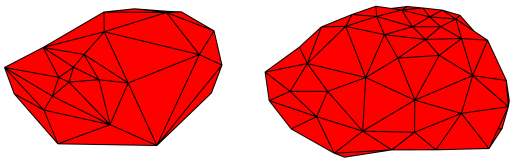

Figure 3.6: A Parent particle mesh. Left: A coarse mesh fit to the parent particle surface. Right: A finer mesh fit to the parent particle surface.

Data acquisition details

The granular cloning method developed herein takes as input level set representations of all the particles in the parent sample. In this case, we use a parent sample size of 1000 grains. After level set data is obtained for each particle, a surface and volume mesh is fit to the zero level set, in other words the surface. In our case, the mesh is generated by passing the level set data into a CGAL meshing library, however any library which can create surface meshes from level set data could be used (Fabri and Pion, 2009). The coarseness of this mesh corresponds to the length scale curvatures/sphericities to be measured via the mesh. For the largest length scale, a particle surface mesh has around 30-60 elements. For the smaller length scale, a particle surface mesh has around 100-150 elements. These numbers are chosen such that modifying elements on the larger length scale corresponds to changing the general shape of the particle, while elements on the smaller length scale are of size on the order of $\frac{D}{10}$. Thus, modifying the smaller elements approximately changes the roundness of the particle. Nonetheless, the size of the elements on a given length scale are not set, and can be modified as much as one desires. A parent particle meshed at the smaller and larger length scale is displayed in 3.6.

Next, the mean and standard deviation of the normalized curvatures are recorded for each parent particle at each length scale, from the volume and surface meshes at the respective length scale. It is important to note that the mean and standard deviation of the principal curvatures across all particles is not what is being gathered. Rather, the mean and standard deviation of principal curvatures across each individual particle is recorded. Consequently, our morphological data extracted from the parent particle level sets is in the form of distributions of mean principal curvature and distributions of standard deviation of principal curvature for both (minimum/maximum) principal curvatures. Principal curvatures are measured via libraries in the open-source software CGAL: The Computational Geometry Algorithms Library (Fabri and Pion, 2009). This particular library in CGAL measures curvatures by taking advantage of

the techniques detailed in Cazals and Pouget (2005). As mentioned in the previous section, these morphological distributions could instead be supplied directly by the user, thereby bypassing the need for analysis of parent particles.

The meshing procedure implemented does not always produce a uniform mesh, in that not all elements in a mesh are the same size, see Figure 3.6. For example, consider the following mesh of a particle surface. On one side of the mesh, vertices are spaced close to one another and elements are very small. On the other side of the mesh, there are a few vertices placed far apart from one another. Consequently, the elements are far larger on this side of the mesh. As a result, moving the vertices that are part of larger elements will change the structure of the particle far more than moving the vertices which correspond to smaller elements, as a larger surface area of the particle will be perturbed by changing the position of the larger element vertices. Thus, element size is taken into consideration when calculating the mean and standard deviation of principal curvatures for a given particle. After calculating the principal curvatures at each vertex, a weight w_i is assigned to each vertex, where w_i is the sum of the areas of the elements that vertex i is part of. This weight quantifies the fact that the position of vertices that are part of larger elements will contribute more to particle properties than that of vertices that are part of smaller elements. Once the principal curvatures and w_i's have been calculated for each vertex, the mean (see 3.5) and standard deviation (see 3.6) of the principal curvatures for the individual particle are calculated as follows:

$$\mu_j = \frac{R \sum_{i=0}^{V} w_i c_{i,j}}{\sum_{i=0}^{V} w_i} \tag{3.5}$$

$$\sigma_j^2 = \frac{\sum_{i=0}^{V} w_i (c_{i,j} * R - \mu_j)^2}{\sum_{i=0}^{V} w_i}, \tag{3.6}$$

where $c_{i,j}$ is the j^{th} principal curvature on the i^{th} vertex, μ_j, σ_j are the mean and standard deviation of j^{th} principal curvature, and V is the total number of vertices on the particle. These distributions of curvature means, curvature standard deviations, sphericities, and volumes are used during clone generation.

Clone generation

In this section, the generation of a unique particle clone is explained. First, a random sphericity and volume are sampled from the respective distributions of the parent particles. Then, the three principal semi-axes lengths for an ellipsoid are chosen such that the ellipsoid matches the volume and sphericity values sampled. This

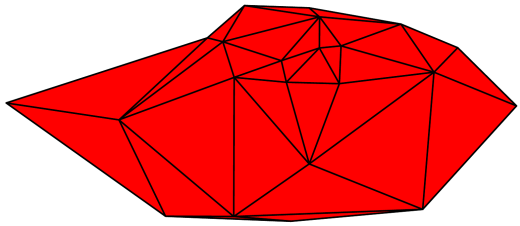

Figure 3.7: Starting coarse meshed ellipsoid for clone.

ellipsoid is the starting configuration of the clone. Next, a coarse surface mesh of the ellipsoid is generated, see Figure 3.7. A volume mesh of the ellipsoid is also constructed, such that the vertices on the volume mesh are the same as the vertices on the surface mesh.

The vertices on the clone mesh are then optimized by minimizing a cost function of the difference of the mean and standard deviation of the distributions of the principal curvatures on the particle from the randomly sampled values, while maintaining the sampled sphericity. As moving one point affects the curvature of all the points around it, perturbing the particle to fit the target properties is a highly nonlinear optimization process. Consequently, genetic algorithms are used to search the non-convex state space for the optimal perturbation of the ellipsoid. Genetic algorithms (GAs) are chosen because GAs have a proven history of solving non-convex optimization problems efficiently when the search space is essentially unknown (De Jong, 1988).

GAs use evolutionary techniques to find the value of a variable or variables that minimize a given cost function. The general GA procedure is outlined below. First, a set of trial solutions to the optimization problem are proposed. These solutions are the individuals, and may be randomly chosen or pre-selected. Then, the trial solutions are evaluated; the individuals with the highest cost are discarded. Subsequently, the properties of the remaining individuals are combined, or mated, to create new individuals with a combination of the older solutions' properties. Finally, a randomly chosen subset of the current solutions are randomly perturbed, or mutated, to obtain a slightly modified set of trial solutions.

This process is repeated until one of the solutions has minimized the cost function sufficiently (De Jong, 1988).

In the case of the developed granular cloning method, the individuals targeted for optimization are surface meshes, which represent potential clones. The cost function is a measure of the difference between morphological properties of the

individuals and randomly sampled values from the distributions of the parent particle properties, see Equation 3.7. This function corresponds to a single particle, and thus is minimized for each clone. The mating process consists of swapping the spatial location of a randomly chosen subset of vertices on one mesh with the spatial location of a subset of points on another mesh. Finally, the mutation step consists of first randomly selecting individuals. Then, vertices on these individuals are randomly selected. These vertices are then perturbed by a vector. Each component of the vector is randomly sampled from a gaussian distribution with mean zero and variance user-specified.

$$\begin{aligned} C = (\frac{\mu_{K1} - \mu_{k1}}{\mu_{k1}})^2 + (\frac{\mu_{K2} - \mu_{k2}}{\mu_{k2}})^2 \\ +(\frac{\sigma_{K1} - \sigma_{k1}}{\sigma_{k1}})^2 + (\frac{\sigma_{K2} - \sigma_{k2}}{\sigma_{k2}})^2 + (\frac{S - s}{s})^2 \end{aligned} \tag{3.7}$$

In Equation 3.7, μ_{k1} and μ_{k2} are the average values of the minimum and maximum principal curvatures of a cloned particle. σ_{k1} and σ_{k2} are the standard deviations of the minimum and maximum principal curvatures of the cloned particle. The corresponding parameters for the target curvature distribution properties randomly sampled from the parent particle data are denoted with subscript capital K. S is the randomly sampled sphericity, while s is the sphericity of the cloned particle. Minimizing this function corresponds to minimizing the square of the difference between each morphological property of the clone and the corresponding randomly sampled morphological property from the parent particle distribution as a fraction of the current clone morphological property. We chose a least-squares approach because of its simplicity, but more detailed cost functions can be constructed if desired. This cost function can easily be modified for a variety of target morphological parameters and length scales.

Properties and parameters such as the standard deviation of the mutation vector distribution, number of individuals, number of iterations, or generations of the genetic algorithm can all be tuned to enhance clone generation. In addition, if the cost of a clone is over a threshold value after generation, then the particle is rejected as it will be too difficult to perturb the particle to reach these sampled values without compromising the physicality of the grain. For instance, if the difference between a current and target measure of the curvature distribution on a particle is too high the particle may be contorted in non-physical ways to match this distribution.

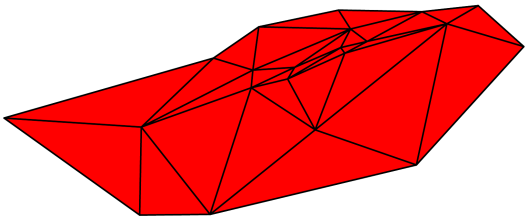

Figure 3.8: Optimized clone on largest length scale.

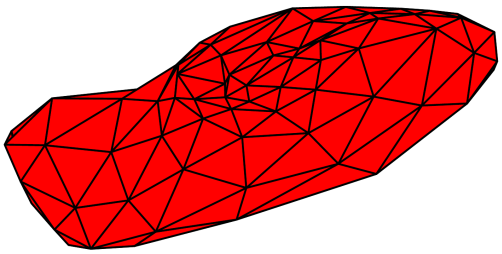

Figure 3.9: Optimized clone on both length scales.

These contortions include overlapping mesh elements, or extremely high curvature spikes around the grain surface. An arbitrary threshold value was added to the cost for every vertex with a curvature more than 2 standard deviations away from the mean curvature. The python package DEAP was utilized for minimizing the cost function (De Rainville et al., 2012). Figure 3.8 shows an optimized clone on the largest length scale. After the optimization process is complete for the coarse-meshed clone, the mesh is refined, and the process is repeated with parent distribution data measured at the corresponding length scale. Figure 3.9 shows a cloned particle that has been optimized on two different length scales.

3.2 Results and discussion

Analysis

A total of 1000 clone particles were generated from distribution data measured from an existing parent database of 1000 particles. The clones were generated following the procedure and minimization of the cost function outlined above. Figure 3.10 shows the average normalized cost function and standard error for 1000 particles for the first 100 generations of the genetic algorithm. The cost is normalized in that, the cost for a given particle is divided by the particle's cost at generation zero. Figure 3.10 shows minimization of the cost function, which results in achieving morphological properties close to the targeted values. The jumps in the cost at a few random points, while initially concerning, are a characteristic of the genetic

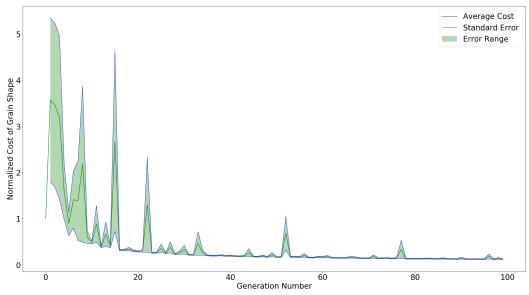

Figure 3.10: Average normalized cost function (the summation of the cost of each clone at a given generation divided by the number of clones sampled) and standard error (the standard deviation of the cost of the clones at a given generation, divided by the square root of the number of clones sampled) for 1000 clones sampled, for 100 generations of the genetic algorithm.

algorithm and the nature of the nonlinear optimization problem. Specifically, the spikes occur because a proposed particle was deformed to a high cost morphology. This high cost morphology was quickly rejected and optimization continued at a more reasonable cost level.

The method can produce a variety of morphological combinations. Figure 3.11 shows multiple cloned particles, sorted by sphericity and roundness. As roundness decreases, the cloned particles have higher surface perturbations. As sphericity increases, particles become less oblong and are closer in large scale morphology to a sphere.

The resulting distributions of roundness and sphericity for the clones match closely with the parent distributions, with each particle contributing one value to the histogram.

Figure 3.12 displays histograms of parent and clone particle sphericity, measured on the final clone particles. Figure 3.13 displays histograms of parent and clone particle roundness, measured on the final clone particles. Additional histograms of parent and clone particle properties can be found in Figures 3.14 and 3.15. It is important to note that the method was able to capture morphological property distributions at different length scales and for different types of distributions. For example the average maximum curvature on the larger length scale resembles a Gaussian distribution, while the standard deviation of the minimum curvature on the smaller length scale is similar to a binomial distribution. The capability to match arbitrary property distributions gives the method tremendous flexibility in cloning grains.

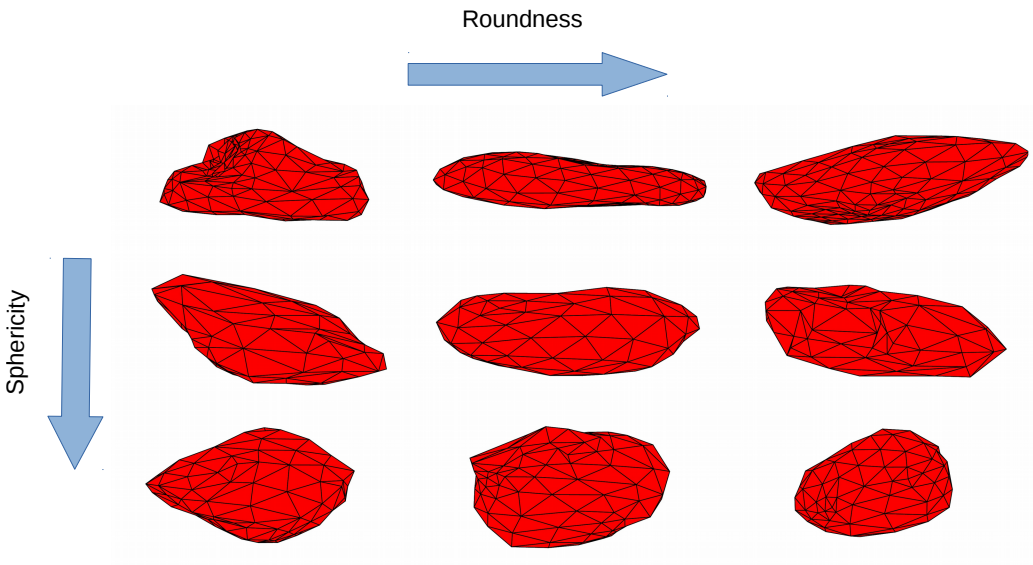

Figure 3.11: Multiple grains generated by the granular cloning algorithm, sorted by sphericity and average maximum normalized principal curvature.

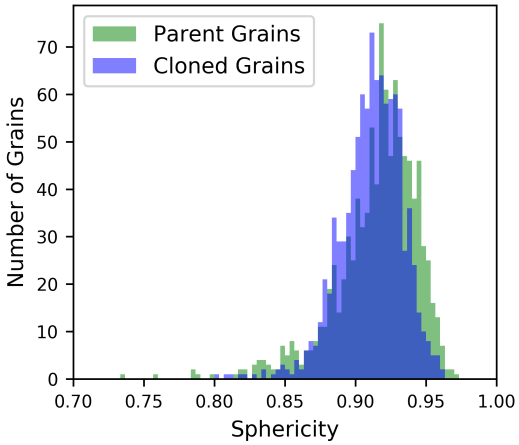

Figure 3.12: Sphericity of parent and cloned particles after optimization.

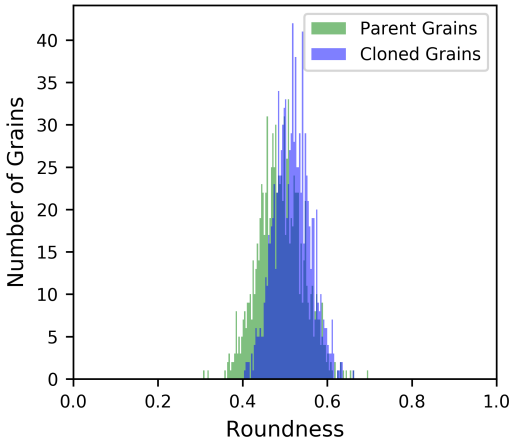

Figure 3.13: Roundness of parent and cloned particles after optimization.

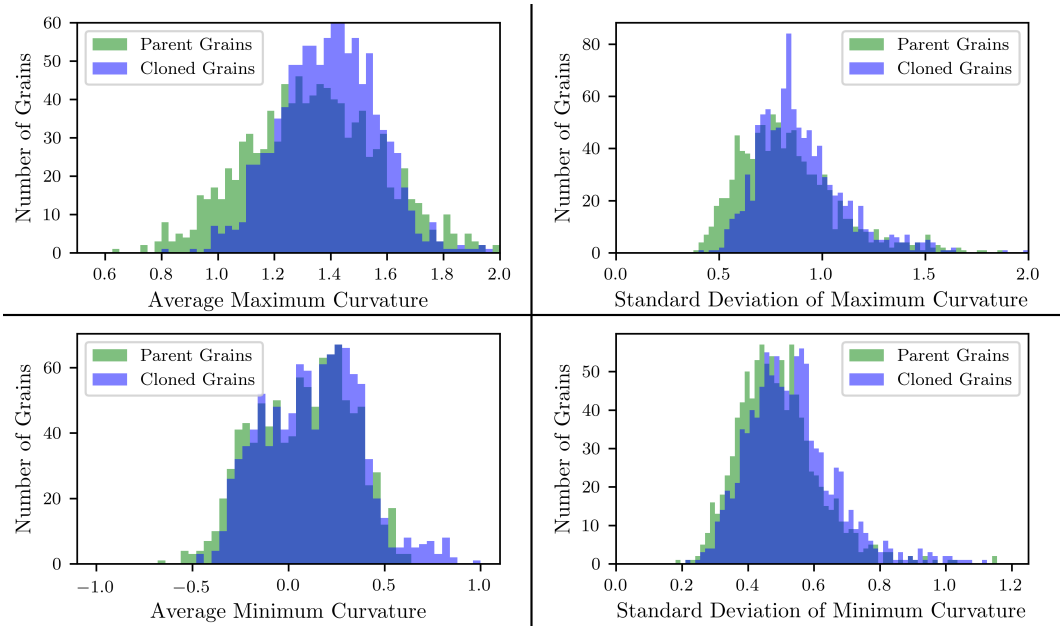

Figure 3.14: Distributions of principal curvature properties on larger length scale.

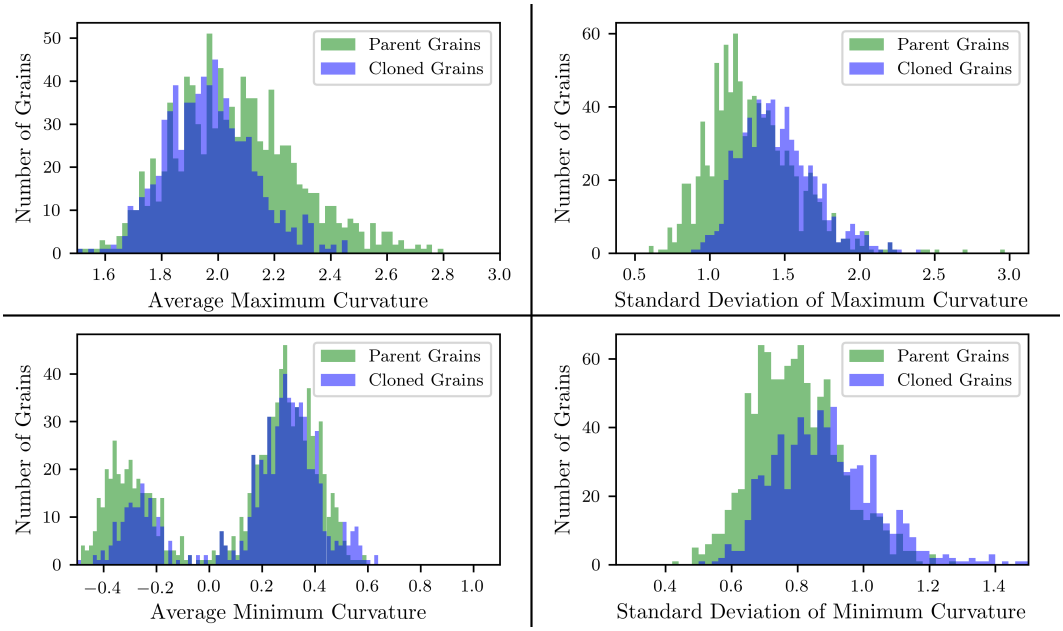

Figure 3.15: Distributions of principal curvature properties on smaller length scale.

3.3 Conclusions

In this work, a new method for generation of unique computational grains from granular material statistics has been described and successfully demonstrated. The method can build particles from any reasonable morphological property via modification of the cost function in the optimization step. We chose to target sphericity and curvature distribution properties — which in certain cases is roundness — as our chosen characteristics. A total of 1000 cloned particles were generated from an existing parent particle dataset. The distribution of morphological properties of these clones were compared to the distribution properties of the parent particles. It was shown that the clone particles accurately reflect the morphological properties of the parent particles.

The shape properties singled out for clone generation in this paper were chosen because they represent morphological properties that are commonly measured. We make no comment on whether these properties are the most important morphological properties of grains in a granular material. Further analysis on shape parameters is required to determine ideal properties to generate clones that match parent mechanical properties. However, the ability of the granular cloning method to build particles with any morphological property and variations of these properties allows the rapid generation of different particle datasets to investigate the underlying physics. As such, our method allows detailed numerical investigations of granular mechanics,

where the importance of specific grain shape properties on mechanical behaviors can be investigated.

There are several ways this method could be improved for future particle design. Firstly, as in Jerves Cobo (2016), there are many knobs that can be turned to change the optimization process. These include all the parameters of the genetic algorithm (as explained in Section 3.1), the threshold value for particle rejection, the amount of elements in a given length scale, in addition to all parameters used for meshing, subdivision, particle deformation and curvature measurements that are determined by the particular computer graphics software utilized. All of these parameters can be toggled to potentially achieve a faster or more accurate cloning process.

Different particle properties can also be inserted into the cost function. We believe that particle principal curvature mean and standard deviation and sphericity capture many important particle shape properties, while striking a satisfactory balance between clone generation accuracy and the amount of time necessary to generate a clone. However, other morphological properties such as aspect ratio, volume to surface ratio or higher order derivatives of the particle surface could be included into the cost function, potentially increasing the accuracy of the generated clones or the efficiency of the cloning process.

Future work will also compare mechanical properties captured in LS-DEM simulation (stress-strain curves, failure strength, friction angle, etc.) between assemblies of parent particles and clone particles. This will further validate the granular cloning process. Additionally, systematic investigations of different shape properties would help with understanding which morphologies are the most critical in relationship to mechanical properties of granular systems.

Chapter 4

UNEARTHING REAL-TIME 3D ANT TUNNELING MECHANICS

PUBLISHED CONTENT AND CONTRIBUTIONS

Buarque de Macedo, Robert et al. (2021). "Unearthing real-time 3D ant tunneling mechanics." In: *Proceedings of the National Academy of Sciences* 118, pp. 1–15. R.B. wrote the relevant code, analyzed the data and wrote the manuscript.

Excavation is a vital component of both the natural world and modern civilization. Mining alone constitutes an over 80 billion dollar industry nationally (*US Mine Production Increasing, Estimated Value of 86.3 Billion in Minerals* 2020), providing an abundance of materials upon which society relies. In nature, insects such as ants have evolved strategies for large-scale efficient and durable tunnel excavation. Indeed, colonies of subterranean-nesting ant species can create nest structures several meters in depth that can persist for decades (Tschinkel, 2003). This biological feat of engineering has fascinated both biologists and physicists alike (Frost et al., 2017; Cassill, Tschinkel, and Vinson, 2002a; Khuong et al., 2016), but is especially captivating from a mechanics perspective (Espinoza and Santamarina, 2010). As anyone who has played Jenga is aware (Hasbro, 1983), removing certain blocks is more likely to cause a collapse than removing others. What principals do ants follow such as to avoid removing structurally critical grains during excavation? Do factors other than safety determine digging technique i.e. time and energy efficiency? Do ants dig according to a simple, innate algorithm? By studying termite mounds, robots following termite-inspired algorithms have been implemented for autonomous construction (Werfel, Petersen, and Nagpal, 2014). Similarly, understanding the innate, collective behavior algorithm that ants employ to excavate tunnels could lead to more efficient and economical digging strategies for resource extraction. Mining collapses can cost up to a 100 million dollars individually (Sousa and Einstein, 2021), in addition to threatening the safety of the workers. Eventually, an autonomous mining robot following said methodology may allow humans to avoid dangerous excavations altogether (Hyder and Nah, 2018). Such a robot is ideal for interplanetary mining (Sivolella, 2019); adapting to extreme and changing conditions before a terrestrial human receives a signal.

There exists a rich body of literature investigating the mechanics and structure of ant tunnels. Classically, the 3-dimensional forms of subterranean colonies were elucidated by the pouring of coagulating fluids into an unoccupied (or euthanized) colony. These landmark studies revealed the ordered chaos of the ant underworld:

a byzantine collection of vertical or angled tunnels coalescing about horizontal chambers (Tschinkel, 2003; Cassill, Tschinkel, and Vinson, 2002b). By contrast, inferring how such structures were created by the ants has typically relied on the use of far simpler, often two dimensional experimental nests. For example, the effects of soil grain size distribution and saturation on tunneling diameter, stability and structure was studied by observing quasi-2D ant farms housing harvester ants *Pogonomyrmex barbatus* (Espinoza and Santamarina, 2010). For this species, it was shown that the most effective tunnel excavation was observed when grains were small enough such that workers could carry particles with their mandibles. Yet, cohesion had to be high enough to support tunnel structures, but not so much as to resist the ants' pulling force. In another 2D study, it was found that the area and digging rate of excavation depended on size of the fire ants involve. However, the topological structure of the tunnels, i.e. the ratio of edges to vertices in a graph representation of the tunnel, was independent across ant size scales (Gravish, Garcia, et al., 2012). However, to elucidate features of the ant digging algorithm that lead to robust tunnel formation, there is a critical need to both quantify how ants tunnel in three dimensions, and deduce how their actions impact the mechanical properties of the surrounding soil.

Nowadays, x-ray computed tomographic imaging (3D XRCT) offers a potential solution for non-destructive analysis of 3D colonies. Minter et al leveraged such technology to demonstrate how ants will change digging angle when encountering gradients in soil density (Minter, Franks, and Brown, 2011). Gravish et al tracked tunnel diameter via XRCT, illustrating how tunnel size is correlated with worker ant morphology, in particular body length (Gravish, Monaenkova, et al., 2013). Goldman et al (Monaenkova et al., 2015) utilized 3D XRCT images of ant tunnels at multiple instances in time to demonstrate how increasing water content at low to intermediate moisture levels correlates with the properties of tunnels dug by ants. By measuring the yield force required to drag a rod on a robotic arm through the soil, it is discovered that increases in yield force due to moisture content correlate with increasing tunnel depth. This work suggests soils with higher yield strengths lead to more robust and stable tunnels. Computer simulations have also emerged as a means for probing ant tunnel mechanics. Frost employed Discrete Element Method (DEM) simulations (Cundall and Strack, 1979b) — which model grains as rigid objects obeying Newtonian physics — to discover that soil arching around rectangular cavities increases the stability of surrounding openings, a possible explanation for inter-woven tunnel geometries (Frost et al., 2017). Behaviorally, ants follow

patterns when selecting grains for wall construction; exhibiting a preference for heterogeneous grain sizes. Such a mixture will have a higher angle of repose, and therefore stability, than homogeneous collections of grains (Aleksiev, Sendova-Franks, and Franks, 2007) . Furthermore, ants will prioritize ease of grain removal when digging over robustness of the resulting wall (Minter, Sendova-Franks, and Franks, 2013). Clearly, ant tunnel construction is strongly influenced by the granular makeup of the soil. Nevertheless, it remains unclear how exactly ants construct stable tunnels in natural settings.

Unsaturated soils, like most granular materials, exhibits "force chains": networks of particles carrying the majority of stress (Radjai et al., 1996; Gili and Alonso, 2002). As mentioned in (Frost et al., 2017), removing particles in these chains is likely to provoke instability, in addition to being harder to remove due to frictional resistance. Do ants avoid extracting grains from such chains? More-so, if the increase of interparticle forces leads to more robust tunnels, how do ants cope with the increasing energetic cost of grain removal (Monaenkova et al., 2015)? These questions are key towards the development of a bio-inspired tunneling algorithm that minimizes the probability of collapse.

In this study, we employ 3DXRCT to map the forces around real ant tunnels during naturalistic tunnel construction. We use this mapping to explore patterns relating tunnel construction to force distributions in real time, in addition to other critical granular material attributes. Because the shape, position and orientation of grains are crucial for determining force distributions in a soil (Chen, Liu, et al., 2020; Yin, Wang, and Zhang, 2020; Azéma and Radjai, 2012; Li, Marteau, and Andrade, 2019), we consider grain-scale properties of the excavated soil and their evolution in time. With XRCT, we achieve sub-mm resolution 3D imaging on a frustum-shaped container of ants and soil during tunnel excavation, during tunnel excavation. Leveraging this data, we re-create the experiments *in silico* via a DEM simulation which can model particles of arbitrary shapes — the Level Set Discrete Element Method (LS-DEM) (Kawamoto et al., 2016). From this simulation, we calcaulate the changing temporal dynamics of interparticle and grain-wall forces throughout the entire sample as ants execute their tunneling behavioral program. This combination of high resolution dynamic imaging of tunnel excavation complemented by grain-scale mechanics unveils the spatio-temporal mesoscopic impact of tunneling ants on the surrounding substrate, elucidating why ants are such efficacious tunnelers.

Methods

To probe the effect of granular physics on ant tunneling behavior, we leverage XRCT imaging at sub-millimeter resolution. 500 ml of quikrete soil with average grain diameter of 2.3 mm (see SI) was mixed with 20 ml of water, and poured into the frustum for a water content $\omega = 0.03$ and initial porosity 0.42. The frustum was encapsulated into a device specifically designed for our XRCT experiments (SI). The device was placed into a CT scanner, and a forty-minute high-resolution scan was performed of the entire sample. Fifteen (15) *Pogonomyrmex occidentalis* ants were released into the top of the container, and the container was sealed (MacMahon, Mull, and Crist, 2000). This number of ants were chosen before the experiment through an optimization procedure performed using the same species of ant and soil as the main experiment. Starting from 1 ant, increasing numbers of ants were observed digging through soil in a laboratory environment. It was found that optimal excavation rate was achieved starting at 15 ants. Following this, faster (four-minute) half-resolution scans were taken every 10 minutes over the course of about a day. Each scan captured the structure and orientation of almost all particles in the sample in 3D. Six (6) instances of the experiment were performed overall, though due to the machine occasionally pausing overnight (SI) only 3 studies collected continuous data on ant tunneling. While the morphology of all 3 experiments are studied, the first two experiments are primarily analyzed in this article, as they span the two possible cases of tunnels on the boundary and in the bulk.

From these three-dimensional images, a digital avatar was created for each particle in the sample. As explained in the supplemental information (SI), a particle avatar is a mathematical representation of a grain's shape, position and orientation; factors known to significantly influence force distribution (Nguyen et al., 2015). Furthermore, by comparing images taken at different instances in time, the order of grain removal by the ants could be determined — up to the frequency of the scans. From here, the morphological properties of removed grains and kept grains were compared, and an LS-DEM simulation utilizing these avatars was executed. All four steps of the digital reconstruction are illustrated in Figure 4.1.

Results and Discussion

Tunnel and particle morphology

Tunnel and grain shape properties were analyzed before considering force chains, to probe the mechanics at the tunnel scale. Splines were fit to tunnels for obtaining a smooth representation of the tunnel axes. In Figure 4.2, a depiction of the spline —

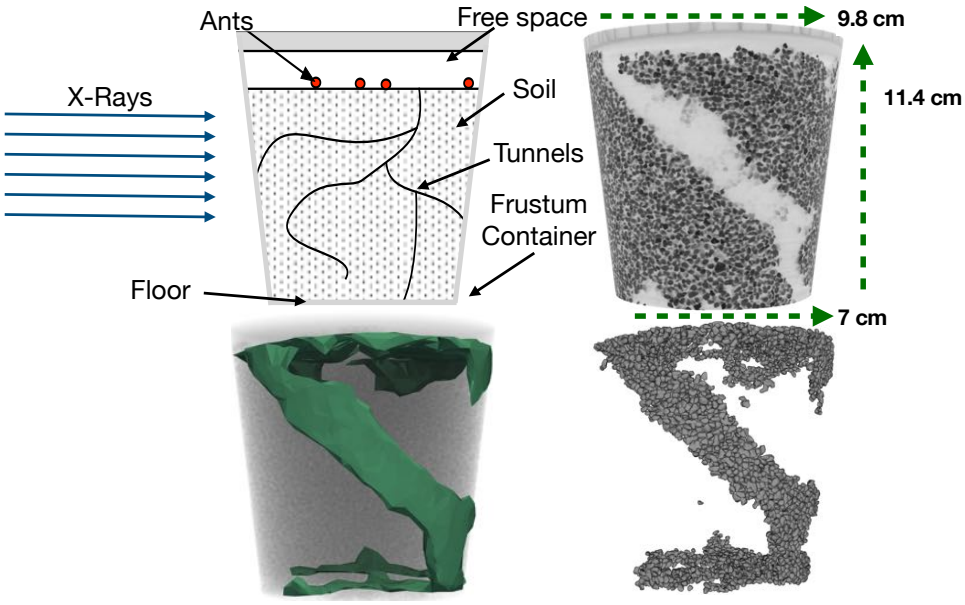

Figure 4.1: The 4 stages of LS-DEM recreation. Top left: Experimental design. Top right: One viewpoint of a completed tunnel from x-ray imaging. Bottom left: Alpha-shape fit to the locations of removed particle centroids for viewing the 3D tunnel, with $\alpha = 40$ (Lou, Jiang, and Scott, 2013). Bottom right: Digital recreation of particles removed by ants in initial location.

with tunnel axis direction obtained from the spline gradient — is presented for the 3 successful experiments on top. On the bottom are multiple measures for quantifying the tunnel's structure.

Ants tend to dig on the container's boundary: in all cases, the initial tunnel began from the container's boundary. Out of all 5 tunnels pictured, only one tunnel (green) passes through the interior during descent. This predilection for the boundary could be simply a matter of geometry: ants start digging down once horizontal motion is inhibited (e.g., by the container's boundary). Or, it could be due to the difference in cohesion between the container's boundary and the particles compared to particle-particle interactions. The latter explains why ants tend to stick to the boundary during excavation.

The ants tend to dig in linear segments. Specifically, along piece-wise segments the ants maintain an approximately constant digging angle ϕ (defined as the angle of the tunnel axis with respect to a horizontal plane). This can be seen in all five of the tunnels. However, the purple and blue tunnel do show gradual variation in angle in parts. Almost vertical descents occur at the top. In the bulk, ants dig at or below the angle of repose for the material ($\approx$ 40 degrees, see SI). Yet, as pointed

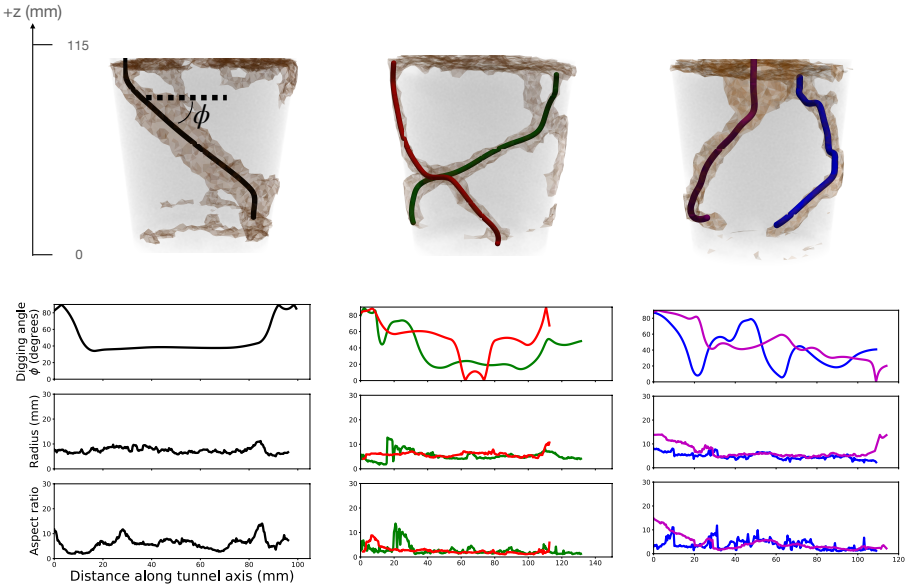

Figure 4.2: Spline fits to ant tunnels. Top) Interpolating spline fit to an ant tunnel, with scale for height. Bottom) Digging angle to horizontal plane ϕ, tunnel radius and aspect ratio as a function of distance along tunnel axis obtained from splines. For high resolution images of the 3 experiments with splines, see S.I (Figs S4 — S8).

out above, the ants exploit the presence of boundaries where they can reach higher digging angles ϕ, such as in experiment 3 (purple/blue). This quantitative measure of digging angles in a cohesive material is consistent with qualitative observations in (Espinoza and Santamarina, 2010).

The aspect ratio of the tunnel at a given distance along the spline is calculated by finding the centroids of all removed particles (pre-removal) which intersect a plane with normal pointed in the direction of the spline, at the particular distance along the spline. Principal component analysis was performed on the centroids projected into this plane, and the ratio of the largest to smallest eigenvalue was taken as the tunnel aspect ratio. Once a tunnel is born from the top excavation, tunnel diameter and aspect ratio is mostly constant, with the green and red tunnels having the lowest aspect ratio and diameter ($\approx$ 4 times particle diameter, consistent with (Gravish, Monaenkova, et al., 2013)). For tunnels dug against a boundary, tunnel morphology is elliptical, raising the cross section aspect ratio. This shape could be the result of ants excavating a segment of a circular tunnel.

The high resolution scan's voxel edge length (70 μm) is about $\frac{1}{40}$ of average particle diameter. This level of detail for each grain means that the ants' preferences for

removing particles with certain attributes can be explored. The volume of the grains has been quantified by counting the number of voxels in each particle via the spam python library. The distributions of volume between removed and nonremoved particles are compared for statistical significance using a Kolmogorov-Smirnov test, see (figure S2). There appears to be a slight, yet statistically significant, bias for lower volume grains. This result is consistent with experiments in (Espinoza and Santamarina, 2010), in which ants prefer to remove particles with diameter comparable to mandible size (1 - 2 mm).

Mechanics of Tunnel Surface

The forces localized on the tunnel surface are studied in this section, offering insight into ant tunneling behavior. Multiple forces exist between adjacent grains in an unsaturated granular material. At the scale of our particles ($\approx 10^{-3}m$) the dominating forces are cohesion, friction, weight and contact between grains and with walls (Espinoza and Santamarina, 2010; Richefeu, El Youssoufi, and Radjai, 2006). To calculate these forces we leverage LS-DEM, detailed in (SI). In summary, we begin with a digital twin of the experiment. This means each particle in the original physical frustum maps to a computational particle — as illustrated by the bottom right image in Figure 4.1. The digital particles match the physical grains up to the resolution of the scans — 0.07 mm. This resolution is sufficient to capture the shape, orientation and position of the particles, see Figure S1 in the supplementary material. The precise reproduction of each interparticle contact in LS-DEM may not match reality exactly. Indeed, even if we matched the contacts precisely, we could not guarantee an exact reconstruction of the forces due to the indeterminate nature of force chains (Shaebani, Unger, and Kertész, 2009). Further, we could not image the location and shapes of all the liquid bridges. Nonetheless, we are more interested in capturing the general behavior of forces in our sample - such as the dependence of force chain morphology on the growth of the tunnel. This emergent behavior is more dependent on the distribution of particle shapes and boundary conditions than on the specific contact locations (Chen, Liu, et al., 2020; Fang, Guo, and Hou, 2020). In this regard, LS-DEM has shown high efficacy (Kawamoto et al., 2018).

The DEM simulation of these grains is left to equilibrate under the aforementioned forces. Cohesion is handled in our simulation using the bond model developed in (Potyondy and Cundall, 2004). Details on this model are given in the supplementary information, see (S.I.). Grains are then deleted in the order in which ants removed the particles. Since scans were performed every 10 minutes, many grains (≈ 100) are

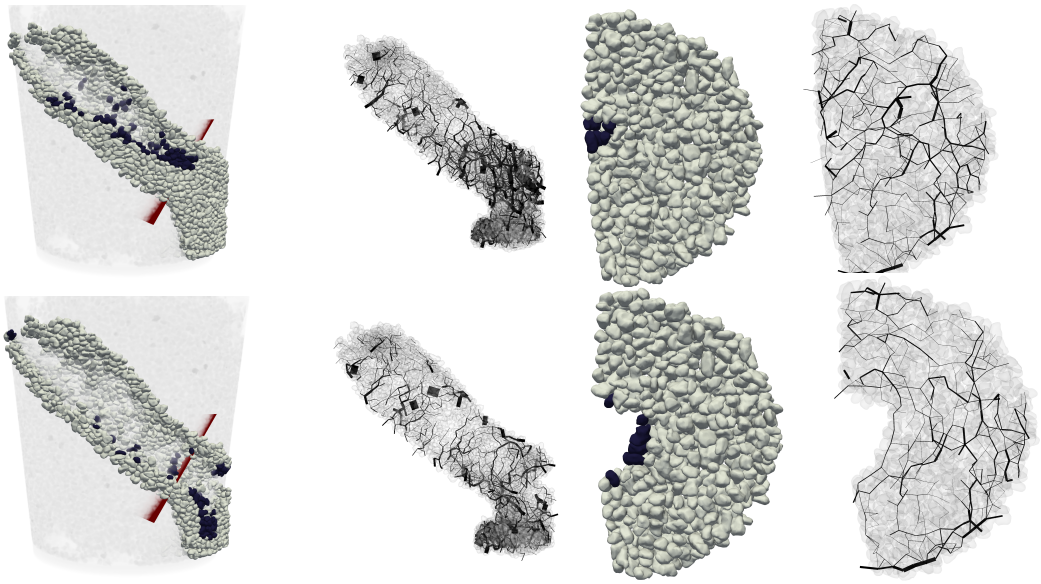

Figure 4.3: Visualization of forces on grains in and around tunnel for experiment 1. Particles which will be removed in subsequent frame are colored blue. Top row: Simulation after equilibration at specific frame. Bottom row: Simulation after equilibration at a later frame. Column 1) Rendering of tunnel particles. Column 2) Forces on tunnel particles. Column 3) Rendering of particles across red plane in column 1. Column 4) Forces through particles in Column 3.

removed during each scan. After every round of particle removal, an equilibration is performed. This methodology is similar to that of dissolution studies (Cha and Santamarina, 2019). We number each equilibration chronologically, denoting this number as the experiment's 'frame.'

The structure of forces for experiments 1 and 2 were analyzed. Figure 4.3 depicts particles and simulated forces from experiment 1. The top row displays the system of particles at a particular frame, while the bottom row corresponds to a temporally later frame (70 minutes later). In the first column, the x-ray image is displayed, with particles on the tunnel's surface rendered individually. Particles which will be removed in the immediate next frame are shaded dark. Column 2 illustrates the forces between particles on the tunnel surface for the two frames. Each black line is a branch vector — i.e. a vector which connects the center of masses between two interacting particles. The thickness of the line is proportional to the magnitude of the normal force between the participating grains. Branches of contiguous particles woven together by high interparticle forces are identified as force chains, as defined in the introduction. Column 3 is a projection of particles onto the red plane in column

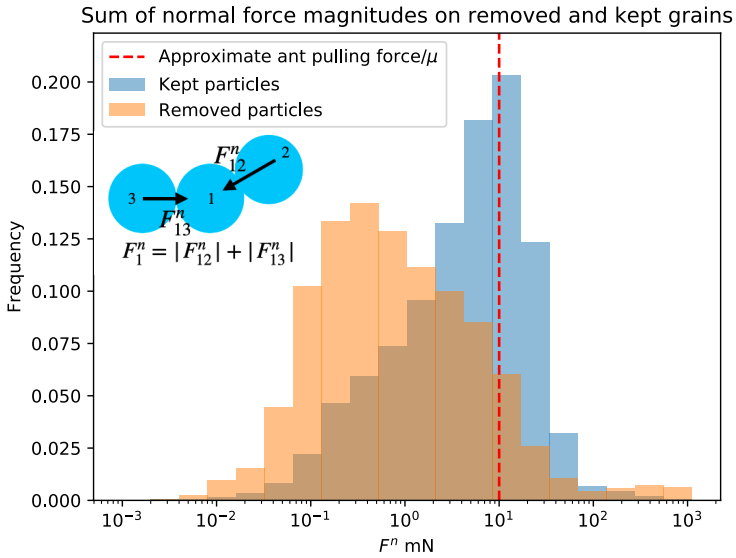

Figure 4.4: Distributions of sum of normal force magnitudes F^n for kept and removed particles across experiments 1 and 2, totalling 117000 grains — see text for F^n definition. The blue histogram is the distribution of F^n_i among all grains which are never removed, at the frame before tunneling begins. The orange histogram is the distribution of the same parameter among particles at the frame immediately before said particle's removal. The approximate ant pulling force is plotted in red (Espinoza and Santamarina, 2010). Removed particles with F^n_i greater than the ant pulling force may be a consequence of model errors in predicting which particles are in force chains. The difference between the two distributions is statistically significant, with $p << 0.005$ under Kolmogorov–Smirnov test. The dark area represents the overlap between the two histograms.

1. The set of particles projected are distances of approximately three tunnel radii from the tunnel axis and two particle diameters from the plane. Such visualization reduces the dimension of the data, revealing patterns influenced by the tunnel axis. The final column presents the distribution of forces in this cross section. In addition, a video of what an ant would see while traversing the green tunnel was compiled, see movie S3.

We make a couple inferences from this data. Firstly, grain forces on the surface of the tunnel tend to be significantly less than that of grains positioned deeper into the bulk. In addition, surface forces are inclined to wrap-around the axis of the tunnel rather than travel along it. This arching phenomena will be explored in section C.

In movie S2 the entire tunnel surface with its forces are rendered for 27 frames. The arching and force relaxation behaviors described above are even more apparent

Figure 4.5: Change in forces around tunnel due to ant excavation for green tunnel in experiment 2, within the bulk. Left: intergranular forces in a tunnel cross section before excavation. Middle: forces in same cross section after tunnel excavation. Right: distribution of F_n in particles which make the tunnel surface, before and after excavation. The presence of the tunnel has reduced the stress in tunnel particles due to arching, with $p << 0.005$ under Kolmogorov–Smirnov test.

in the video. Next, we study these phenomena quantitatively by looking at the distribution of normal forces in the sample. As the tunnel head reaches a cross-section, contact forces decrease on the particles in said section. The force between grains during slippage can be modeled by Coulomb friction (Cundall and Strack, 1979b). Therefore, the difficulty of removing a grain i is given by $\mu F_i^n + C$, where μ is the coefficient of friction between grains, C is the liquid bond strength that must be broken to remove a grain, and $F_i^n = \sum_j |F_{ij}^n|$ is the sum of the magnitude of normal forces on the grain, where F_{ij}^n is the j^{th} contact force acting on particle i, see drawing in Figure 4.4. With lower normal forces, less pulling force is required to overcome friction between each particle and its neighbors. Furthermore, low force grains are less structurally critical and can be supported through cohesive bonds. As ants remove particles at the tunnel head, the region of low force expands - granting the ants a larger set of loose grains to safely remove. As the tunnel head diameter is widened, the ants propagate the tunnel axis ever forward. Cohesive bonds and contact forces support force chain arches which occur across the tunnel surface. These arches re-form or strengthen as the tunnel is widened via ants “pruning” grains from the tunnel side walls. Tunnel widening dwindles at a given depth when

a particular tunnel diameter is reached. In precis, we see that ants avoid removing high force grains due in part to this high force relaxation.

It is worth mentioning that the frustum shaped container may provide additional stabilization due to the side walls. For instance, we see the largest tunnel — experiment 1 — occurring along the sides. Nevertheless, arching behavior still occurs within the bulk, as evident from results for experiment 2 (Figure 4.5) and detailed in section C.

Soil Arching

The effects described in the previous section are consequences of soil arching, which is considered in this section. As can be seen in Figure 4.3 and Movie S1, force chains tend to wrap around the tunnel axis. It has been shown that the presence of a tunnel in soil will cause this "arching" effect not only on the tunnel's surface, but in a larger zone centered around the tunnel axis (Chen, Tang, et al., 2011). This effect could help explain why particles on the tunnel surface tend to transmit relatively lower interparticle forces.

Arching is defined by Terzaghi as when "one part of a mass of soil yields while the remainder stays in place" causing a "shearing resistance within the zone of contact between the yielding and the stationary masses" (Terzaghi, 1943b). Visually, arching often appears as force chains with an arch-like shape, emanating from a discontinuity like a void. Crucially, arching displaces load from the discontinuity to the surrounding area.

While a multitude of studies have analyzed stress fields around linear tunnels with tunnel axes perpendicular to gravity (Wu et al., 2020; Lee et al., 2006; Yin, Wang, and Zhang, 2020), there is a paucity of research on tunnels with variable axis directions and complex particle shapes - though recently linear angled tunnels have been considered in continuum models (Vitali, Celestino, and Bobet, 2018). Consequently, the nature of arching in our experiment was investigated.

It was hypothesized that arches would wrap about the tunnel axis; changing orientation with tunnel direction. To test this hypothesis, particles on planes intersecting and with normal in the direction of the tunnel axis were visualized. An example of a tunnel cross section for experiment 2 is given in Figure 4.5, where both the particles and the intergranular forces are visualized. Experiment 2 is the only instance when ants tunneled away from the container boundary, and is more reminiscent of conditions found in nature. From inspection, forces at and near the tunnel surface have

significantly decreased following excavation, in particular directly above the tunnel. Forces above the tunnel also tend to arch about the tunnel axis - displacing the large load from the soil weight away from the hole. Such arches act as a "stress shield," maintaining the low contact forces within their interior. This effect was recently studied by Fang et al. (Fang, Guo, and Hou, 2020). Within the low stress zone, cohesive forces comparable to the weight of one grain are strong enough to support unloaded grains, allowing stable tunnels underneath pounds of earth. Therefore, arching occurs multiple layers deep into the material, shielding the vulnerable grains on the tunnel surface from forces which could trigger a collapse.

The histogram in Figure 4.5 quantifies the effect of stress shielding. The blue histogram depicts F^n for grains that constitute the tunnel surface post-excavation (SI), at the frame before excavation begins. The orange plot corresponds to the distribution of F^n on the same grains, after excavation. Clearly, excavation has reduced the load on the grains from the soil mass. To summarize, arches occurring within the soil form and strengthen during excavation. These arches reduce the load on particles at the tunnel surface. Thus, ants do not need to 'know' which grains are in force chains before particle removal; by selecting any particle on the surface of the tunnel, ants have a high probability of avoiding a structurally critical grain.

Closure

We have provided evidence that a subterranean-nesting ant species tends to dig in piece-wise linear tunnel segments. In addition, we demonstrated that the ants have a preference for removing smaller grains. Finally, we have demonstrated how ants can safely remove particles in a soil, even when digging below the soil surface by benefiting from force re-distributions via granular arching. We propose granular arching provides an effective tunnel lining, while also reducing load at the head of tunnel.

These results suggest that ants can maintain stable tunnels without needing to determine which exact particles are in force chains. Such findings are not at odds with how humans excavate, for instance when utilizing a tunnel boring machine. Nonetheless, ants achieve stability by gradually removing particles without the need for additional reinforcements — like tunnel linings and rock bolts. These results are applicable to a new class of palm-sized robots which tunnel into soils (Borela et al., 2021; Sadeghi, Mondini, and Mazzolai, 2017). Heuristics learned from our simulations could aid these robots with finding minimum energy paths through soils.

Even more, the principles discovered here may have applicability towards hard rock mining, where tunnels consist of a handful of jointed rocks and are well suited to DEM analysis (Boon, Houlsby, and Utili, 2015). It is the authors' intent to zoom out from the micromechanical world, and to leverage this framework in the creation of automated excavation algorithms.

4.1 Supplementary Information

Constructing Experimental Apparatus

The testing apparatus was first designed and built at Caltech. This device consisted of a small plastic container which could be filled with sand and ants, and placed within an XRCT scanner. The container needed to be large enough such that the ants could comfortably tunnel within the domain, yet small enough to obtain detailed x-ray images of all the individual grains. Furthermore, the casing needed to be cylindrical shaped so that it situated within the scanner. A plastic frustum was chosen as the experimental container, which was 11.4 cm in height, 7 cm in minimum diameter and 9.8 cm in maximum diameter. A plastic top for the container was 3D printed, with a hole in the center for depositing the ants.

Soil and Ants

Quikrete soil of size 10/12 (*Mesh (scale)* 2020) was utilized for this experiment by passing store bought sand through a mesh size 10 (2 mm) followed by a mesh size 12 (1.7 mm) sieve, and keeping the grains which passed through only the former sieve. Later analysis revealed the sieved granular material's average radius (maximum distance from centroid to surface) was 2.34 mm. Pogonomyrmex harvester ants were utilized for this experiment. Pogonomyrex ants were chosen because of their prolific digging and ability to handle grains on the mm scale, such as those used in the experiment that are ideal for XRCT imaging. Ants were ordered from antsalive.com.

Experimental Procedure

The goal of the experiments was to obtain the orientations and shape of each particle in the device as ants were digging. To achieve image resolution on the order of 0.1 mm, x-ray tomography was performed.

The soil sample was prepared by mixing 500 ml of 10-12 quikrete soil with 20 ml of water. This mix was poured into the plastic frustum. Multiple samples were created for the experiment. The number of grains amounted to around 60,000 grains each time. The sample was then placed into the x-ray tomographic scanner. An initial

high resolution scan with voxel edge length 70μm was performed. Then, 15 ants were released at the top of the sample, and the plastic top was secured on. Following this, a half-resolution scan with voxel edge length 140μm (last 4 minutes) was taken every ten minutes over the course of 20 hours, thereby tracking the dynamic states of the sample. The lower resolution scans can discern particle details on the scale of $\frac{1}{20}$ of the average particle diameter: enough information such that one can track the movement of all the particles imaged in the initial high resolution scan. Six experiments were performed overall, however due to the XRCT machine shutting off unintentionally over night, certain experiments were missing data points. Note this did not affect the quality of experiments which were measured.

The results of these scans were 3D tiff files, each corresponding to a particular experiment and time. These tiff files were then processed in the subsequent steps to obtain interparticle forces. From these images, the porosity ϕ could be determined via spam (Stamati et al., 2020).

Image Processing

To obtain forces between grains, we created digital particle avatars which mimicked the morphology of particles in the sample. Each avatar is a 3d discrete level-set of the grain surface, along with a collection of coordinates on the particle surface. For a given particle, its level set representation is a scalar function defined over three dimensional space, where its value at a point is the signed distance from said point to the particle's surface, see Figure 4.6. Before processing, x-ray tiff images were adjusted for consistent orientation and lighting across time, and a watershed algorithm isolated the voxels corresponding to each grain in the high resolution scan. This analysis was performed via the Python library spam (Stamati et al., 2020).

The process of converting a tiff file into level set particles is detailed fully in (Vlahinić et al., 2014). In summary, non-local means filtering is applied for denoising the watershed. Then, the level set of each individual grain is calculated through the process of re-initialization, as are its set of surface coordinates. Particle positions and rotations are also recorded.

To determine the frame at which grains disappear, the lower resolution XRCT images at different instances in time, or frames, were autonomously compared. For a low-resolution scan taken at a particular frame, if the mean gray value of the voxels that were occupied by a particle in the initial high resolution scan dropped below 128, the grain was labeled as removed and the step at which the particle disappeared was

recorded.

Tunnel Morphology Analysis

To generate Figure 2 in the text, a spline was fit to the initial positions of all particles that were removed for each of the experiments. To do so, k-means clustering was first utilized to isolate the centroids of the removed particles at each frame. The distances between centroids were computed to discern tunnels from one another. Then, a spline was fit to each set of centroids corresponding to a particular tunnel. The spline knots could be manually perturbed for a finer fit. Then, the spline was discretized into 300 points for further analysis.

Digging angle ϕ at a given point along the spline was determined by calculating the spline's derivative, then finding 90 — the angle between this direction and the z axis. This measure was chosen because it was similar to the angle of repose for a sandpile (Al-Hashemi and Al-Amoudi, 2018). For further analysis, the shape of the tunnel cross section at each spline point was calculated as follows: a plane was fit at the spline point with its normal vector pointed in the direction of the spline derivative. The initial centroids of each removed particle about one grain diameter away from the plane were projected onto the plane to form a 2 dimensional 'slice.' Next, a convex hull was calculated from the projection of the removed particle centroids in the 2d plane. The center of the convex hull was determined, and the average distance from the edge of the hull to the center was taken to be the tunnel radius at this spline point. To detect which particles were on the tunnel surface at a particular frame, all grains within approximately one grain diameter (2.8 mm) were classified as tunnel surface particles. Finally, principal component analysis was performed on the projected centroids in the plane, and the ratio of the largest to smallest eigenvalue was taken as the tunnel aspect ratio. All processing in this step was carried out by the SciPy Python library.

LS-DEM Simulation

Once the level sets and surface points of all the particles in the sample were obtained, the avatars could be used in simulation. As stated in the primary text, an extension of the DEM was used - the level set discrete element method (LS-DEM). In DEM, particles move according to classical rigid body mechanics. In the variant of interest here, particles may overlap each other. For each point on one particle which is overlapping another, a contact force is calculated. The normal force imparted from one particle onto another is a multiple of overlap distance, with constant

of proportionality k_n. Shear force, perpendicular to normal force, is determined according to a Mohr-Coulomb failure criterion with coefficient of friction μ and stiffness k_s. While calculating the overlap distance is trivial for spheres, it can be difficult and computationally taxing for particles of arbitrary shape. By representing the particles as level set avatars as in LS-DEM, overlap calculations for oddly shaped particles were tractable and accurate. Wall interactions were handled through an analytical expression relating position to wall overlap. See (Kawamoto et al., 2016) for details on LS-DEM.

Some particles, typically at the top and bottom of the container, were not imaged properly and their level set was non-physical. Thus, these avatars were removed before simulation. Other particles began with too high an overlap between each other, leading to high initial velocities in the simulation. This occurs usually due to errors in the image processing step. Such particles had their volume reduced by uniform contraction.

We use the calibration parameters similar to those in Kawamoto (Kawamoto et al., 2018), which have been shown to predict the location and behavior of shear bands within digital twins of triaxial test. We take particle density to be 2650 kg/m^3. k_n is the same as that in Kawamoto at $(3 * 10^4)$, with a slightly reduced $k_s = 0.8k_n$. As demonstrated in (Kawamoto et al., 2016), the specific value of k_n does not have a significant effect on results. We take $\mu = 0.45$, which is similar to but slightly lower than Kawamoto, which consisted of rougher grains. Furthermore, Kawamoto demonstrates that in the low-strain regime, such as in our sample, the response of the system to perturbation is not very sensitive to the coefficient of friction. Global damping is set to 100 s^{-1}, as it was found that this value led to efficient convergence to equilibrium, yet was large enough such that collapses and large displacements could still occur. The coefficient of restitution for local damping between grains is set to 0.4, to dampen spurious oscillations. Correctness was checked by following procedures in (Tu and Andrade, 2008).

To include cohesion in the model, particle bonding was implemented according to (Potyondy and Cundall, 2004). This model is equivalent to placing a beam between each pair of particles within a specified distance, which ruptures when the normal stress in the beam reaches a threshold $\sigma_c = \frac{-|F^n|}{A} + \frac{|M^s|R}{I} = \frac{C_n}{A}$ or the shear stress $\tau_c = \frac{|F^s|}{A} + \frac{|M^n|R}{J} = \frac{C_s}{A}$, where A is bond area, C_n is the maximum bond force in the normal direction and C_s is for shear, F^n and F^s are the normal and shear forces in the beam respectively, and M^n and M^s are the normal and shear moments

respectively. We take the bond area $A = 1mm$ ((Richefeu, El Youssoufi, Peyroux, et al., 2008)), and I and J are the area and polar moments of inertia of the beam. The normal direction of a bond between two particles is given by the direction of the vector connecting the two closest points on the aforementioned grains. While typical liquid bond models in DEM do not provide shear or moment resistance, such models have been developed primarily for spheres (Potyondy and Cundall, 2004). We find that adding shear and moment resistance is necessary for maintaining tunnel stability in all experiments. This is most likely due to the irregular shape of particles, and the more complicated geometry of cohesive bonds between grains. To validate our model, we perform angle of repose simulations along with experiments (see below). We also reproduce the DEM simulations from Santamarina et al, in which DEM particles are dropped through holes of increasing size in the flat bottom of computational silos - see Figure 6 in (Espinoza and Santamarina, 2010). We successfully predict the regions of stability/instability in accordance with the experimental results in said paper.

This model was chosen as to minimize plastic contact breakage during simulation, such that the closest approximation of the force distribution in the imaged sample was obtained. The original bonding model was developed for spherical grains. Thus, we extended this formalism by calculating bond displacement from the two closest points between the participating grains at bond creation. The force needed to break bonds was calculated from Equation (1) in (Espinoza and Santamarina, 2010):

$$C = \frac{\pi}{2}\sigma d[2 - (\frac{8}{9}\omega G_S)^{\frac{1}{4}}] \tag{4.1}$$

with air-water surface surface tension $\sigma = 0.073N/m$, water content $\omega = 0.03$, specific gravity $G_S = 2.65$ and particle diameter $d = 2.3$ mm resulting in cohesive strength C = 0.37 mN. Note this formula applies to spherical particles. We initially assumed it was a sufficient approximation for non-spherical particles due to the local smoothness of grains at contacting points. Nonetheless, it was discovered that $C_n \geq 2 * C$ for tunnels to be stable in our simulations. This may be due to the assumption of sphericity in the bond strength formula. During simulation, every 10 timesteps a particle bond is created between any unbonded pair of grains which are within 0.28 mm of each other. The normal force needed to break bonds was set to $C_n = 2C$, and shear $C_s = 0.8C_n$. Normal bond stiffness was $k_n = 2C$, and $k_s = 0.8k_n$.

For the first frame of the simulation, an equilibration step was conducted where par-

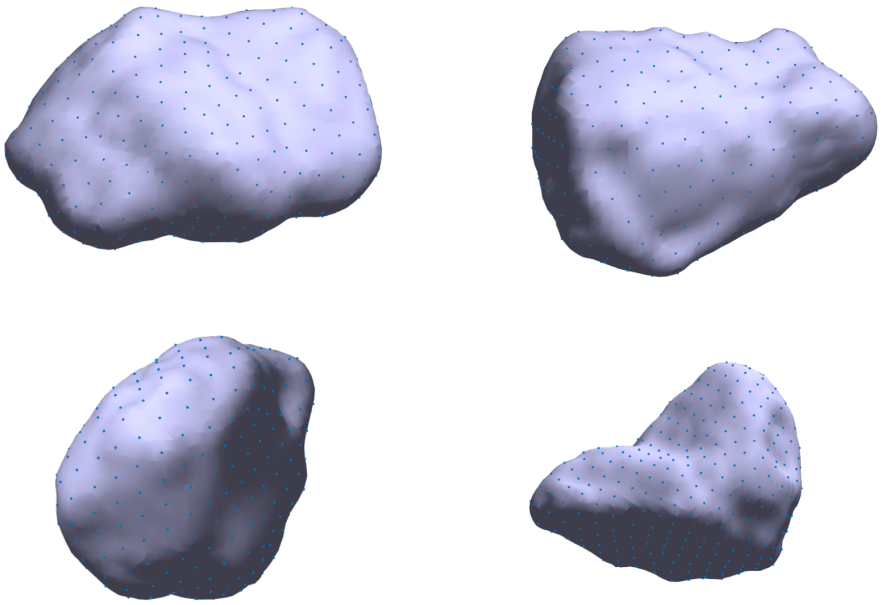

Figure 4.6: Example of 4 particles used in LS-DEM simulation, obtained from XRCT. 0 isosurface of levelset given by purple mesh, with surface points superimposed.

ticles settled from their starting configuration to a resting configuration. The simulation was run until the kinetic energy converged to a value less than $5kg\ vox^2/s^2$. We also checked that the total force on each grain was sufficiently small, such that the simulation total energy was at a stationary point.

The following was then performed for each frame: first, the final configuration of the previous frame was used as the initial configuration for the current. Then, the particles removed between the current and previous image were deleted from the simulation. The new configuration was run to equilibrium, and the process was then repeated for all imaged frames.

Angle of Repose

There is no agreed upon definition of the angle of repose (AOR) for a granular material, nor is there a standardized method for determining the angle — particularly for cohesive grains. For practical purposes, we define it as 'the steepest slope of the unconfined material, measured from the horizontal plane on which the material can be heaped without collapsing' (Al-Hashemi and Al-Amoudi, 2018).

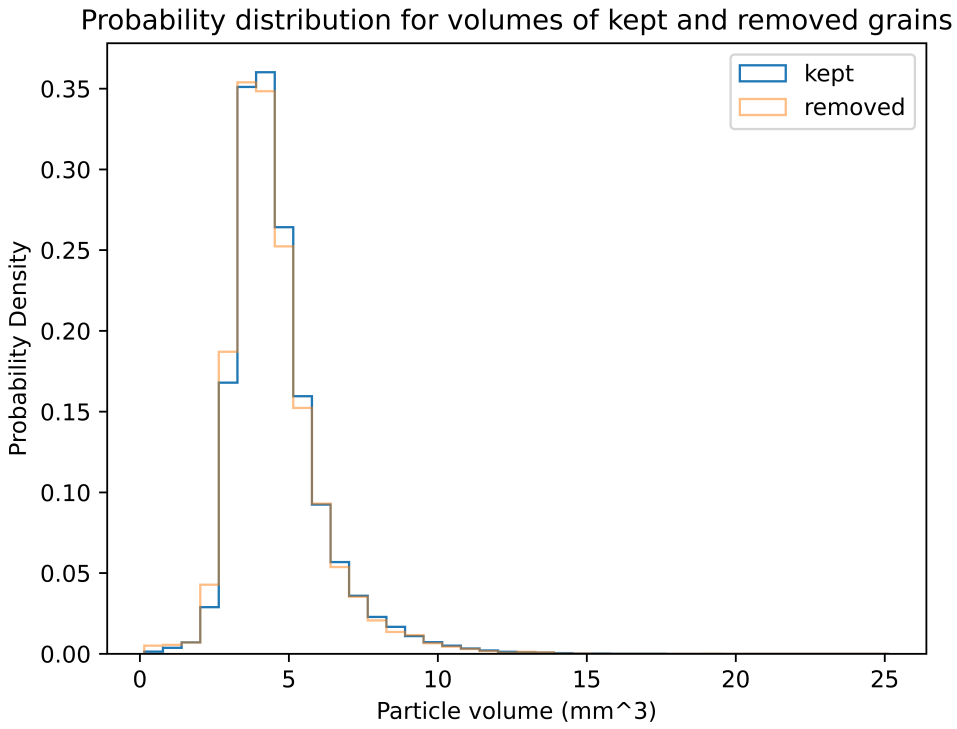

Figure 4.7: Distribution of particle volumes of grains removed by ants (Removed grains) and grains kept by ants (Kept grains) across all 3 experiments. The difference between the two distributions is statistically significant, with $p << 0.005$ under Kolmogorov-Smirnov test.

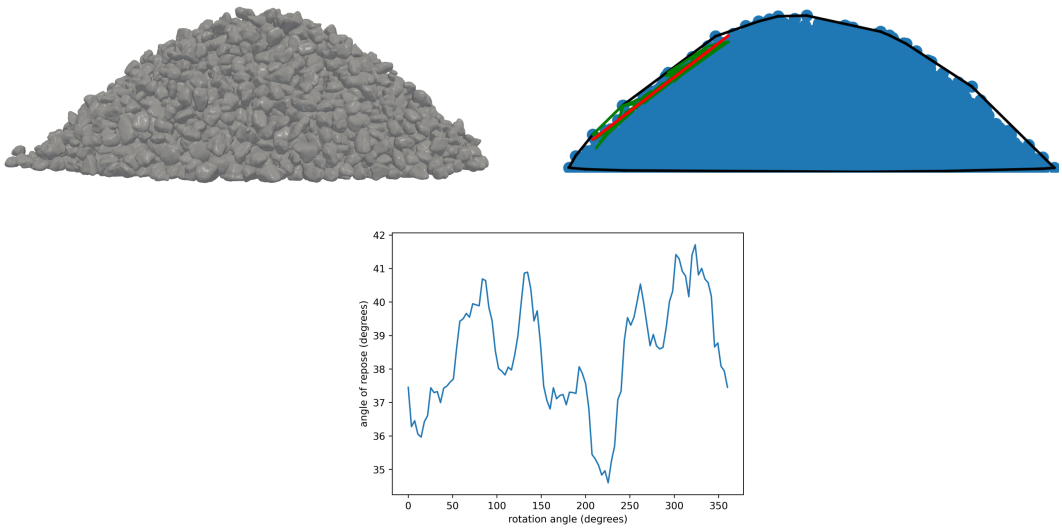

Figure 4.8: LS-DEM pluviation simulation to find AOR. Particles were dropped through a filter into a conical pile (top left). Particle centroids were used to construct a 2D cross section (top right), which is centered at the origin and rotated through a circle (see movie S4). A convex hull is fit to the projection of centroids in each plane (black lines). In a given cross section, centroids used for estimating AOR were highlighted in green, with the red line denoting least squares fit. Bottom: rotation angle of projection plane vs. AOR of cross section.

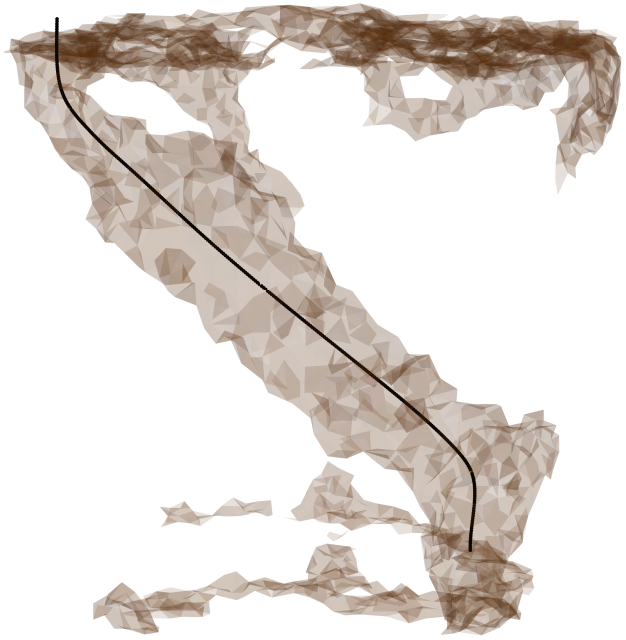

Figure 4.9: Experiment 1 tunnel 1.

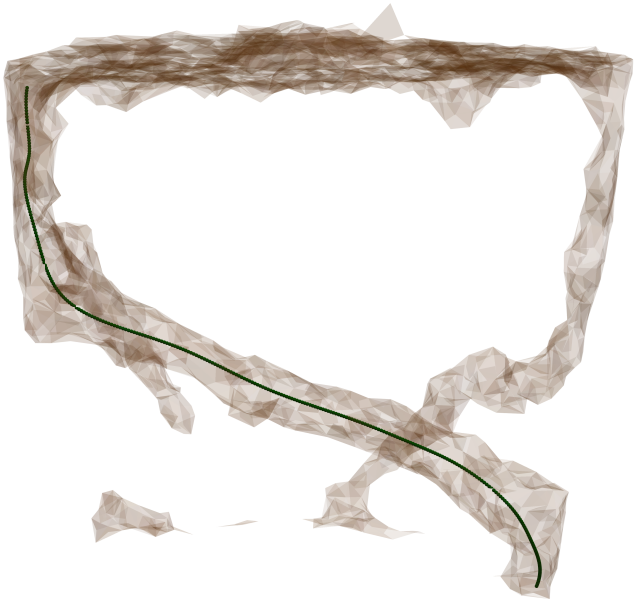

Figure 4.10: Experiment 2 tunnel 1.

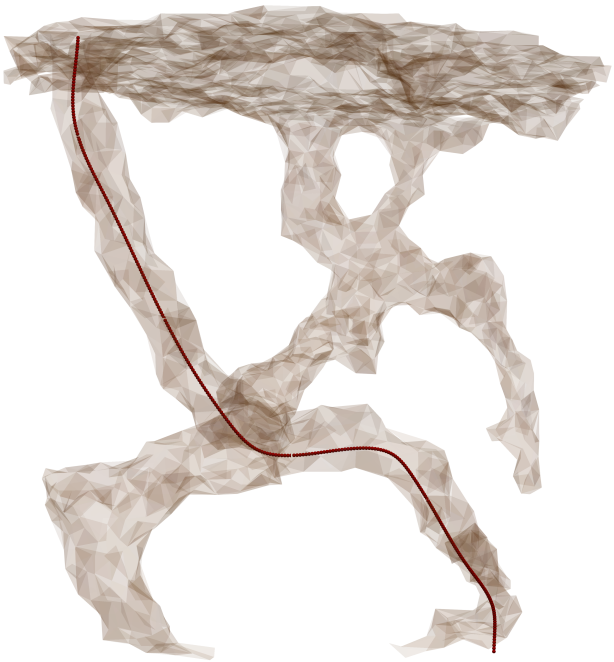

Figure 4.11: Experiment 2 tunnel 2.

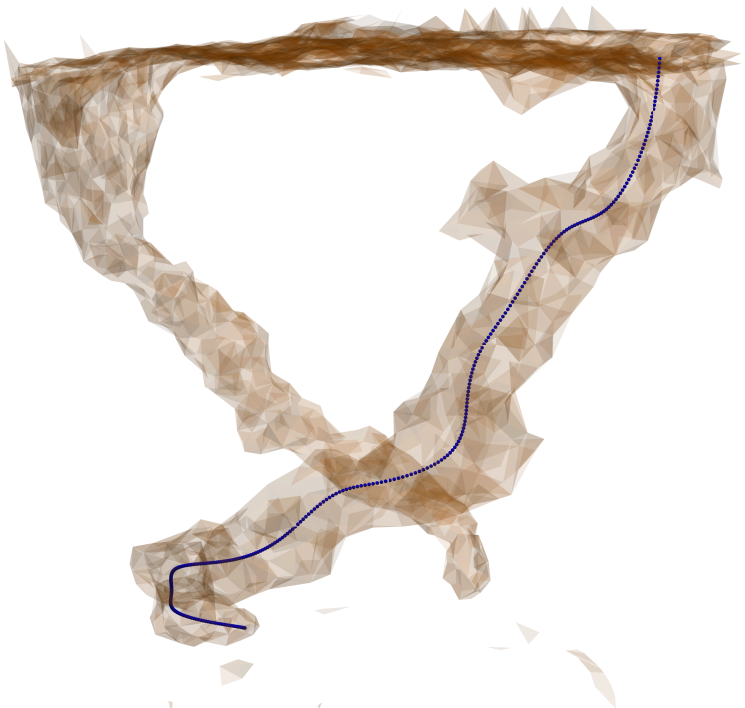

Figure 4.12: Experiment 3 tunnel 1.

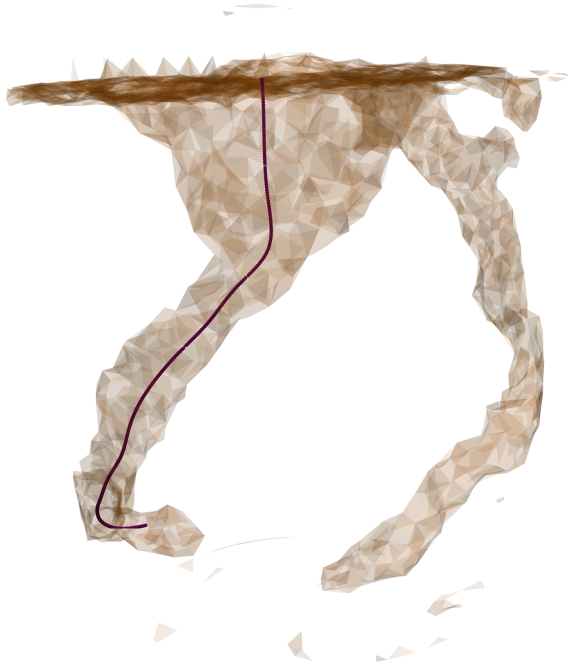

Figure 4.13: Experiment 3 tunnel 2.

Chapter 5

WHAT IS SHAPE? CHARACTERIZING PARTICLE MORPHOLOGY WITH GENETIC ALGORITHMS AND DEEP GENERATIVE MODELS

PUBLISHED CONTENT AND CONTRIBUTIONS

Buarque de Macedo, Robert et al. (2022). "What is shape? Characterizing particle morphology with genetic algorithms and deep generative models." In: *Granular Matter, in review*.
R.B. helped with the conceptualization of the project, writing the relevant code, analyzing the data, and writing the manuscript.

Topology optimization — the automated design of a material's structure to engineer a desired property — has demonstrated promise across multiple fields (Jihong et al., 2021). Due to exponential growth in computing power and algorithmic developments, computers have 'invented' functional structures, including: satellite brackets, cantilevers and lattice materials (Rosinha et al., 2015; Jihong et al., 2021; Cheng, Bai, and To, 2019). Nonetheless, topology optimization is inherently challenging due to the high dimension of the design space. As such, it is beneficial to parameterize the solutions with as few variables as possible, effectively reducing the dimension of the design space (Kumar and Kochmann, 2021). This process is prone to loss of critical information and it requires a deep understanding of the optimization problem. To overcome this, recent methods have leveraged deep learning to automatically discover a reduced number of parameters needed to uniquely define a class of solutions. For instance, Wang et al. utilized a deep learning architecture known as a variational autoencoder (VAE) to construct a finite dimensional vector space, or 'latent space' of microstructures (Wang, Chan, et al., 2020). Each vector in the latent space within certain bounds defined a unique and valid material microstructure. Further, the dimension of the latent space was significantly lower than that of the original binary image of the microstructure. Such a vector space is invaluable to topology optimization, as optimization algorithms can be easily run in the continuous, complete and relatively low dimensional latent space. In this work, we apply recent developments in topology optimization to granular materials.

Granular materials — any collection of discrete-solid objects — are ubiquitous in both nature and industry (Oda and Iwashita, 2020). Soils, ball bearings, and even asteroids can be classified as granular, and their behavior is approximated by rigid body dynamics (Makse, Johnson, and Schwartz, 2000; Kollmer, Lindauer, and Daniels, 2016). Thus, certain attributes persist across granular materials on multiple scales. One such phenomenon is jamming: when a collection of particles transition from a fluid-like flowing state to a solid-like locked state (Behringer and Chakraborty,

2018). Recently, engineers and artists have attempted to design granular materials which take advantage of this unique jamming property for achieving desired functionality. Examples include self-supporting structures for housing, fabric which can transition from soft to stiff with pressurization and robotic grippers. (Keller and Jaeger, 2016; Wang, Li, et al., 2021; Brown et al., 2010) . A primary challenge in designing such substances is picking the shapes of the individual grains. Spherical particles tend to pack tightly, but do not have tensile strength when uncompressed. On the other-hand non-convex grains may entangle with each other and provide tensile strength, but pack loosely (Graaf, Roij, and Dijkstra, 2011). Consequently, finding the optimal morphology for a set of design specifications remains an open, yet crucial, problem.

Discovering the ideal grain structure for optimizing a macroscopic property such as tensile strength is a daunting task because of the infinite number of shapes one may consider. One method of exploring the high dimensional phase space of shapes is with genetic algorithms (GAs) (Holland, 1992). Jaeger et al. (Jaeger and Pablo, 2016; Miskin and Jaeger, 2013; Miskin and Jaeger, 2014) utilized GAs to evolve a particle morphology in order to maximize packing fraction in discrete element method (DEM) simulations (Cundall and Strack, 1979a). Nonetheless, the technique was limited to clumps of spheres due to the limitations of traditional DEM. On the other hand, Makse et al developed a formula for estimating packing fraction and coordination number for arbitrary particle shapes by constructing the Voronoi volumes from sphere clusters (Baule and Makse, 2014). Such an equation could be invaluable for use in topology optimization, as unlike simulations it can be quickly evaluated. Nonetheless, it assumes maximum packing density, and may not be accurate when meta-stable states such as arches occur in samples.

A way to reduce the computational requirement of automated grain design is by finding a function mapping from grain shape to material-scale behavior that can be quickly evaluated. One can then invert this ‘forward’ mapping from morphology-to-behavior to obtain an ‘inverse’ mapping from behavior-to-morphology. Creating this ‘inverse’ mapping is highly non-trivial and non-unique but of great scientific interest. In the last few years, such a mapping has been investigated for a multitude of shapes and behaviors using experiments and simulations, as analytical solutions for even simple shapes remain elusive. Commonly explored shapes in jammed particle simulations include spheres, cylinders, superballs, staples, ellipses and ellipsoids, sphere clusters, crosses, spherocylinders, tetrahedra, frustums, platonic solids, and

realistically shaped grains - though for the latter there are few computational efforts due to technical limitations (An et al., 2009; Gan and Yu, 2020; Salerno et al., 2018; Gravish, Franklin, et al., 2012; Guises et al., 2009; Graaf, Roij, and Dijkstra, 2011; Meng et al., 2012; Li, Lu, et al., 2013; Zhao et al., 2011; Baker and Kudrolli, 2010; Jerves, Kawamoto, and Andrade, 2016). In all such cases, material properties continuously vary with particle shape.

The above studies suggests that a continuous function exists mapping particle shape to characteristic mesoscopic properties like average coordination number and packing fraction. However, each study only considers a small 'slice' of the entire function's domain. In this work, we demonstrate a methodology for constructing the general mapping from shape to material properties by parameterizing particle shape, and finding relationships between the chosen parameters and granular material properties. Tackling this herculean task is now possible due to recent technological advancements. These being: 1) the level-set discrete element method (LS-DEM), a DEM which can efficiently simulate particles of arbitrary shape (Kawamoto et al., 2016), 2) granular cloning, which allows the generation of particle shapes with user-specified properties (Buarque de Macedo, Marshall, and Andrade, 2018), and 3) neural-network based generative models, which can dramatically reduce the dimension of high-dimensional phase spaces by leveraging non-linear patterns in the data (Doersch, 2016).

We first explore human chosen parameterizations of particle shape (morphological descriptors), and how these parameters affect packing fraction ϕ (ratio of solid to total area in a granular material) and coordination number Z (average number of grain-grain contacts per particle). In particular, we see how grain roundness, aspect ratio and convexity affect material properties. As these three parameters can not uniquely define a shape, we utilize a VAE to develop a 20-dimensional granular particle latent space. In such a space, each vector represents a unique particle shape. Finally, we demonstrate how such a latent space can be utilized for shape optimization, see Figure 5.1. By attempting to define the shape of a particle with the minimum number of parameters, we ask: what is necessary to define a morphology? In other words, what is shape?

This paper is organized as follows. First, the methods of generating unique particles shapes is detailed in 5.1. Next, the simulation engine and methods are explained in 5.2. The results are then presented and analyzed in 5.3, followed by the conclusion and suggestions for future work in 5.4.

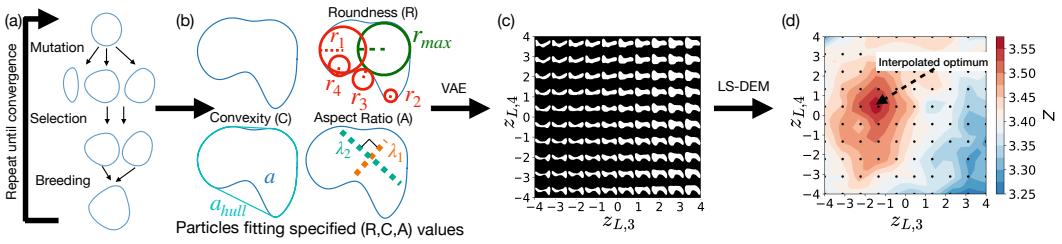

Figure 5.1: Overview of topology optimization framework. (a) Obtain diverse collection of particle shapes from GAs which match specified (R,C,A) values. (b) Parameters for calculating (R,C,A). (c) Create continuous vector space of shapes with VAE. $z_{L,i}$ denotes the i^{th} latent space vector, as described in section 5.1. Sampling of shapes shown at evenly spaced vectors along a plane in latent space, with axes $z_{L,3}$ and $z_{L,4}$. The plane is defined by S (Equation 5.6). (d) Run simulation for each shape at grid points (black dots) in latent space and obtain material property (Z). Use interpolation or optimization to find optimal particle shapes between grid points.

5.1 Particle generation methods

Generation with genetic algorithms

To start, we choose to continuously vary the convexity C, roundness R and aspect ratio A of the particles as it is well documented that such properties have a significant effect on material behavior (Jerves, Kawamoto, and Andrade, 2016; Yang and Luo, 2015). Thus, each shape generated can be represented as a point in this three-dimensional parameter space, with coordinates given by (R, C, A). We investigate whether these dimensions are sufficient for predicting the properties at the mesoscale, or if more dimensions are required. These shape descriptors are defined for a given particle as follows:

$$R = \frac{\sum_{i=1}^{N} \frac{r_i}{N}}{r_{max}} \tag{5.1}$$

$$C = \frac{a_{hull}}{a} \tag{5.2}$$

$$A = \frac{\lambda_1}{\lambda_2} \tag{5.3}$$

where N is the number of corners on a particle, r_i is the radius of curvature r of the i^{th} corner, r_{max} is the radius of the largest circle that can fit entirely within the particle, a and a_{hull} are, respectively, the area of the particle and the area of the convex hull of the shape and $\lambda_1 \leq \lambda_2$ are the principal component magnitudes of the points on the surface of the particle, see Figure 5.1. Note all 3 parameters take values between 0 and 1, with 1 corresponding to the values for a disk.

In order to investigate how ϕ and Z change with these three dimensions, it is necessary to generate a wide range of particle shapes covering the (R, C, A) space. Generating new particle shapes autonomously, or 'granular cloning,' is an active area of research (Jerves, Kawamoto, and Andrade, 2017; Zhou and Wang, 2017; Shi et al., 2021). Most methods require an external repository of particle shapes which are used as a blueprint for new shapes. However, we wish to generate particles from shape descriptors alone. The method proposed in (Buarque de Macedo, Marshall, and Andrade, 2018) allows one to do this. Here, a GA morphs a particle's shape until the grain matches the shape descriptors to a certain tolerance. Clearly, multiple realizations of particle shape may correspond to the same (R, C, A) value. Hence we generate 10 particle realizations for each point on a grid in (R, C, A) space, evenly spaced by 0.1, with $R \in [0.2, 1.0]$, $C \in [0.7, 1.0]$ and $A \in [0.2, 1.0]$. We restrict our attention to $C \geq 0.7$ which still leads to pronounced nonconvexity (see Figure 5.3) while ensuring that the genetic algorithm produces physically valid morphologies.

The engine used for the GE is python DEAP (Fortin et al., 2012). To summarize, the method deforms an ellipse to match a target set of morphological properties. In this case, the properties are a specified roundness, aspect ratio and convexity. The method begins by placing 8 equally spaced points along the perimeter of an ellipse, with the ellipse having the specified aspect ratio and area equal to 300. Then, a genetic algorithm perturbs the points until the morphological properties of the particle are within a tolerance of the specified properties. By using 8 points uniformly distributed across the surface to build the particle, we have chosen a 'scale' for the morphology of about particle diameter d/10. This is a common length scale for quantifying particle roundness (Cho, Dodds, and Santamarina, 2006a).
The genetic algorithm consists of 3 steps: mutation, combination and selection. The algorithm begins with 50 equivalent ellipses, or 'individuals.' Random individuals are selected for mutation with probability 0.5. For individuals undergoing mutation, points on the particle boundary are selected with probability 0.5. In polar coordinates, the radial component r of the particle is moved in the radial direction by a random number sampled from the Gaussian $\Delta r \sim \mathcal{N}(0.0,\ 1.0)$ and change in polar angle $\Delta\theta \sim \mathcal{N}(0.0,\ 0.05)$.

Next, the 'cost' of each individual is calculated for selection. The cost of an individual is given by

$$\text{cost} = (C - C_{target})^2 + (R - R_{target})^2 + (A - A_{target})^2 + 100 \sum_{i=1}^{N} \delta(\frac{r_i}{r_{max}} < 0.08) + 100SI + 100BN. \quad (5.4)$$

The subscript 'target' is the specified shape parameter value, and the squared difference is the squared error, a measure of the difference between the current individual and the target morphology. The fourth term in the cost function heavily penalizes the morphology for each corner with a normalized radius of curvature $\frac{r_i}{r_{max}}$ less than 0.08, thereby avoiding non-physical sharp edges. The SI term is equal to 1 if the particle self-intersects, heavily penalizing this non-physical behavior. The parameter is checked using the Bentley-Ottmann algorithm (Bentley and Ottmann, 1979). The BN term heavily penalizes 'bottlenecks' in the shape, i.e. when two points on opposite sides of the particles are squeezed close to one-another. It is equal to 1 when two opposite points are within a distance 7 of one-another. It is difficult to create consistent level sets from grains with bottlenecks. Minimizing this cost function produces a particle with the specified morphological parameters that is physical. In the selection step, pairs of individuals are randomly chosen, and the individual with a higher cost is eliminated. The remaining individuals are duplicated until the population size is back to 50.

Measuring particle roundness requires identifying corners on the particle at a relevant length scale. Given the points on the particle surface, the corners are identified as follows: First, a third-order spline is fit to the points. The spline is then smoothed, from which 500 ordered points on the smoothed particle surface are generated. The radius of curvature can be calculated at each of these points due to the smoothness of the spline. For each point, the radius of curvature of all points 20 ahead and behind are checked. If the radius of curvature of the current point is the minimum out of all the checked points, it is considered a corner. The radius of the maximum sized circle that can be fit in the particle is easily calculated from the level set: $r_{max} = |\min(\Phi)|$, see Figure 5.2.

Finally, in the combination step pairs of individuals are randomly selected with probability 0.2. A new individual, or 'child' is created by randomly swapping boundary points on both grains.

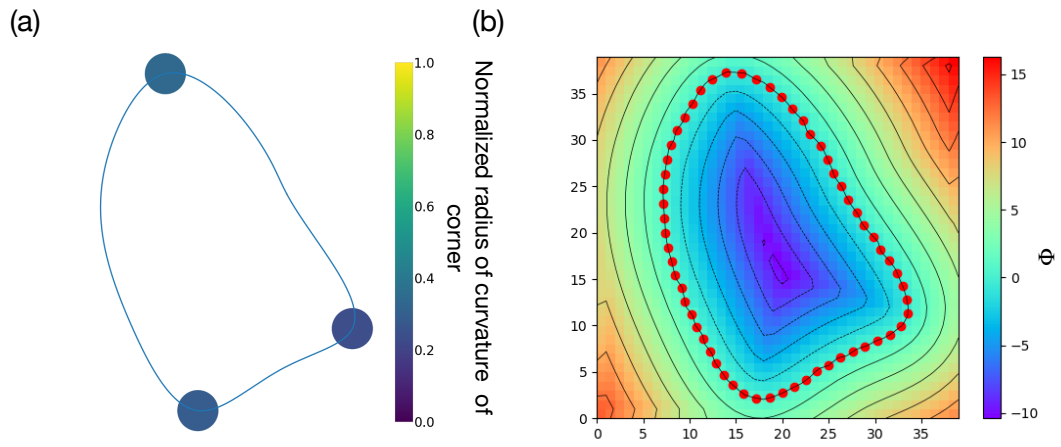

Figure 5.2: Diagrams of particle corners and level set. (a) Corners detected by corner detection algorithm, with normalized radius of curvatures shown. (b) Points on the surface of a particle, with the grain's level set Φ given as a heatmap.

This entire processes is repeated for 500 'generations,' or until the minimum cost of an individual is below the tolerance $\epsilon = 0.0005$. After convergence, the individual with minimum cost is taken to be the solution. The location of the points are saved, and the level set for the particle is automatically generated. If generation 500 is reached and convergence has not occurred, the algorithm selects a different combination of target parameters. Note that all parameters can be modifieid to genereate different classes of shapes.

For each realization of an (R, C, A) point, a simulation is performed to generate a packing and subsequently ϕ, Z are calculated. An example of a generated grain for each sampled point in (R, C, A) space is given in Figure 5.3.

Generation with deep learning

While the classical, intuition based descriptors (R, C, A) can capture a significant amount of information about a particle's shape, they are not sufficient to fully quantify grain morphology. For instance, an infinite number of unique shapes could have the same (R, C, A) coordinate. The limitations of these descriptors can be seen in the results for ϕ in section 5.3 for high convexity and in Z for low convexity morphologies. Here, the dependence of ϕ on roundness and aspect ratio is complicated, implying there may be additional dimensions necessary to fully classify the grains. Consequently, we pose the question: what is the minimum number of dimensions necessary to sufficiently quantify 2D particle shape, in relation to its collective packing properties? Further, what are these dimensions?

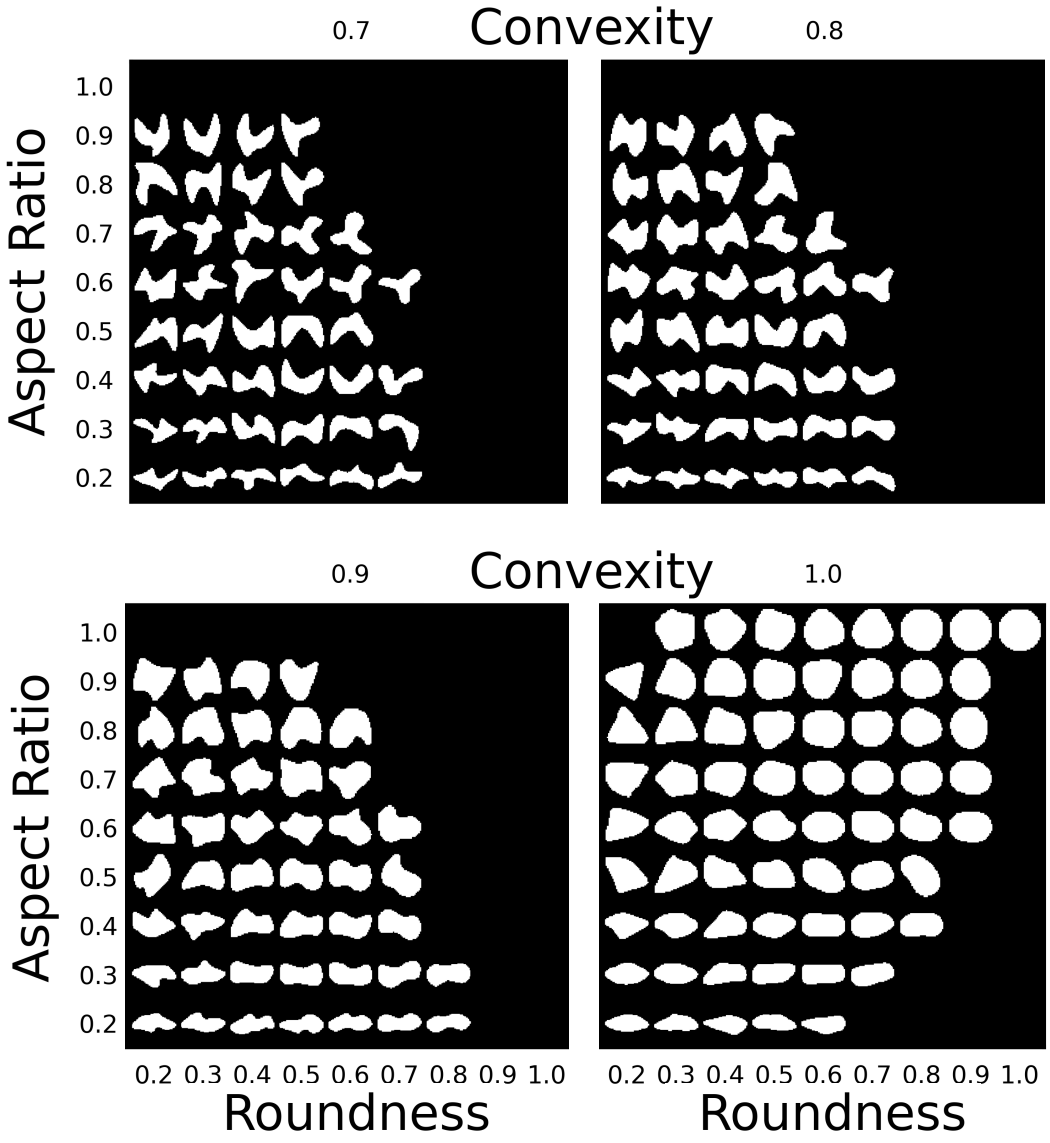

Figure 5.3: Example of grains generated at grid points in R, C, A space. Empty boxes indicate the algorithm was unable to generate a particle with the prescribed (R, C, A) values. Each box represents a different convexity, with A as row and R as columns.

Advances in machine learning offer tools for answering these questions. We utilize a VAE (Pu et al., 2016), which has recently been leveraged for generating unique and realistic granular particles (Shi et al., 2021). The input to a VAE is an array of numbers, which in our case is the grey-values in a pixelated 64x64 2D image of a particle. The array is acted on by a series of matrix operations and non-linear functions, referred to as 'dense' layers. These operations include multiple convolutions, a commonly used operation in networks learning with image data. The transformed data is then fed into two arrays: μ and σ. Both of these vectors are the same length d, which is a parameter chosen by the user. This first half of the network is dubbed an 'encoder,' as it compresses the data from the original image into d dimensions. Next, a 'sample' z is chosen by sampling from the distribution $z = \mu + \sigma \odot \epsilon$, where ϵ is a random standard normal variable sampled at evaluation time and $\odot$ is the element-wise dot product. The second half of the network is a series of convolutions that reconstructs the original image from z. This section of the network is called the 'decoder.' The loss function for the network is a measurement of the difference between the input image and the reconstructed image, and the similarity between the distribution of the training data in the latent space and a standard normal distribution. The parameters in the network are trained via back-propagation. Once trained, the network has learned how to compress the image into d dimensions such that the loss function is minimized.

The architecture of the encoder, which takes 64x64 black and white (single channel) images as input is given in table 5.2, while the decoder architecture is given in table 5.3 (Appendix). A general diagram of the architecture is displayed in Figure 5.4.

The VAE parameters η and θ, representing the weights connecting neurons in the encoder and decoder network respectively, are tuned during training as to minimize the following loss function for each of the data points where x_i is the i^{th} training data point:

$$l_i = -\mathbb{E}_{\mathbf{z}\sim q_\theta(\mathbf{z}|x_i)}[\log(p_\eta(\mathbf{x}_i|\mathbf{z}))] + KL(q_\theta(\mathbf{z}|\mathbf{x}_i)||p(\mathbf{z})) \tag{5.5}$$

The first term is the 'reconstruction loss,' and measures the difference between the input and the output image for data point x_i, while the second term (Kullback–Leibler divergence) encourages the distribution of data in the latent space $\mathbf{z}$ to be Gaussian. p and q represent probability distributions learned by the network. For details on all terms and derivation, see (Doersch, 2016). Code for variational autoencoder from (Rath, 2021).

We train a VAE on 10,000 unique images of particles generated by the genetic algorithm across a uniform sampling in (R, C, A) space. The grains are rotated and translated such that the principal axis of the grain is horizontal, and the grain centroid is in the middle of the image. The grain is converted into a black and white image, with the particle being white and the outside the particle black. The image is then subdivided into 62 pixels horizontally and vertically, with two empty pixels used to pad the sides of the image. These images are then used to train the network. We find that $d = 20$ is the lowest value of d necessary for successful reconstruction. Any lower, and the reconstruction loses too much structure when compared to the original image. Once trained, the encoder section of network can generate 2 unique d-dimensional vectors, μ and σ, for any given particle shape. Likewise, for any sample vector z the decoder can generate a unique particle shape. The d dimensional vector space of z is a latent space, where each vector defines a unique grain.

With the VAE, we achieve the goal of finding a complete set of dimensions for fully describing particle shape, such that the number of dimensions are minimized to avoid redundancy. By discovering a function with this latent space as the domain, and mesoscal variables such as ϕ as the range, we would have a means of quickly predicting the mechanical properties of granular materials with arbitrary shaped grains.

We compute a z for each particle in the training data. The data is then scaled

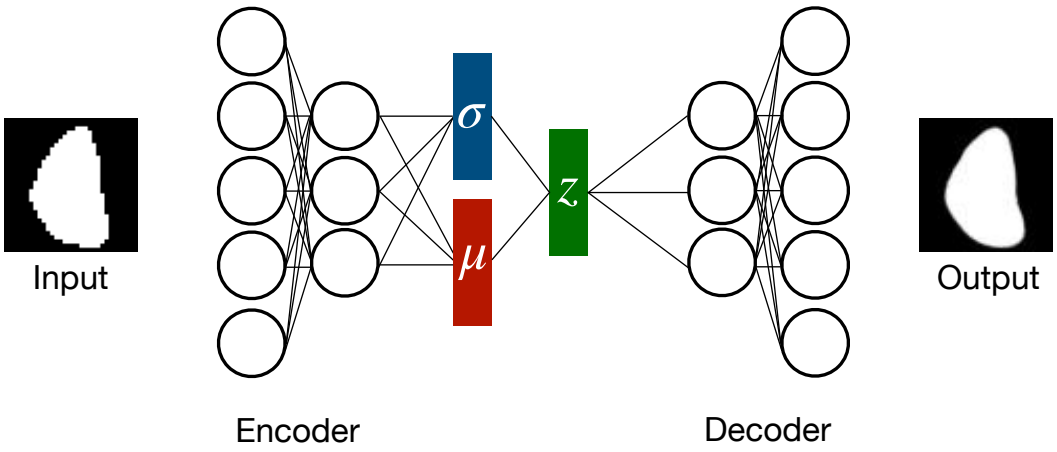

Figure 5.4: Diagram of a VAE. On the left is the input, which is a pixelated image of a grain in this case. On the right is the reconstructed image that is output by the network. Note the network smooths the particle somewhat, representing a certain degree of lost information.

and rotated to reduce remaining correlations between the data points in the latent space using principal component analysis (PCA) (Jolliffe and Cadima, 2016). The transformed z vectors are given by z_L, with i^{th} components $z_{L,i}$. Each z_L lives in the d-dimensional latent space, with basis vectors $(b_1, ..., b_d)$. It is found that outside of the range $-4 \leq z_{L,i} \leq 4$, corresponding particles tend to be non-physical, i.e. containing disconnected regions. For computational tractability, only latent vectors in the somewhat arbitrary subspace S are simulated in this study, where:

$$S = \{(0, -4, z_{L,3}, z_{L,4}, 0, ..., 0) \in \mathbb{R}^{20}\}. \tag{5.6}$$

However, the methods applied here are valid in any subspace of the latent space. S is chosen because of the high diversity of particle shapes defined by the space. A uniformly spaced 2D grid is defined in S with grid spacing 0.8 between bounds $-4 \leq z_{L,3}, z_{L,4} \leq 4$. A particle is generated from each z_L grid point for use in simulation. The particle shapes corresponding to each grid point are displayed in figure 5.1.

5.2 Simulation methodology

In order to measure ϕ, Z and any other mesoscopic quantity for a range of shapes, we leverage a specialized 2D DEM simulation. DEM was developed for disks that obey rigid body mechanics (Cundall and Strack, 1979a). In DEM, disks are allowed to overlap by a very small amount. The contact force between two disks is a function of the overlap extent between two particles. Nonetheless, LS-DEM (level set DEM) allows DEM simulation of arbitrarily shaped grains, and thus is capable of simulating any physically possible shape created by the generative models.

LS-DEM (Kawamoto et al., 2016) stores the location of a collection of points on the surface of the particle, in addition to the level set of each grain. The level set Φ for a given particle surface is a function defined in all of space, such that its value at a given point is the signed distance to the surface of the grain. Φ is positive outside the grain, and negative inside, pictured in Figure 5.2. When the surface of one grain intersects another, the penetration extent is easily computed by looking up one particle's level-set value at the location of the other particle's surface points, and performing linear interpolation on the level-set value if necessary.

Each (R, C, A) simulation consists of 900 particles at a gas state, i.e. randomly distributed in an evenly spaced non-overlapping grid such that grains are not touching one-another with uniformly distributed random velocity and rotation. The horizontal and vertical grid spacing is 6 m, with 15 particles per row. The initial speed is a

Parameter	(R,C,A) sims	VAE sims
Box width lx (m)	108	64
Box height ly (m)	402	402
Particle area (m^2)	6	variable
Density (kg/m^3)	2650	2650
Normal spring constant k_n (kg/s^2)	10^{11}	10^{11}
Tangential spring constant k_s (kg/s^2)	10^{11}	10^{11}
Coefficient of friction μ	0.5	0.5
Normal coefficient of restitution C^n_{res}	0.4	0.4
Shear coefficient of restitution C^s_{res}	0.5	0.5
Number of unique grain shapes per simulation	10	1
Total number of grains	900	1800

Table 5.1: Table of simulation parameters

randomly chosen number between -20 to 20 ms^{-1} in a random direction, with 0 angular velocity. The initial conditions are chosen randomly in order to make sure the final sample is less dependent on initial conditions.

Each particle in the (R, C, A) simulation has the same area. Simulations for VAE generated grains contain 1,800 particles, as it is found for very non-convex particles generated by the VAE the representative volume element (RVE) requires more grains (see below). Particles generated from the VAE are scaled such that each pixel edge length in the 64x64 image is equal to 0.045 m. Particles are arranged in a grid with the same spacing as in (R, C, A) simulations. Simulations parameters are given in table 5.1.

The grains are left to fall under the influence of gravity until they reach a loosely packed jammed state. The simulation is run until the system is at rest. The packing fraction, in 2D, is calculated for the jammed state by first performing a Voronoi tessellation on the points on the particles' surface in order to calculate the area of the domain, then using the known area of the grains to calculate ϕ for a given RVE. Z is computed by measuring the average number of grains a given particle is contacting.

Calculation of material properties such as ϕ and Z requires defining a representative volume element (RVE), i.e. an area in the simulation domain over which these parameters can be found. The RVE size of a granular material requires calibration. If the RVE is too small, it is not representative of the mesoscopic properties. However, too large of an RVE will include the rigid wall boundaries, which will skew results. We take a circle of radius D = 50 m centered at the centroid of grain

positions to be the RVE, from which Z and ϕ are calculated for each simulation. The value of $D = 50$ is determined by testing for convergence in mesoscale properties, see appendix section 5.5.

Each simulation is repeated 5 times, with the same particles but different initial velocities, positions and orientations. The average ϕ, Z of these 5 simulations are recorded. Examples of simulations before and after pluviation are displayed in figure 5.5B.

5.3 Results and analysis

(R,C,A) simulations

ϕ and Z measurements are given in Figure 5.5A. The data exhibits multiple patterns. The most obvious trend is that decreasing convexity decreases both packing fraction and coordination number. This is also evident from Figure 5.5B and comparing figure 5.6A,D,G and J: as convexity decreases, the porosity of the material increases substantially. This is due to contact occurring at corners of highly non-convex grains leading to empty space within the grain's non-convex indent, or arches forming within the material around large voids (Figure 5.6J) similar to cohesive granular materials (Rognon et al., 2006).

For high convexity grains $C = 1$, ϕ gradually changes in the R, A plane, except for very low A, at which ϕ rapidly decreases. The high values of ϕ at $(R, C, A) = (1.0, 1.0, 1.0)$ and $(R, C, A) = (0.2, 1.0, 0.2)$ are due to the hexagonal-like (Figure 5.6A) and tessellating (Figure 5.6B) packings that occur with grain shapes near these locations, respectively.

Z is strongly affected by A for all $C >= 0.7$ Elongated grains exhibit local nematic order by tending to pack side-by-side (Figure 5.6C,F,I,L). This packing is similar to what is observed with ellipses. So is the trend in Z: elongating the particles increases the average number of contacts. However, as convexity decreases, the elongated grains exhibit less orientational order and the trends in Z become more complex (Guises et al., 2009).

The patterns in ϕ in the $C = 0.9$, $C = 0.8$ and $C = 0.7$ plane are similar: maxima is achieved in the (R, A) plane at $(R, A) \approx (0.7, 0.4)$ (Figure 5.6E,H) for $C = 0.8/0.9$, and $(R, A) \approx (0.6, 0.3)$ for $C = 0.7$(Figure 5.6K) . Interlocking is present for both of these maxima, yet the prevalence decreases with decreasing convexity. Particles far from the maxima exhibit less interlocking and pack loosely (Figure 5.6D,G,J). The decrease in ϕ as R is decreased for low convexities is related to loss of interlocking.

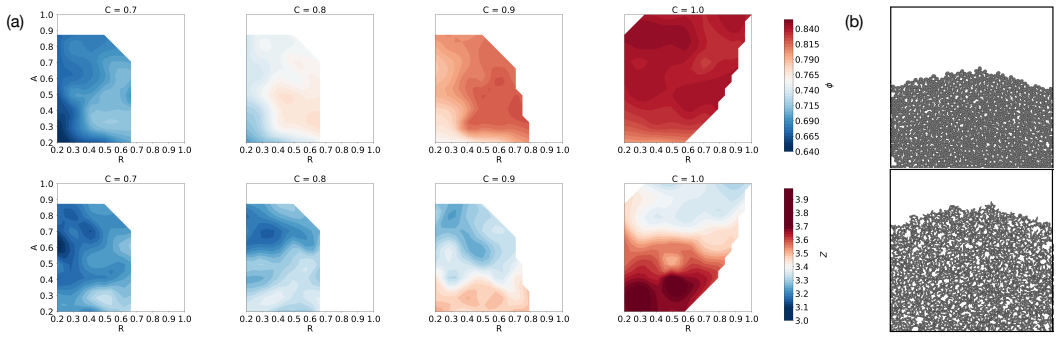

Figure 5.5: RCA simulation data. (a) Average ϕ, Z in R, C, A space. Top row: ϕ values. Bottom row: Z values. Columns correspond to convexity, matching Figure 5.3. White blocks are locations where there are too few points for interpolation. (b) final state of two R,C,A simulations at (0.7,1.0,0.7) (top) and (0.3,0.7,0.2) (bottom).

In general, the (R, C, A) basis is effective at categorizing this diverse collection of shapes. The function mapping (R, C, A) to Z and ϕ appears smooth. Nonetheless, in the $C = 1$ plane the ϕ values vary more non-smoothly. Further, the space is full of 'holes' where a particle shape could not be found. These observations imply additional dimensions may be necessary to quantify shape in a continuous and complete sense. Exploring such additional coordinates is the subject of the next section.

VAE-generated particle simulations

For each particle on the uniformly spaced grid in S (see 5.1.) a pluviation simulation of 1,800 identical copies of the particle is carried out, as detailed in 5.2. The results for ϕ and Z in the subspace S are given in Figure 5.7. Unlike Figure 5.5, the ϕ,Z function is defined for all of S, as a shape is guaranteed to exist for any vector - though the probability of a consistent shape decreases outside the $-4, 4$ bounds. In S, the particle with the highest packing fraction is predicted to be in the top right, or the $(4, 4)$ location. This corresponds with a relatively convex shape, see inset. Meanwhile, the particle with the maximum coordination number is around the $(-1.5, 0.5)$, matching the elongated 'bar bell' shape in Figure 5.1 - a stretched, lower aspect ratio shape. Both optimums are consistent with observations in section 5.3. As neither of these particles were in the training data for the VAE, the program has 'invented' an entirely new shape for optimizing a material attribute.

This research has focused on the 'forward' problem of granular design: mapping particle shape to mesoscopic or bulk properties. That being said, these tools can be applied towards the 'inverse' property-to-bulk problem. With an approximate

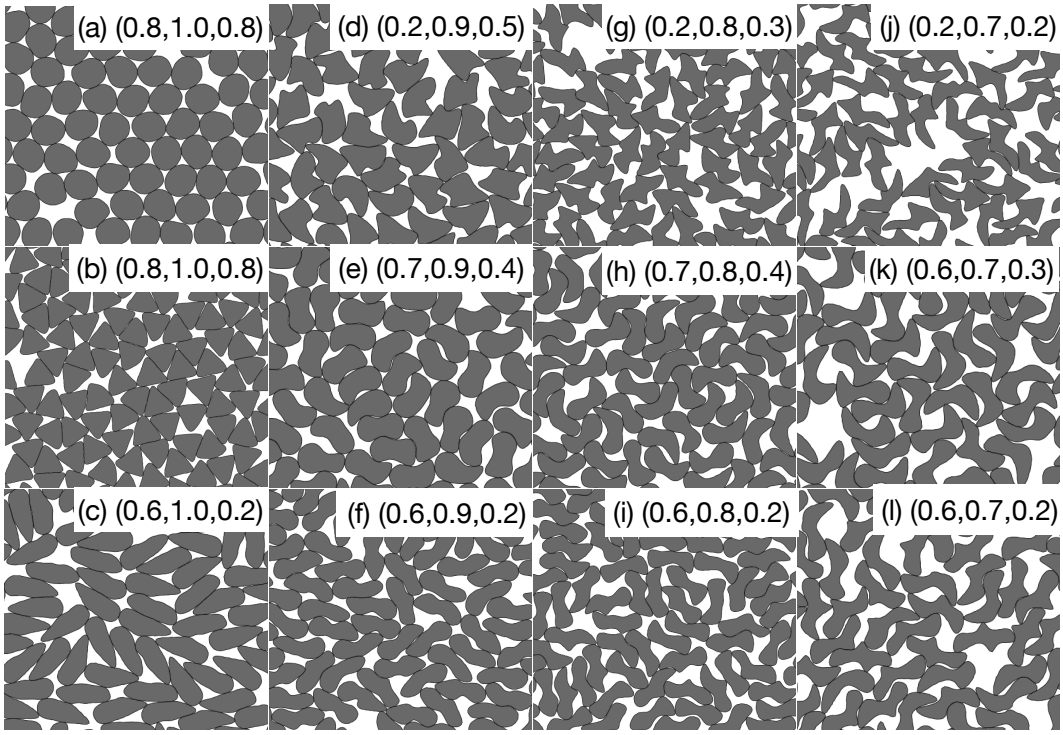

Figure 5.6: Examples of pluviated packing configuration across (R,C,A) space. Corresponding (R,C,A) value for each packing given in top-right corner. Particles exhibit hexagonal packing (a), tessellation (b), nematic ordering (c,f), interlocking (e,h,k), arching (j) and propensity for corner contact (d,g,j).

forward mapping from latent space vector to bulk property in hand, one can search the latent space for areas of optimal bulk properties such as yield stress. Once an area in latent space has been identified, LS-DEM simulations can be run using particles sampled from this area to achieve a finer sample of bulk properties. This process can be repeated for other candidate areas of the latent space, thereby performing topology optimization (see Figure 5.1). This is similar to the method in (Gladstone et al., 2021), which performs optimization within the lower dimensional latent space to reduce the complexity of the problem.

5.4 Conclusions

In this work, we have investigated mappings from parameterized spaces of particle shape to mesoscale material quantities, Z and ϕ. We have shown how parameterizing morphology by roundness, sphericity and aspect ratio can successfully be used to predict material properties. In particular, we have found that ϕ and Z continuously vary throughout the shape space due to intuitive changes in packing geometry characterized by tessellation, local nematic ordering, hexagonal packing, arching

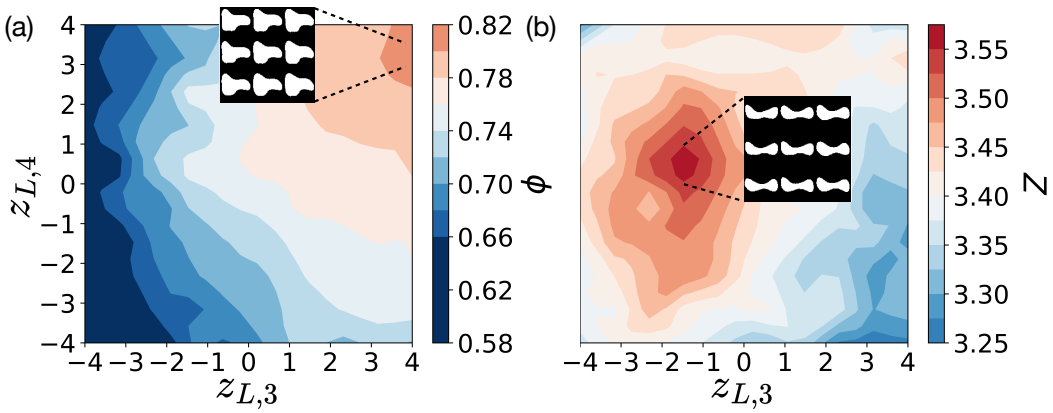

Figure 5.7: Average ϕ (a) and Z (b) measured for uniform square grid in S space where z_L^i denotes the i^{th} latent space vector (see Section 5.1) with interpolation between points. Particles close in latent space to maxima shown.

and interlocking. We have also outlined a method for fully and automatically parameterizing particle shape via VAEs.

In future work, the techniques developed can be easily extended to 3 dimensions. Future work should also consider larger collections of particles, such to further minimize the effects of wall boundaries. Next, our results have only considered pluvation-prepared samples. However, mesoscale properties in granular materials are highly dependent on initial conditions (Staron and Hinch, 2007). Thus, it would be useful to understand how the ϕ and Z values corresponding to a particular shape change with preparation method. For instance, particles could be compressed or tapped to achieve higher packing fractions. Also, it would be valuable to see how results change with frictionless grains as qualitatively different packing configurations may be achieved. Further, the methodologies presented can be applied to any mesoscale or bulk material property — including tensile strength and critical state parameters. This mapping could also be used in coarse grained data-driven models, where model parameters are learned from lower-scale simulations (Karapiperis et al., 2021). Additionally, it could facilitate the 'engineering' of a confined fluid's thermodynamics (Monfared et al., 2020). Finally, our results suggest particle morphology can be fully characterized using a few number of variables. Exploring the meaning of the dimensions chosen by the generative model could shed light on the nature of shape.

This methodology contains certain limitations. The genetic algorithm will not converge for certain morphological parameters, leading to the 'gaps' in RCA space.

Further, the genetic algorithm requires manual tuning, including mutation parameters and start conditions. The VAE overcomes many of these limitations as it can learn to generate particle shapes with minimal hand-tuning. Nonetheless, it is difficult to control the output of the autoencoder to only output particles of a certain class, such as with a constant convexity or roundness.

Previous research into granular materials was limited by the types of shapes one could simulate or obtain experimentally. Shape optimization of granular materials was limited to a small number of clustered of spheres, or relied upon theoretical results which may not always match DEM simulations. With these results, we open research avenues for exploring high-dimensional spaces of arbitrary grain shapes is LS-DEM simulations.

5.5 Appendix

Frictionless ellipse validation

We perform simulations of frictionless ellipses with a range of aspect ratios to validate our findings against previous results, see Figure 5.8. Results are generally very similar, with ϕ oscillating about 0.88 as the ellipse is elongated from a circle, followed by a decrease in ϕ that starts as A moves below 0.5. The insensitivity of the packing fraction to particle elongation in the aspect ratio range 0.5 to 1 in figure 5.8 differs from previous studies (Schreck, Xu, and O'Hern, 2010; Donev et al., 2007) which observed a decrease in ϕ as an aspect ratio 1 is approached. However, these studies used bi-disperse particles to prevent crystallization, while in our simulations of identical, frictionless particles the tendency to crystallize keeps the packing fraction high. Indeed, we note that LS-DEM produces almost perfect hexagonal packing for frictionless circles (A = 1), with ϕ slightly below 0.9.

Determination of RVE size

To discover the minimum RVE size for a given complete simulation, circles of increasing diameter D centered at the average of all the particles' centroids are considered, where D_i corresponds to the i^{th} circle of increasing diameter in steps of 1 m. Z_i is determined for the particles within each D_i diameter circle. A moving average of $\overline{Z_i}$ is computed by averaging Z_i with Z_{i-1} and Z_{i+1}. Then, $|\overline{Z_i} - Z|$ is calculated. This function quantifies the size of fluctuations in the value of Z as a function of D. As D is increased, this value is initially large due to the small RVE. However, the function oscillates about a smaller constant when D is sufficiently large enough to capture the general RVE behavior. As D is further increased, the RVE

Layer	Operation	Output dimension	kernel size	stride	padding	Activation function
1	2DConv	(64,33,33)	4	2	2	ReLU
2	2DConv	(128,17,17)	4	2	2	ReLU
3	2DConv	(256,9,9)	4	2	2	ReLU
4	2DConv	(512,5,5)	4	2	2	ReLU
6	2DConv	(1024,3,3)	4	2	2	ReLU
7	avg. pool	(1024,1)	N/A	N/A	N/A	None
8	linear	(2048,1)	N/A	N/A	N/A	None
9	linear	(20,1)	N/A	N/A	N/A	None

Table 5.2: Architecture of encoder. Input is a 64x64 black and white image (single channel) of the particle. Output is the μ vector and σ vector of latent space size d, 20. From here a sample z can be drawn.

Layer	Operation	Output dimension	kernel size	stride	Activation function
1	linear	(1024,1)	N/A	N/A	N/A
2	2DConvTranspose	(512,3,3)	3	2	ReLU
3	2DConvTranspose	(256,7,7)	3	2	ReLU
4	2DConvTranspose	(128,15,15)	3	2	ReLU
5	2DConvTranspose	(64, 31,31)	3	2	ReLU
5	2DConvTranspose	(64, 64)	4	2	Sigmoid

Table 5.3: Architecture of decoder. Input is sample z of size (d,1), drawn from normal distribution with mean μ and standard deviation σ, obtained from encoder. Output is a 64x64 reconstruction of the original image.

encompasses the boundary, and the value of the fluctuations suddenly change due to the boundaries' effect. The optimal value of D is when the domain is large enough to minimize the size of the fluctuations, but is minimally affected by the boundaries. This function of D becomes constant at about $D = 50$ m for the simulations, see Figure 5.9. The convergence of $|\overline{Z_i} - Z|$ for 900 particles and 1800 for (R, C, A) and VAE simulations, respectively, in addition to the small variation in calculated ϕ and Z from the simulations indicates that the number of grains used in the simulations is satisfactory.

VAE parameters

See Tables 5.3 and 5.2.

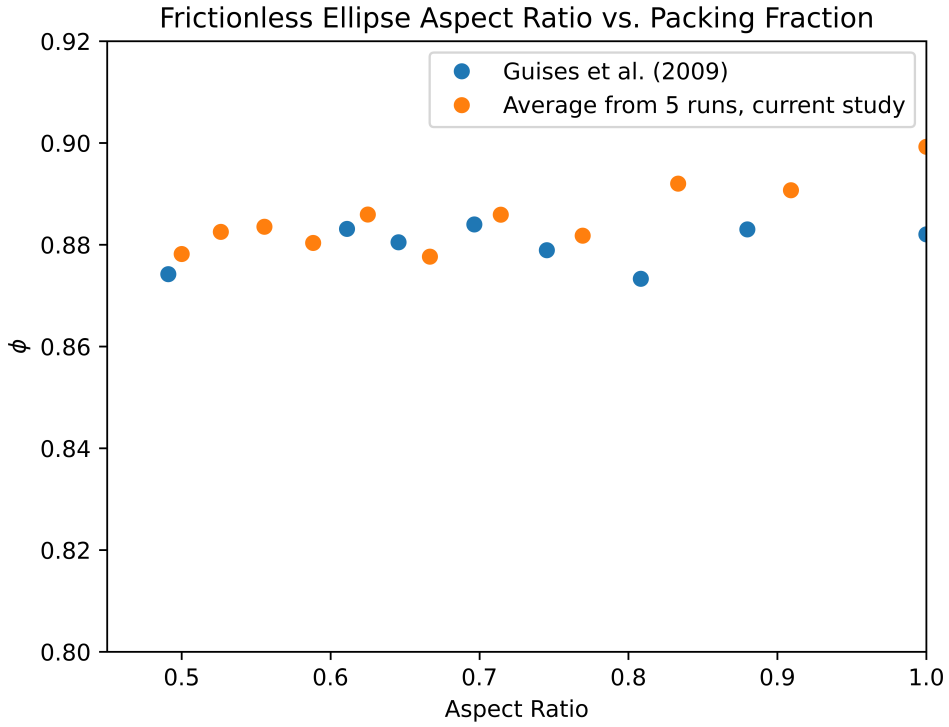

Figure 5.8: Packing fraction of frictionless ellipses, comparing results from current study with Guises et al., (2009)

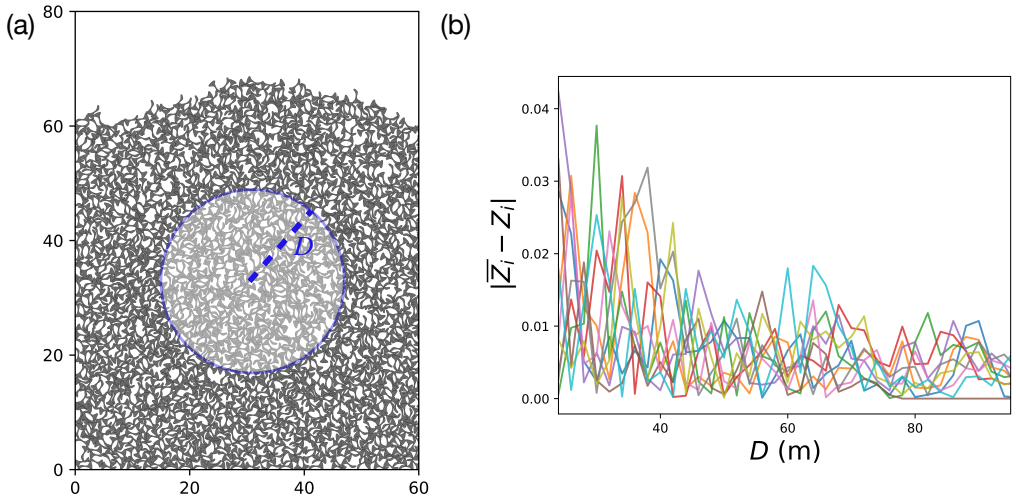

Figure 5.9: Data used to choose the RVE size. (a) Finished simulation of 1800 identical particles with RVE of diameter $D = 50$ m bounds shown in blue. Axis ticks in m. (b) $|\overline{Z_i} - Z_i|$ as a function of D for 10 simulations, with values for each simulation given by a unique color, see section 5.2. Convergence begins at about $D = 50$ m. Values after $D = 60$ m are unreliable as the RVE is greater than the box size.

Chapter 6

CONCLUSIONS AND OUTLOOK

6.1 Findings

In this thesis, we explored methods for optimizing granular material attributes at multiple scales. This ranged from autonomously controlling the shape of grains to achieve user-specified morphological properties, learning how ants manipulate granular materials to achieve stable tunneling, to the creation of a mapping from morphological attributes to emergent mesoscale properties that can be inverted for topology optimization.

In Chapter 3, genetic algorithms were utilized to build particles that matched the principle curvature and sphericity distributions of real grains. We found that tasking the genetic algorithm with matching these particular morphological characteristics lead to convergence, and that the morphological descriptor distributions of 3D generated particles closely matched that of the original grains.

In Chapter 4, XRCT images were taken of a soil sample during ant tunnel construction. Each grain was imaged, and an *in silico* re-creation of the experiment was performed in LS-DEM. We found that ants tended to dig at constant angles to the vertical direction, preferred to dig on the boundaries and had a slight preference for smaller particles. Further, we discovered that arches formed around the ant tunnels as the ants dug, stabilizing tunnels and reducing load on grains on the tunnel surfaces.

In Chapter 5, we leveraged the granular cloning algorithm developed in Chapter 3 to develop a mapping between grain morphological property and mesoscopic properties. We found that grains could be successfully generated using the genetic algorithm which matched a specified aspect ratio, roundness and convexity. We developed a mapping from these morphological properties to mesoscopic properties ϕ and Z using 2D LS-DEM simulations. We found that ϕ and Z smoothly varied as a function of these descriptors. Further, we discovered that variations in these mesoscopic properties with morphology could be explained by interpretable geometric characteristics such as tesselation, nematic ordering, hexagonal packing, arching and interlocking. Next, we used a vational autoencoder (VAE) to develop a latent space of particle shapes. In this space, every vector corresponded to a unique

shape. Additionally, the latent space was continuous. As before, ϕ and Z appeared to smoothly vary in this space.

6.2 Outlook

The research in this thesis opens the door to many exciting directions for understanding and controlling granular materials. The 3D genetic cloning algorithm can be used to develop particles with a wider range of grain morphological properties, such as convexity. The algorithm can be tested on a wide range of parent datasets, generating libraries of grain morphologies which can be used in LS-DEM simulations. It would also be interesting to see how modifying the initial conditions for the genetic algorithm can affect the final results. Changing the initial conditions from a coarse ellipsoid to something else (such as a cube) could lead to more diverse clones.

The work in Chapter 4 implies that the arching phenomenon can be used to create stable tunnels in unreinforced granular environments. It would be interesting to see if this behavior scales to different soil environments, i.e. soils with different particle sizes, cohesion, friction and morphology. As ants can excavate in a wide variety of environments (Espinoza and Santamarina, 2010), it is worth investigating whether a generalized ant excavation strategy exists. Next, an algorithm could be developed which replicates the techniques used by ants for tunneling in granular environments. The algorithm could be run in environments more suitable to human excavation, such as in jointed rocks. This should be feasible in LS-DEM simulations with appropriate scaling of parameters (Rosakis et al., 2021). Whether this ant tunneling algorithm is practical for human excavation would be of great practical interest. Finally, the algorithm could be implemented in a robotic excavation system. If the robot contains a haptic feedback module that is able to sense force on grains and a visual component for determining tunnel size, the robot could choose where to dig such as to minimize the probability of tunnel collapse. The system could also be used for search and rescue missions as the robot could choose which piece of rubble, or 'grain,' to remove as to minimize collapse.

The methods developed in Chapter 5 lay the foundation for many novel research directions. As in 3D, new morphological properties could be specified to the genetic algorithm to generate new classes of particles. For instance, grain roughness could be a new parameter specified to control particle properties on a smaller length scale. Initial conditions can also be modified to generate larger classes of shapes.

Indeed, starting from an ellipse may not be the optimal initial condition for highly non-convex grains. Next, other mesoscopic or bulk properties can be investigated corresponding to the generated particles. One could investigate components of the material's stiffness tensor such as Young's modulus, constrained modulus, and Poisson's ratio. Further, critical state parameters corresponding to each shape could be probed including internal friction angle, yield stress and residual stress. It would be interesting to see if these bulk variables smoothly vary as a function of morphological property, and which descriptors lead to the most significant changes in these variables. Regarding the deep learning component, the latent space can be made richer by training on both new grains generated by the genetic algorithm and on real particle shapes obtained from XRCT. While it is not feasible to obtain the mesoscopic or bulk properties for all infinite particles in the latent space, intelligent sampling and interpolation could be performed to obtain an approximate mapping from latent space vector to mesoscopic/bulk variables. The high amount of structure in the latent space — such as particles with similar convexity and aspect ratio clustering together — means that using interpolation to 'guess' the values of bulk variables in unsampled areas could be very effective. Finally, as stated in Chapter 5 the latent space is particularly useful for topology optimization of granular materials. For instance, a genetic algorithm could be run in the latent space that attempts to maximize the stiffness of the granular material. With a learned function that maps latent space value to bulk property obviating the need to always run a simulation for each morphology, topology optimization of granular materials becomes feasible. Applications of topology optimization of granular materials include structured fabrics which can stiffen by a user-specified amount as in (Wang, Li, et al., 2021). Topology optimization could be leveraged to discover the ideal grain shape for constructing such materials. These materials have applications ranging from armor to temporary housing. Further, a granular material composed of non-convex shapes with high Young's modulus and low ϕ would be a desirable lightweight material (Wegst and Ashby, 2004). Discovering grain shapes which would build such a material is a promising application of the tools developed in this thesis.

It is the author's hope that the results in this thesis will inspire new, exciting research into the control of granular systems.

BIBLIOGRAPHY

Aleksiev, Antony S., Ana B. Sendova-Franks, and Nigel R. Franks (2007). "The selection of building material for wall construction by ants." In: *Animal Behaviour* 73.5, pp. 779–788. ISSN: 0003-3472. DOI: https://doi.org/10.1016/j.anbehav.2006.06.014. URL: http://www.sciencedirect.com/science/article/pii/S0003347207000395.

An, Xinhong et al. (2009). "Experimental study of the packing of mono-sized spheres subjected to one-dimensional vibration." In: *Powder Technology* 196.1, pp. 50–55.

Azéma, Emilien and Farhang Radjai (2012). "Force chains and contact network topology in sheared packings of elongated particles." In: *Physical Review E* 85.3, p. 031303.

Baker, Jessica and Arshad Kudrolli (2010). "Maximum and minimum stable random packings of platonic solids." In: *Physical Review E* 82.6, p. 061304.

Bardenhagen, Scott, Jeremiah Brackbill, and Deborah Sulsky (2000). "Numerical study of stress distribution in sheared granular material in two dimensions." In: *Physical Review E* 62.3, p. 3882.

Baule, Adrian and Hernán A. Makse (2014). "Fundamental challenges in packing problems: from spherical to non-spherical particles." In: *Soft Matter* 10.25, pp. 4423–4429.

Behringer, Robert P. and Bulbul Chakraborty (2018). "The physics of jamming for granular materials: A review." In: *Reports on Progress in Physics* 82.1, p. 012601.

Bentley, Jon Louis and Thomas A. Ottmann (1979). "Algorithms for reporting and counting geometric intersections." In: *IEEE Transactions on Computers* 28.09, pp. 643–647.

Boon, Chia Weng, Guy Houlsby, and Stefano Utili (2015). "Designing tunnel support in jointed rock masses via the DEM." In: *Rock Mechanics and Rock Engineering* 48.2, pp. 603–632.

Borela, Rodrigo et al. (2021). "Earthworm-inspired robotic locomotion in sand: an experimental study with X-ray tomography." In: *Géotechnique Letters* 11.1, pp. 66–73.

Brown, Eric et al. (2010). "Universal robotic gripper based on the jamming of granular material." In: *Proceedings of the National Academy of Sciences* 107.44, pp. 18809–18814.

Buarque de Macedo, Robert, Edward Andò, et al. (2021). "Unearthing real-time 3D ant tunneling mechanics." In: *Proceedings of the National Academy of Sciences* 118, pp. 1–15.

Buarque de Macedo, Robert, Konstantinos Karapiperis, et al. (2022). "What is shape? Characterizing particle morphology with genetic algorithms and deep generative models." In: *Granular Matter, in review*.

Buarque de Macedo, Robert, Jason Marshall, and Jose Andrade (2018). "Granular object morphological generation with genetic algorithms for discrete element simulations." In: *Granular Matter* 20.4, pp. 1–12.

Cassill, Deby, Walter Tschinkel, and Bradleigh Vinson (2002a). "Nest complexity, group size and brood rearing in the fire ant, Solenopsis invicta." In: *Insectes Sociaux* 49, pp. 158–163.

– (2002b). "Nest complexity, group size and brood rearing in the fire ant, Solenopsis invicta." In: *Insectes Sociaux* 49.2, pp. 158–163.

Cazals, Frédéric and Marc Pouget (2005). "Estimating differential quantities using polynomial fitting of osculating jets." In: *Computer Aided Geometric Design* 22.2, pp. 121–146. ISSN: 0167-8396. DOI: http://dx.doi.org/10.1016/j.cagd.2004.09.004. URL: http://www.sciencedirect.com/science/article/pii/S016783960400113X.

Cha, Minsu and Carlos Santamarina (2019). "Localized dissolution in sediments under stress." In: *Granular Matter* 21.3, p. 79.

Chen, Chee Nan, Wen-Yen Huang, and Cheng-Tsung Tseng (2011). "Stress redistribution and ground arch development during tunneling." In: *Tunnelling and Underground Space Technology* 26.1, pp. 228–235.

Chen, Ren-Peng, Qi-Wei Liu, et al. (2020). "Effect of particle shape on the development of 2D soil arching." In: *Computers and Geotechnics* 125, p. 103662.

Chen, Renpeng, LJ Tang, et al. (2011). "Face stability analysis of shallow shield tunnels in dry sandy ground using the discrete element method." In: *Computers and Geotechnics* 38.2, pp. 187–195.

Cheng, Lin, Jiaxi Bai, and Albert C. To (2019). "Functionally graded lattice structure topology optimization for the design of additive manufactured components with stress constraints." In: *Computer Methods in Applied Mechanics and Engineering* 344, pp. 334–359.

Ji-Cheng, Xun et al. (2011). "Advances in the micro-macro mechanics of granular soil materials." In: *Advances in Mechanics* 41.3, p. 351.

Cho, Gye-Chun, Jake Dodds, and J. Carlos Santamarina (May 2006a). "Particle shape effects on packing density, stiffness, and strength: natural and crushed sands." In: *Journal of Geotechnical and Geoenvironmental Engineering* 132.5, pp. 591–602. DOI: 10.1061/(asce)1090-0241(2006)132:5(591).

– (2006b). "Particle shape effects on packing density, stiffness, and strength: natural and crushed sands." In: *Journal of Geotechnical and Geoenvironmental Engineering* 132.5, pp. 591–602.

Cil, Mehmet and Khalid Alshibli (2012). "3D assessment of fracture of sand particles using discrete element method." In: *Geotechnique Letters* 2.3, pp. 161–166. DOI: 10.1680/geolett.12.00024. eprint: http://dx.doi.org/10.1680/geolett.12.00024. URL: http://dx.doi.org/10.1680/geolett.12.00024.

Cloud, Joseph M et al. (2021). "Towards autonomous lunar resource excavation via deep reinforcement learning." In: *ASCEND 2021*, p. 4217.

Cobo, Alex Xavier Jerves (Apr. 2016). "Microscopic rigin of Macroscopic Strength in Granular Media: A Numerical and Analytical Approach." PhD thesis. California Institute of Technology.

Coetzee, Corne and Daniel Els (2009). "Calibration of discrete element parameters and the modelling of silo discharge and bucket filling." In: *Computers and Electronics in agriculture* 65.2, pp. 198–212.

Cundall, Peter A and Otto DL Strack (1979a). "A discrete numerical model for granular assemblies". In: *Geotechnique* 29.1, pp. 47–65.

Cundall, Peter A. (1988). "Formulation of a three-dimensional distinct element model-Part I. A scheme to detect and represent contacts in a system composed of many polyhedral blocks." In: *International Journal of Rock Mechanics and Mining Sciences and Geomechanics Abstracts* 25.3, pp. 107–116. ISSN: 0148-9062. DOI: http://dx.doi.org/10.1016/0148-9062(88)92293-0. URL: http://www.sciencedirect.com/science/article/pii/0148906288922930.

Cundall, Peter A. and Otto D. L. Strack (1979b). "A discrete numerical model for granular assemblies." In: *Géotechnique* 29.1, pp. 47–65. DOI: 10.1680/geot.1979.29.1.47.

Day, Robert W. (2010). *Foundation engineering handbook: Design and construction with the 2009 international building code*. McGraw-Hill Education.

De Jong, Kenneth (1988). "Learning with genetic algorithms: An overview." In: *Machine Learning* 3.2, pp. 121–138. DOI: 10.1007/BF00113894. URL: http://dx.doi.org/10.1007/BF00113894.

De Rainville, François-Michel et al. (2012). "DEAP: A Python framework for evolutionary algorithms." In: *Proceedings of the 14th Annual Conference Companion on Genetic and Evolutionary Computation*. GECCO '12. Philadelphia, Pennsylvania, USA: ACM, pp. 85–92. ISBN: 978-1-4503-1178-6. DOI: 10.1145/2330784.2330799. URL: http://doi.acm.org/10.1145/2330784.2330799.

Di Prisco, Claudio et al. (2018). "Experimental investigation of the time-dependent response of unreinforced and reinforced tunnel faces in cohesive soils." In: *Acta Geotechnica* 13.3, pp. 651–670.

Do, Trong Nhan and Jian-Hong Wu (2020). "Simulation of the inclined jointed rock mass behaviors in a mountain tunnel excavation using DDA." In: *Computers and Geotechnics* 117, p. 103249.

Doersch, Carl (2016). "Tutorial on variational autoencoders." In: *arXiv preprint arXiv:1606.05908*.

Donev, Aleksandar et al. (2007). "Underconstrained jammed packings of nonspherical hard particles: Ellipses and ellipsoids." In: *Physical Review E* 75.5, p. 051304.

Duran, Jacques (2012). *Sands, powders, and grains: An introduction to the physics of granular materials.* Springer Science & Business Media.

Espinoza, D Nicolas and J. Carlos Santamarina (2010). "Ant tunneling—a granular media perspective." In: *Granular Matter* 12.6, pp. 607–616.

Fabri, Andreas and Sylvain Pion (2009). "CGAL: The Computational Geometry Algorithms Library." In: *Proceedings of the 17th ACM SIGSPATIAL International Conference on Advances in Geographic Information Systems*. GIS '09. Seattle, Washington: ACM, pp. 538–539. ISBN: 978-1-60558-649-6. DOI: 10.1145/1653771.1653865. URL: http://doi.acm.org/10.1145/1653771.1653865.

Fang, Yingguang, Lingfeng Guo, and Mingxun Hou (2020). "Arching effect analysis of granular media based on force chain visualization." In: *Powder Technology* 363, pp. 621–628.

Fortin, Félix-Antoine et al. (July 2012). "DEAP: Evolutionary algorithms made easy." In: *Journal of Machine Learning Research* 13, pp. 2171–2175.

Frost, J David et al. (2017). "Biologically-inspired insight into soil arching and tunnel stability from the topology of ant nests." In: *19th International Conference on Soil Mechanics and Geotechnical Engineering*. Seoul, South Korea.

Gan, Jieqing and Aibing Yu (2020). "DEM simulation of the packing of cylindrical particles." In: *Granular Matter* 22.1, pp. 1–19.

Geng, Junfei et al. (2001). "Footprints in sand: The response of a granular material to local perturbations." In: *Physical Review Letters* 87.3, p. 035506.

Gili, Josep and Eduardo Alonso (2002). "Microstructural deformation mechanisms of unsaturated granular soils." In: *International Journal for Numerical and Analytical Methods in Geomechanics* 26.5, pp. 433–468.

Gladstone, Rini Jasmine et al. (2021). "Robust topology optimization using variational autoencoders." In: *arXiv preprint arXiv:2107.10661*.

Goodman, Richard E et al. (1984). "Discontinuous deformation analysis." In: *The 25th US Symposium on Rock Mechanics (USRMS)*. Evanston, Illinois: OnePetro.

Goodman, Richard E (1999). "Karl Terzaghi: The engineer as artist." In: Reston, VA, USA: American Society of Civil Engineers.

Graaf, Joost de, René van Roij, and Marjolein Dijkstra (2011). "Dense regular packings of irregular nonconvex particles." In: *Physical Review Letters* 107.15, p. 155501.

Gravish, Nick, Scott V. Franklin, et al. (2012). “Entangled granular media.” In: *Physical review letters* 108.20, p. 208001.

Gravish, Nick, Mateo Garcia, et al. (2012). “Effects of worker size on the dynamics of fire ant tunnel construction.” In: *Journal of the Royal Society Interface* 9.77, pp. 3312–3322.

Gravish, Nick, Daria Monaenkova, et al. (2013). “Climbing, falling, and jamming during ant locomotion in confined environments.” In: *Proceedings of the National Academy of Sciences* 110.24, pp. 9746–9751.

Guessasma, Mohamed and Charles Machado (2018). “Three-dimensional DEM modelling of ball bearing with lubrication regime prediction.” In: *Lubricants* 6.2, p. 46.

Guises, Romain et al. (2009). “Granular packing: Numerical simulation and the characterisation of the effect of particle shape.” In: *Granular Matter* 11.5, pp. 281–292.

Guo, Peijun and Xubin Su (2007). “Shear strength, interparticle locking, and dilatancy of granular materials.” In: *Canadian Geotechnical Journal* 44.5, pp. 579–591. DOI: 10.1139/t07-010. eprint: http://dx.doi.org/10.1139/t07-010. URL: http://dx.doi.org/10.1139/t07-010.

Guo, Peijun and Shunhua Zhou (2013). “Arch in granular materials as a free surface problem.” In: *International Journal for Numerical and Analytical Methods in Geomechanics* 37.9, pp. 1048–1065.

Hafez, Ahmed et al. (2021). “The effect of particle shape on discharge and clogging.” In: *Scientific Reports* 11.1, pp. 1–11.

Hasbro, Inc (1983). *Jenga*.

Al-Hashemi, Hamzah M. Beakawi and Omar S. Baghabra Al-Amoudi (2018). “A review on the angle of repose of granular materials.” In: *Powder Technology* 330, pp. 397–417.

Hestroffer, Daniel et al. (2019). “Small solar system bodies as granular media.” In: *The Astronomy and Astrophysics Review* 27.1, pp. 1–64.

Höhner, Dominik et al. (2011). “Comparison of the multi-sphere and polyhedral approach to simulate non-spherical particles within the discrete element method: Influence on temporal force evolution for multiple contacts.” In: *Powder Technology* 208.3, pp. 643–656.

Holland, John H. (1992). “Genetic algorithms.” In: *Scientific American* 267.1, pp. 66–73.

Huang, Yang H (2014). “Slope stability analysis by the limit equilibrium method: Fundamentals and methods.” In: American Society of Civil Engineers. Reston, VA, USA.

Hyder Zeshan; Siau, Keng; and Fiona Fui-Hoon Nah (2018). "Use of artificial intelligence, machine learning, and autonomous technologies in the mining industry." In: *MWAIS 2018 Proceedings. 43.* 129, p. 104792. ISSN: 0925-7535. DOI: https://doi.org/10.1016/j.ssci.2020.104792. URL: http://www.sciencedirect.com/science/article/pii/S0925753520301892.

Hyslip, James P. and Luis E. Vallejo (1997). "Fractal analysis of the roughness and size distribution of granular materials." In: *Engineering Geology* 48.3-4. Fractals in Engineering Geology, pp. 231–244. ISSN: 0013-7952. DOI: http://dx.doi.org/10.1016/S0013-7952(97)00046-X. URL: http://www.sciencedirect.com/science/article/pii/S001379529700046X.

Jaeger, Heinrich M. and Juan J. de Pablo (2016). "Perspective: Evolutionary design of granular media and block copolymer patterns." In: *APL Materials* 4.5, p. 053209.

Jerves, Alex X, Reid Y Kawamoto, and José E Andrade (2017). "A geometry-based algorithm for cloning real grains." In: *Granular Matter* 19.2, p. 30.

– (2016). "Effects of grain morphology on critical state: a computational analysis." In: *Acta Geotechnica* 11.3, pp. 493–503.

Jihong, Zhu et al. (2021). "A review of topology optimization for additive manufacturing: Status and challenges". In: *Chinese Journal of Aeronautics* 34.1, pp. 91–110.

Jolliffe, Ian T. and Jorge Cadima (2016). "Principal component analysis: A review and recent developments." In: *Philosophical Transactions of the Royal Society A: Mathematical, Physical and Engineering Sciences* 374.2065, p. 20150202.

Kalender, Willi A. (2006). "X-ray computed tomography." In: *Physics in Medicine & Biology* 51.13, R29.

Karapiperis, Konstantinos et al. (2021). "Data-driven multiscale modeling in mechanics." In: *Journal of the Mechanics and Physics of Solids* 147, p. 104239.

Kawamoto, Reid et al. (2016). "Level set discrete element method for three-dimensional computations with triaxial case study." In: *Journal of the Mechanics and Physics of Solids* 91, pp. 1–13.

– (2018). "All you need is shape: predicting shear banding in sand with LS-DEM." In: *Journal of the Mechanics and Physics of Solids* 111, pp. 375–392.

Keller, Sean and Heinrich M Jaeger (2016). "Aleatory architectures." In: *Granular Matter* 18.2, pp. 1–11.

Khuong, Anaıs et al. (2016). "Stigmergic construction and topochemical information shape ant nest architecture." In: *Proceedings of the National Academy of Sciences* 113.5, pp. 1303–1308. ISSN: 0027-8424. DOI: 10.1073/pnas.1509829113. eprint: https://www.pnas.org/content/113/5/1303.full.pdf. URL: https://www.pnas.org/content/113/5/1303.

Kollmer, Jonathan E., Scott M. Lindauer, and Karen E. Daniels (Jan. 2016). "Granular materials in space exploration." In: *Earth and Space 2016*. American Society of Civil Engineers. DOI: 10.1061/9780784479971.021.

Kruggel-Emden, Harald et al. (2007). "Review and extension of normal force models for the Discrete Element Method." In: *Powder Technology* 171.3, pp. 157–173. ISSN: 0032-5910. DOI: http://dx.doi.org/10.1016/j.powtec.2006.10.004. URL: http://www.sciencedirect.com/science/article/pii/S0032591006004360.

Kumar, Siddhant and Dennis M Kochmann (2021). "What machine learning can do for computational solid mechanics." In: *arXiv preprint arXiv:2109.08419*.

Labuz, Joseph F and Arno Zang (2012). "Mohr–Coulomb failure criterion." In: *Rock mechanics and rock engineering* 45.6, pp. 975–979.

Lee, Chung-Jung et al. (2006). "Tunnel stability and arching effects during tunneling in soft clayey soil." In: *Tunnelling and Underground Space Technology* 21.2, pp. 119–132.

Li, Cheng-Qing, Wen-Jie Xu, and Qing-Shan Meng (2015). "Multi-sphere approximation of real particles for DEM simulation based on a modified greedy heuristic algorithm." In: *Powder Technology* 286, pp. 478–487.

Li, Liuchi, Eloıse Marteau, and José E. Andrade (2019). "Capturing the inter-particle force distribution in granular material using LS-DEM." In: *Granular Matter* 21.3, p. 43.

Li, Shuixiang, Peng Lu, et al. (2013). "Quasi-random packing of tetrahedra." In: *Soft Matter* 9.39, pp. 9298–9302.

Lim, Keng-Wit, Kristian Krabbenhoft, and José E. Andrade (2014). "On the contact treatment of non-convex particles in the granular element method." In: *Computational Particle Mechanics* 1.3, pp. 257–275. DOI: 10.1007/s40571-014-0019-2. URL: http://dx.doi.org/10.1007/s40571-014-0019-2.

Lin, Xing-Tao et al. (2019). "Three-dimensional stress-transfer mechanism and soil arching evolution induced by shield tunneling in sandy ground." In: *Tunnelling and Underground Space Technology* 93, p. 103104.

Lou, Shan, Xiangqian Jiang, and Paul J. Scott (2013). "Application of the morphological alpha shape method to the extraction of topographical features from engineering surfaces." In: *Measurement* 46.2, pp. 1002–1008.

Lozano, Celia et al. (Apr. 2012). "Breaking arches with vibrations: The role of defects." In: *Physical Review Letters* 109, p. 068001. DOI: 10.1103/PhysRevLett.109.068001.

MacMahon, James A., John F. Mull, and Thomas O. Crist (2000). "Harvester ants (Pogonomyrmex spp.): Their community and ecosystem influences." In: *Annual Review of Ecology and Systematics* 31.1, pp. 265–291. DOI: 10.1146/annurev.ecolsys.31.1.265.

Makse, Hernán A., David L. Johnson, and Lawrence M. Schwartz (2000). "Packing of compressible granular materials." In: *Physical review letters* 84.18, p. 4160.

Meng, Lingyi et al. (2012). "Shape and size effects on the packing density of binary spherocylinders." In: *Powder Technology* 228, pp. 284–294.

Mesh (scale) (2020). https://en.wikipedia.org/wiki/Mesh_(scale).

Metcalfe, Guy et al. (2002). "Granular friction, Coulomb failure, and the fluid-solid transition for horizontally shaken granular materials." In: *Physical Review E* 65.3, p. 031302.

Minter, Nicholas, Nigel Franks, and Katharine Brown (Aug. 2011). "Morphogenesis of an extended phenotype: Four-dimensional ant nest architecture." In: *Journal of the Royal Society, Interface / the Royal Society* 9, pp. 586–95. DOI: 10.1098/rsif.2011.0377.

Minter, Nicholas J., Ana B. Sendova-Franks, and Nigel R. Franks (2013). "Nest-seeking rock ants (Temnothorax albipennis) trade off sediment packing density and structural integrity for ease of cavity excavation." In: *Behavioral Ecology and Sociobiology* 67.11, pp. 1745–1756.

Miskin, Marc Z. and Heinrich M. Jaeger (2013). "Adapting granular materials through artificial evolution." In: *Nature Materials* 12.4, pp. 326–331.

– (2014). "Evolving design rules for the inverse granular packing problem." In: *Soft Matter* 10.21, pp. 3708–3715.

Monaenkova, Daria et al. (2015). "Behavioral and mechanical determinants of collective subsurface nest excavation." In: *Journal of Experimental Biology* 218.9, pp. 1295–1305.

Monfared, Siavash et al. (Dec. 2020). "Effect of confinement on capillary phase transition in granular aggregates." In: *Physical Review Letters* 125.25.

Morrissey, John P., Jin Y. Ooi, and Jian Fei Chen (2013). "A DEM study of silo discharge of a cohesive solid." In: *PARTICLES III: proceedings of the III International Conference on Particle-Based Methods: fundamentals and applications*. CIMNE, pp. 298–309.

Nassauer, Benjamin, Thomas Liedke, and Meinhard Kuna (2013). "Polyhedral particles for the discrete element method." In: *Granular Matter* 15.1, pp. 85–93.

Neil, Brent and John Russ (2012). *Measuring Shape*. Boca Raton, Florida: CRC Press.

Nguyen, Duc-Hanh et al. (Mar. 2015). "Effects of shape and size polydispersity on strength properties of granular materials." In: *Physical Review E* 91 (3), p. 032203. DOI: 10.1103/PhysRevE.91.032203. URL: https://link.aps.org/doi/10.1103/PhysRevE.91.032203.

Oda, Masanobu and Kazuyoshi Iwashita (2020). "Mechanics of Granular Materials." In: Boca Raton, Florida: CRC Press.

Oliveira, Agamenon R.E. (2004). "The contribution of coulomb to applied mechanics." In: *International Symposium on History of Machines and Mechanisms*. Springer, pp. 217–226.

Pal, Raj Kumar, Robert Buraque de Macedo, and José Andrade (2021). "Tunnel excavation in granular media: the role of force chains." In: *Granular Matter* 23.4, pp. 1–14.

Potyondy, David O. and Peter A. Cundall (2004). "A bonded-particle model for rock." In: *International Journal of Rock Mechanics and Mining Sciences* 41.8, pp. 1329–1364.

Pu, Yunchen et al. (2016). "Variational autoencoder for deep learning of images, labels and captions." In: *Advances in Neural Information Processing Systems* 29, pp. 2352–2360.

Vu-Quoc, Loc, Xiang Zhang, and Otis .R. Walton (2000). "A 3-D discrete-element method for dry granular flows of ellipsoidal particles." In: *Computer Methods in Applied Mechanics and Engineering* 187.3, pp. 483–528. ISSN: 0045-7825. DOI: http://dx.doi.org/10.1016/S0045-7825(99)00337-0.

Radjai, Farhang et al. (1996). "Force distributions in dense two-dimensional granular systems." In: *Physical Review Letters* 77.2, p. 274.

Ramesh, K. (2000). *Digital photoelasticity*. Bristol, England: IOP Publishing.

Rath, Sovit Ranjan (Feb. 2021). *Generating fictional celebrity faces using convolutional variational Autoencoder and pytorch*. URL: https://debuggercafe.com/generating-fictional-celebrity-faces-using%20%5C%5C-convolutional-variational-autoencoder-and-pytorch/.

Richefeu, Vincent, Moulay Saıd El Youssoufi, Robert Peyroux, et al. (2008). "A model of capillary cohesion for numerical simulations of 3D polydisperse granular media." In: *International Journal for Numerical and Analytical Methods in Geomechanics* 32.11, pp. 1365–1383.

Richefeu, Vincent, Moulay Saıd El Youssoufi, and Farhang Radjai (2006). "Shear strength properties of wet granular materials." In: *Physical Review E* 73.5, p. 051304.

Riley, Ken, Michael Hobson, and Stephen Bence (2006). *Mathematical Methods for Physics and Engineering*. Cambridge, England: Cambridge University Press.

Rognon, Pierre G. et al. (2006). "Rheophysics of cohesive granular materials." In: *EPL (Europhysics Letters)* 74.4, p. 644.

Rosakis, Ares J et al. (2021). "Implications of Buckingham's Pi theorem to the study of similitude in discrete structures: Introduction of the RFN, μN, and SN dimensionless numbers and the concept of structural speed." In: *Journal of Applied Mechanics* 88.9.

Rosinha, Inês P. et al. (2015). "Topology optimization for biocatalytic microreactor configurations." In: *Computer Aided Chemical Engineering* 37, pp. 1463–1468.

Sadeghi, Ali, Alessio Mondini, and Barbara Mazzolai (2017). "Toward self-growing soft robots inspired by plant roots and based on additive manufacturing technologies." In: *Soft Robotics* 4.3, pp. 211–223.

Saint-Cyr, Baptiste et al. (2011). "Rheology of granular materials composed of nonconvex particles." In: *Physical Review E* 84.4, p. 041302.

Salerno, K. Michael et al. (2018). "Effect of shape and friction on the packing and flow of granular materials." In: *Physical Review E* 98.5, p. 050901.

Schreck, Carl F, Ning Xu, and Corey S O'Hern (2010). "A comparison of jamming behavior in systems composed of dimer-and ellipse-shaped particles." In: *Soft Matter* 6.13, pp. 2960–2969.

Shaebani, M. Reza, Tamás Unger, and János Kertész (2009). "Extent of force indeterminacy in packings of frictional rigid disks." In: *Physical Review E* 79.5, p. 052302.

Shi, Jia-jie et al. (2021). "Randomly generating three-dimensional realistic schistous sand particles using deep learning: Variational autoencoder implementation." In: *Engineering Geology*, p. 106235.

Sivolella, Davide (2019). "Off-World Mining." In: *Space Mining and Manufacturing*. Springer, pp. 51–79.

Sousa, Rita L. and Herbert H. Einstein (2021). "Lessons from accidents during tunnel construction." In: *Tunnelling and Underground Space Technology* 113, p. 103916.

Sperl, Matthias (2006). "Experiments on corn pressure in silo cells — translation and comment of Janssen's paper from 1895." In: *Granular Matter* 8.2, pp. 59–65. ISSN: 1434-7636. DOI: 10.1007/s10035-005-0224-z. URL: http://dx.doi.org/10.1007/s10035-005-0224-z.

Stamati, Olga et al. (2020). "spam: Software for Practical Analysis of Materials." In: *Journal of Open Source Software* 5.51, p. 2286.

Staron, Lydie and John Hinch (2007). "The spreading of a granular mass: Role of grain properties and initial conditions." In: *Granular Matter* 9.3, pp. 205–217.

Terzaghi, Karl (1943a). *Theoretical Soil Mechanics.* Hoboken, NJ, USA: Wiley.

– (1943b). "Theoretical Soil Mechanics." In: Hoboken, NJ, USA: John Wiley & Sons, Ltd. Chap. 5, pp. 66–76.

– (1962). "Stability of steep slopes on hard unweathered rock." In: *Geotechnique* 12.4, pp. 251–270.

Terzaghi, Karl von (1925). "Earthwork mechanics based on soil physics." In: *Erdbaumechanik auf bodenphysikalisher Grundlage. Vienna: Franz Deuticke*.

Tschinkel, Walter R. (2003). "Subterranean ant nests: Trace fossils past and future?" In: *Palaeogeography, Palaeoclimatology, Palaeoecology* 192.1. New Interpretations of Complex Trace Fossils, pp. 321–333. ISSN: 0031-0182. DOI: https://doi.org/10.1016/S0031-0182(02)00690-9. URL: http://www.sciencedirect.com/science/article/pii/S0031018202006909.

Tu, Xuxin and José E Andrade (2008). "Criteria for static equilibrium in particulate mechanics computations." In: *International Journal for Numerical Methods in Engineering* 75.13, pp. 1581–1606.

US Mine Production Increasing, Estimated Value of 86.3 Billion in Minerals (2020). https://www.usgs.gov.

Vitali, Osvaldo P.M., Tarcisio B. Celestino, and Antonio Bobet (2018). "Analytical solution for tunnels not aligned with geostatic principal stress directions." In: *Tunnelling and Underground Space Technology* 82, pp. 394–405.

Vlahinić, Ivan et al. (2014). "Towards a more accurate characterization of granular media: Extracting quantitative descriptors from tomographic images." In: *Granular Matter* 16.1, pp. 9–21.

Wadell, Hakon (1935). "Volume, shape, and roundness of quartz particles." In: *The Journal of Geology* 43.3, pp. 250–280. ISSN: 00221376, 15375269. URL: http://www.jstor.org/stable/30056250.

Wang, Chuncheng, Kejun Dong, and Aibing Yu (2015). "Structural characterization of the packings of granular regular polygons." In: *Physical Review E* 92.6, p. 062203.

Wang, Liwei, Yu-Chin Chan, et al. (2020). "Deep generative modeling for mechanistic-based learning and design of metamaterial systems." In: *Computer Methods in Applied Mechanics and Engineering* 372, p. 113377.

Wang, Yifan, Liuchi Li, et al. (2021). "Structured fabrics with tunable mechanical properties." In: *Nature* 596.7871, pp. 238–243.

Wegst, Ulrike G.K. and Michael F. Ashby (2004). "The mechanical efficiency of natural materials." In: *Philosophical Magazine* 84.21, pp. 2167–2186.

Werfel, Justin, Kirstin Petersen, and Radhika Nagpal (2014). "Designing collective behavior in a termite-ispired robot construction team." In: *Science* 343.6172, pp. 754–758. DOI: 10.1126/science.1245842. eprint: https://science.sciencemag.org/content/343/6172/754.full.pdf.

Wold, Svante, Kim Esbensen, and Paul Geladi (1987). "Principal component analysis." In: *Chemometrics and Intelligent Laboratory Systems* 2.1, pp. 37–52. ISSN: 0169-7439. DOI: http://dx.doi.org/10.1016/0169-7439(87)80084-9. URL: http://www.sciencedirect.com/science/article/pii/0169743987800849.

Wu, Lin et al. (2020). “3D discrete element method modelling of tunnel construction impact on an adjacent tunnel.” In: *KSCE Journal of Civil Engineering* 24.2, pp. 657–669.

Yang, Jiannan and Xiaodong D. Luo (2015). “Exploring the relationship between critical state and particle shape for granular materials.” In: *Journal of the Mechanics and Physics of Solids* 84, pp. 196–213.

Yin, Zhen-Yu, Pei Wang, and Fengshou Zhang (2020). “Effect of particle shape on the progressive failure of shield tunnel face in granular soils by coupled FDM-DEM method.” In: *Tunnelling and Underground Space Technology* 100, p. 103394.

Yuliza, Elfi et al. (2018). “Stability of granular tunnel.” In: *Granular Matter* 20.4, pp. 1–13.

Zhao, Jian et al. (2011). “Shape influences on the packing density of frustums.” In: *Powder technology* 214.3, pp. 500–505.

Zhou, B. and J. Wang (2016). “Generation of a realistic 3D sand assembly using X-ray micro-computed tomography and spherical harmonic-based principal component analysis.” In: *International Journal for Numerical and Analytical Methods in Geomechanics*. ISSN: 1096-9853. DOI: 10.1002/nag.2548.

Zhou, Bo and Jianfeng Wang (2017). “Generation of a realistic 3D sand assembly using X-ray micro-computed tomography and spherical harmonic-based principal component analysis.” In: *International Journal for Numerical and Analytical Methods in Geomechanics* 41.1, pp. 93–109.

Zhou, Zong-Yan, Rui-Ping Zou, et al. (2011). “Dynamic simulation of the packing of ellipsoidal particles.” In: *Industrial & Engineering Chemistry Research* 50.16, pp. 9787–9798.

Zhuravlev, V Ph (2013). “On the history of the dry friction law.” In: *Mechanics of Solids* 48.4, pp. 364–369.